Asteroseismic grid modeling of the *Kepler* LEGACY sample: Investigating the helium enrichment law

Nuno Moedas
Mestrado em Astronomia e Astrofísica
Departamento de Física e Astronomia
2019

Orientador
Tiago L. Campante, Investigador (CAUP) & Professor Auxiliar Convidado (FCUP)
Coorientador
Margarida S. Cunha, Investigadora (CAUP)

U.PORTO

FACULDADE DE CIÊNCIAS
UNIVERSIDADE DO PORTO

Todas as correções determinadas pelo júri, e só essas, foram efetuadas.

O Presidente do Júri,

Porto, _____/_____/_____

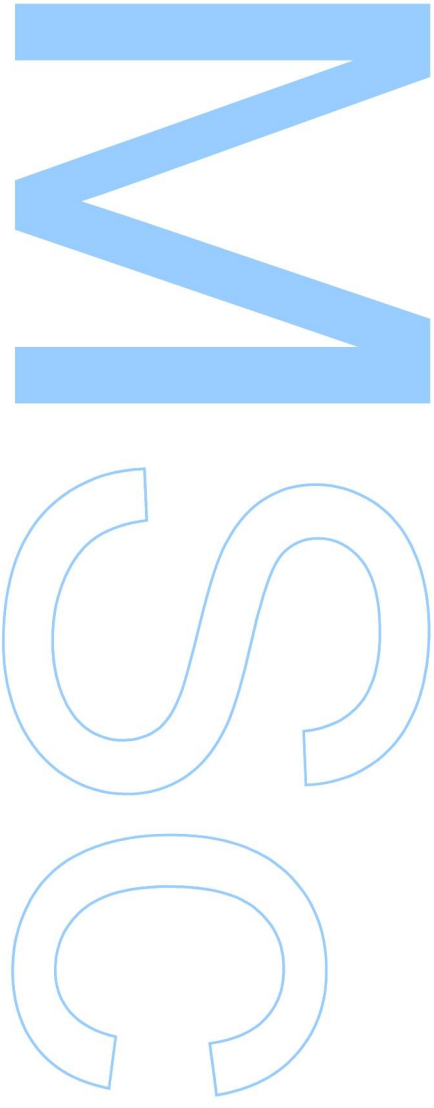

Faculdade de Ciências da Universidade do Porto
Departamento de Física e Astronomia

Asteroseismic grid modeling of the *Kepler* LEGACY sample: Investigating the helium enrichment law

Nuno Alexandre Martins Moedas (up201708257)

Mestrado em Astronomia e Astrofísica

Orientador: Tiago Campante

Coorientadora: Margarida Cunha

Ano 2018/2019

Acknowledgments

I would like to thank Dr. Tiago L. Campante and Dr. Margarida S. Cunha for having guided me through this period. I would also like to thank Mr. Benard Nsamba, not only for teaching me how to work with the different modeling codes necessary to the completion of this work, but also for guiding me through this project. I would also like to thank Dr. Kuldeep Verma for providing access to the data from his work on helium glitches. At last, I want to thank all my colleagues who helped me with my thesis.

Resumo

A abundância inicial de hélio é um ingrediente essencial na modelação de estrelas do tipo solar que, no entanto, permanece pouco restringida pelas observações. Isto porque a abundância de hélio não pode ser determinada diretamente a partir de observações espectroscópicas, ou seja, as riscas do hélio não são detectáveis nos espectros das estrelas do tipo solar. Uma solução comum para este problema é estimar o valor inicial da abundância de hélio através de uma relação semi-empírica entre o hélio e os elementos pesados, ancorada nos valores de nucleossíntese do Big Bang. Dependendo da escolha da composição solar utilizada na calibração dos modelos, esta relação entre o hélio e elementos pesados, dada por ($\frac{\Delta Y}{\Delta Z}$), apresenta variações entre 1 e 3. Neste estudo, adotamos a amostra estelar *Kepler* LEGACY, que dispõe de valores precisos para astrossismologia, e exploramos as incertezas sistemáticas associadas aos parâmetros estelares derivados (i.e., densidade média, raio, massa e idade) decorrentes das diferentes razões $\frac{\Delta Y}{\Delta Z}$ adoptadas. Com efeito, exploramos as incertezas sistemáticas associadas aos parâmetros estelares derivados, considerando $\frac{\Delta Y}{\Delta Z} = 1.4$ e $\frac{\Delta Y}{\Delta Z} = 2.0$ nas nossas técnicas de modelação. Como resultado, foram encontrados enviesamentos nos valores derivados para as massas e os raios estelares, com a grelha de modelos construída considerando a relação $\frac{\Delta Y}{\Delta Z} = 2.0$ apresentando menores valores para as massas e raios. As incertezas sistemáticas são de 2,6% e 1,1% para a massa e raio, respetivamente. Reportamos ainda uma boa concordância em termos das densidades médias derivadas, com incertezas estatísticas comparáveis às incertezas sistemáticas. Além disso, também comparámos os nossos resultados com os requisitos de precisão da missão PLATO (ESA), mostrando que as diferenças no tratamento da razão $\frac{\Delta Y}{\Delta Z}$ produzem resultados que estão dentro dos limites de precisão exigidos pela missão (de 2-4% para o raio, 10-15% para a massa e 10% para a idade). Contudo, estes limites podem ser excedidos ao considerar diferentes processos de transporte nos modelos estelares, o que pode ser um problema. Finalmente, comparámos a abundância inicial de hélio nos nossos modelos optimizados com os valores observacionais obtidos por Verma et al. para uma sub-amostra das nossas estrelas-alvo, para a qual foi possível uma abordagem através da análise dos *glitches*.

Abstract

The initial helium abundance is an essential ingredient in the modeling of solar-type stars. The abundance of helium in these stars remains, however, a poorly constrained observational property. This is because it cannot be directly determined from spectroscopic observations, i.e., helium lines are not detectable in the spectra of solar-type stars. A common solution is then to estimate the initial helium abundance via a semi-empirical helium-to-heavy-element ratio ($\frac{\Delta Y}{\Delta Z}$), anchored to the standard Big Bang nucleosynthesis value. Depending on the choice of solar composition used in model calibration, the $\frac{\Delta Y}{\Delta Z}$ is found to vary between 1 and 3. In this study, we adopt the *Kepler* LEGACY stellar sample, for which precise asteroseismology is available, and explore the systematic uncertainties in the derived stellar parameters (i.e., mean density, radius, mass, and age) arising from different values of the $\frac{\Delta Y}{\Delta Z}$ adopted. We explored the systematic uncertainties in the derived stellar parameters arising from setting the $\frac{\Delta Y}{\Delta Z}$ to 1.4 and 2.0 in our modeling techniques. We found biases in the derived stellar masses and radii, with the grid having a higher $\frac{\Delta Y}{\Delta Z}$ yielding lower masses and radii. The systematic uncertainties were found to be 2.6% and 1.1% in mass and radius, respectively. We report a good agreement in terms of the derived mean densities with statistical uncertainties comparable to systematic uncertainties. In addition, our results were compared to ESA's PLATO stellar property accuracy requirements, showing that differences in the treatment of the $\frac{\Delta Y}{\Delta Z}$ yield results which are in the limit of the required PLATO accuracy limits of 2-4% for the radius, 10-15% for the mass, and 10% for the age. Therefore, these limits may be exceeded when one varies different chemical transport processes in stellar models, thus may be a point of concern. Finally, we compared the initial helium abundance in our optimized models with the values derived observationally by Verma et al. for a sub-sample of our target stars for which a glitch analysis was possible.

Key words

Asteroseismology, solar-type stars, helium abundance, helium enrichment law, stellar modeling, stellar grids, *Kepler* LEGACY Sample

Contents

Acknowledgments **I**

Resumo **III**

Abstract **V**

1 Introduction **1**

2 Stellar Structure and Evolution **3**

2.1 Equations of Stellar Structure 3

2.2 Energy Transport 4

2.2.1 Radiative Transport 4

2.2.2 Transport by Convection 4

2.3 Energy Production 6

2.4 The HR Diagram 7

2.5 Stellar Evolution 9

2.5.1 Effect of Mass 13

2.5.2 Effect of Metallicity 16

2.5.3 Mixing Length Parameter 20

2.5.4 Atomic Diffusion 23

3 Theoretical Asteroseismology **26**

3.1 Stellar Pulsation Equations 26

3.2 Oscillation Modes 29

3.3 Scaling Relations 30

4 MESA - Modules for Experiments in Stellar Astrophysics **32**

5 GYRE **36**

6 AIMS - Asteroseismic Inference on a Massive Scale **40**

7 Helium Abundance **44**

7.1 Stellar Grids 44

7.2 *Kepler* LEGACY Sample 45

7.3 Results 47

7.3.1 Impact of Luminosity Constraint on the Optimization 47

7.3.2 Comparison with the Literature 52
7.3.3 Grid Comparison 65
7.3.4 Models vs. Inference from Structural Glitches 68

8 Summary **76**

A Appendix **82**

List of Tables

2.1 Diagrams of the p-p chain and CNO cycle 6
4.1 Criteria used for selection of time step and stop conditions in the production of models 33
4.2 Parameters used for the first grids 34
6.1 Obtained solar values 43
6.2 Parameter values obtained from different pipelines, plus the solar values and the values obtained from Grid 2 43
7.1 Physical characteristics and differences between the grids 45
7.2 Parameter range for the grids 45
7.3 Statistical values of the grid comparison 65
A.1 Classical parameters of stars in the LEGACY sample, plus the Sun, used as constraints 82
A.2 Bolometric correction coefficients. 84
A.3 Obtained mass, radius, age, and density for grid A without L_* 84
A.4 Obtained mass, radius, age, and density for grid A with L_* 86
A.5 Obtained mass, radius, age, and density for grid B without L_* 89
A.6 Obtained mass, radius, age, and density for grid B with L_* 91
A.7 Results for the helium surface abundance obtained using the grids 93
A.8 Summary of codes, physical inputs, and optimization methods applied by each pipeline 96
A.9 Results from ASTFIT 96
A.10 Results from BASTA 99
A.11 Results from YMCM 102
A.12 Helium surface abundance obtained through measurement of stellar glitches 105

List of Figures

2.1 The HR diagram 8
2.2 HR diagram for a 1 $M_\odot$ star 9
2.3 Radius vs. age (1 $M_\odot$) 9
2.4 Temperature gradient and adiabatic gradient for a 1 $M_\odot$ star 11
2.5 $\log(T_c)$ vs. $\log(\rho_c)$ (1 $M_\odot$) 12
2.6 HR diagram for different masses and their age at the end of the MS 13
2.7 $\log(T_c)$ vs. $\log(\rho_c)$ for different M_* 14
2.8 Radii of stars of varying mass at different evolutionary stages for different masses . . . 14
2.9 Temperature gradient and adiabatic gradient for different M_* 15
2.10 HR diagram for different metallicities and their age at the end of the MS 16
2.11 $\log(T_c)$ vs. $\log(\rho_c)$ for different Z 17
2.12 Radii of stars at different evolutionary stages for different Z 18
2.13 Temperature gradient and adiabatic gradient for different Z 19
2.14 HR diagram for different α_{MLT} and their age at the end of the MS 20
2.15 $\log(T_c)$ vs. $\log(\rho_c)$ for different α_{MLT} 21
2.16 Radii of stars at different evolutionary stages for different α_{MLT} 21
2.17 Temperature gradient and adiabatic gradient for different α_{MLT} 22
2.18 HR diagram for stars with and without diffusion 23
2.19 $\log(T_c)$ vs. $\log(\rho_c)$ for stars with and without diffusion 24
2.20 Abundance profile of hydrogen and helium 25
3.1 Spherical harmonics 27
3.2 S_ℓ, N and ω_c frequencies of a MS star and an RG star 28
3.3 Cyclic frequencies computed for the Sun 29
3.4 Power density spectrum of the Sun 31
4.1 Step Histograms 33
4.2 HR diagram for Grid 1 and 2 for $\alpha_{\mathrm{MLT}} = 2.0$ 34
4.3 Full HR diagram for Grid 2 35
5.1 Frequencies for MS and SG phases 36
5.2 Evolution of the frequencies with same ℓ 37
5.3 Evolution of $\Delta\nu$ 38
5.4 Contour map of $\Delta\nu$ in HR diagram 38
6.1 Échelle diagrams 40
6.2 Histograms of the probability density function for M_* 41

6.3 Correlation function of different parameters 42
7.1 *Kepler* LEGACY sample 46
7.2 Relative mass deviation for grid A models with and without L_* 48
7.3 Relative radius deviation for Grid A models with and without L_* 48
7.4 Relative density deviation for Grid A models with and without L_* 49
7.5 Relative age deviation for Grid A models with and without L_* 49
7.6 Relative mass deviation for Grid B models with and without L_* 50
7.7 Relative radius deviation for Grid B models with and without L_* 50
7.8 Relative density deviation for Grid B models with and without L_* 51
7.9 Relative age deviation for Grid B models with and without L_* 51
7.10 Relative mass deviation between results from grid A and ASTFIT 53
7.11 Relative radius deviation between results from grid A and ASTFIT 53
7.12 Relative density deviation between results from grid A and ASTFIT 54
7.13 Relative age deviation between results from grid A and ASTFIT 54
7.14 Relative mass deviation between results from grid B and ASTFIT 55
7.15 Relative radius deviation between results from grid B and ASTFIT 55
7.16 Relative density deviation between results from grid B and ASTFIT 56
7.17 Relative age deviation between results from grid B and ASTFIT 56
7.18 Relative mass deviation between results from grid A and BASTA 57
7.19 Relative radius deviation between results from grid A and BASTA 57
7.20 Relative density deviation between results from grid A and BASTA 58
7.21 Relative age deviation between results from grid A and BASTA 58
7.22 Relative mass deviation between results from grid B and BASTA 59
7.23 Relative radius deviation between results from grid B and BASTA 59
7.24 Relative density deviation between results from grid B and BASTA 60
7.25 Relative age deviation between results from grid B and BASTA 60
7.26 Relative mass deviation between results from grid A and YMCM 61
7.27 Relative radius deviation between results from grid A and YMCM 61
7.28 Relative density deviation between results from grid A and YMCM 62
7.29 Relative age deviation between results from grid A and YMCM 62
7.30 Relative mass deviation between results from grid B and YMCM 63
7.31 Relative radius deviation between results from grid B and YMCM 63
7.32 Relative density deviation between results from grid B and YMCM 64
7.33 Relative age deviation between results from grid B and YMCM 64

7.34 Relative mass deviation between Grids A and B models 66
7.35 Relative radius deviation between Grids A and B models 66
7.36 Relative density deviation between Grids A and B models 67
7.37 Relative age deviation between Grids A and B models 67
7.38 Difference between model helium abundance (Grid A) and the value obtained from glitches (MESA calibration) 70
7.39 Difference between model helium abundance (Grid A) and the value obtained from glitches (GARSTEC calibration) 70
7.40 Difference between model helium abundance (Grid B) and the value obtained from glitches (MESA calibration) 71
7.41 Difference between model helium abundance (Grid B) and the value obtained from glitches (GARSTEC calibration) 71
7.42 Estimated value of $\frac{\Delta Y}{\Delta Z}$ for each star as a function of Y_{i} 72
7.43 Estimated value of $\frac{\Delta Y}{\Delta Z}$ for each star as a function of Y_{s} 72
7.44 Estimated $\frac{\Delta Y}{\Delta Z}$ as a function of age 73
7.45 δY_{i} as a function of Y_{i} 73
7.46 δY_{i} as a function of Y_{s} 74

List of Abbreviations

ASTFIT	ASTEC FITting
AIMS	Asteroseismic Inference on a Massive Scale
BASTA	BAyesian STellar Algorithm
ESA	European Space Agency
GARSTEC	GARching Stellar Evolution Code
HR	Hertzsprung–Russell
MS	Main Sequence
MMS	Magnus-Multiple-Shooting
MLT	Mixing-Length Theory
MESA	Modules for Experiments in Stellar Astrophysics
SG	Subgiant
RG	Red-Giant
PLATO	PLAnetary Transits and Oscillations
YMCM	Yale Monte Carlo Method
ZAMS	Zero Age Main Sequence

1 Introduction

Stars are extremely interesting objects to study. They come in a variety of flavors, from low-mass stars that undergo a calm and long evolution path, to very massive stars that quickly reach their end with a supernova explosion. Ultimately, they are the true building blocks of the Galaxy, driving its chemical evolution [1].

In this work, we use asteroseismology to study solar-type stars by means of their natural, resonant oscillations [2, 3]. We resort to three computational programs to study these stars. We use *Modules for Experiments in Stellar Astrophysics* (MESA) to build models throughout stellar evolution, allowing for the construction of well-sampled grids containing different evolutionary tracks across a range of masses and chemical compositions [4]. We use the GYRE oscillation code to numerically compute the theoretical oscillation frequencies of each model previously built [5]. Finally, the *Asteroseimic Inference on a Massive Scale* (AIMS) algorithm allows us to search the stellar model grids and obtain the stellar parameters that best fit the observations [6].

Our aim is to investigate the abundance of helium in solar-type stars, which is the second most abundant element in the Universe. Despite this, the relatively low effective temperatures of these stars prevent a spectroscopic measurement of the helium abundance from being made, as the temperature required to excite an atomic transition exceeds $20,000$K [7, 8]. For this reason, the helium mass fraction in models of these stars is predicted from observables through a so-called helium enrichment law, which depends on the helium enrichment ratio $\left(\frac{\Delta Y}{\Delta Z}\right)$ (where Y and Z represent the helium and heavy element mass fractions, respectively).

Through the past years, the $\frac{\Delta Y}{\Delta Z}$ has been study in different works, showing that this parameter is poorly constrained. The use of nearby K-dwarf stars and a set of isochrones have shown similar estimations for $\frac{\Delta Y}{\Delta Z}$ around 2.1 [8, 9]. However, observations considering metal-poor galaxy H II regions, Magellanic cloud H II regions, and M17 abundances gave an estimation of $\frac{\Delta Y}{\Delta Z} \sim 1.6$ when considering temperature fluctuations [10]. However, another result was obtained when only using galaxy H II regions S206 and M17, with [10] estimating $\frac{\Delta Y}{\Delta Z} = 1.41 \pm 0.62$, a value consistent with the standard chemical evolution models. Studies of the chemical composition of the Sun demonstrates that a different choice of the solar composition leads to a value of $\frac{\Delta Y}{\Delta Z}$ within the range of 1.7 to 2.2 [11]. By taking into account the different studies, it is generally accepted for $\frac{\Delta Y}{\Delta Z}$ to be between 1 and 3, for solar-type stars.

We address this problem by modeling solar-type stars from the *Kepler* LEGACY sample (66 stars in total), which exhibit a high signal-to-noise ratio in their oscillation spectra [16]. Then, we compare the modeled surface helium abundance to the values inferred from the analysis of structural glitches [14]. The data used in this thesis was collected by during the *Kepler* mission, a satellite launched

in 2009 that acquired time-series data from a large number of stars over the course of four years [12]. A new mission is currently being prepared by the European Space Agency (ESA), the *PLATO* (PLAnetary Transits and Oscillations) mission, which aims at detecting and characterizing extrasolar planets, and also will provide new data in the seismic activity of the star that host the exoplanet. This will give access to new time-series data of stars and their planets, with even greater accuracy [13]. PLATO is due to launch in 2026.

This work is organized as follows. In section 2, we provide a set of basic concepts in stellar structure and evolution, followed by a theoretical introduction to asteroseismology in section 3. Sections 4, 5 and 6 introduce MESA, GYRE, and AIMS, respectively, from a user's point of view. Section 7 discusses the problem of helium abundance and presents our results. Finally, section 8 contains our conclusions.

2 Stellar Structure and Evolution

2.1 Equations of Stellar Structure

We introduce the four differential equations of stellar structure, which describe stellar structure and evolution with respect to the macrophysics. These are the mass conservation equation,

$$\frac{\partial r}{\partial m} = \frac{1}{4\pi r^2 \rho}, \tag{2.1}$$

the hydrostatic equilibrium equation,

$$\frac{\partial P}{\partial m} = -\frac{Gm}{4\pi r^4}, \tag{2.2}$$

the energy conservation equation,

$$\frac{\partial L}{\partial m} = \varepsilon - \varepsilon_\nu + \varepsilon_\mathrm{g}, \tag{2.3}$$

and the energy transport equation,

$$\frac{\partial T}{\partial m} = -\frac{GmT}{4\pi r^4 P}\nabla_T. \tag{2.4}$$

In these equations, r is the distance to the center of the star, m the mass inside the radius r, P is the pressure, ρ is the density, T is the temperature, L is the luminosity at a given position, ε is the energy rate per unit mass generated by nuclear reactions, ε_v is the energy lost by production of neutrinos, ε_g is the work performed on the gas during any expansion or contraction of the star, G is the gravitational constant, and ∇_T is the temperature gradient given by

$$\nabla_T = \frac{\partial \ln T}{\partial \ln P}. \tag{2.5}$$

The solutions to these equations are not static and present a dependence with time due to nuclear reactions taking place inside the star, which results in changes to the chemical composition and mean molecular weight. The solutions to eqs. 2.1 and 2.2 give rise to the mass profile of the star, and eqs. 2.3 and 2.4 describe the thermal profile inside the star.

2.2 Energy Transport

Energy flows from the inner layers, where nuclear reactions occur, to the outer layers of the star, and then radiates to the interstellar medium. This energy flow can take place through radiative transfer, convective motions or conductive transfer. We will not be discussing conductive transfer here, although it can be very efficient in degenerate matter conditions, such as those found in stellar cores during the red-giant phase of evolution.

2.2.1 Radiative Transport

For radiative transfer in a time-independent, three-dimensional problem it follows that

$$\mu_i \frac{\partial I}{\partial x_i} = -(\kappa_{\rm ab} + \kappa_{\rm sc})\rho I + \kappa_{\rm ab}\rho B + \kappa_{\rm sc}\rho J, \tag{2.6}$$

where $I(\mathbf{x}, \boldsymbol{\mu})$ is the specific intensity at point $\mathbf{x}$ in direction $\boldsymbol{\mu}$, $\kappa_{\rm ab}$ is the mean absorption opacity, $\kappa_{\rm sc}$ is the scatter opacity, $B = (ac/4\pi)T^4$ is the integrated Planck intensity, c is the speed of light, a is the radiation constant, and J is the mean intensity. Assuming the intensity is isotropic and using the Eddington approximation, one obtains the following expression for the radiative flux:

$$F = -\frac{4\pi}{3\rho\kappa}\nabla B = -\frac{4acT^3}{3\rho\kappa}\nabla T, \tag{2.7}$$

where $\kappa = |\kappa_{\rm ab} + \kappa_{\rm sc}|$. This is known as the diffusion approximation.

The radiative flux shows a dependence on the opacity κ, which in turn has a natural dependence on frequency. It is possible to obtain an average opacity thus rendering the problem frequency-independent. This is called the Rosseland mean opacity, and is defined as

$$\kappa^{-1} = \frac{\pi}{acT^3}\int_0^\infty \frac{1}{\kappa_\nu}\frac{\partial B_\nu}{\partial T}d\nu, \tag{2.8}$$

where B_ν is the monochromatic Planck function.

When the energy is transported by photons it is possible to derive the temperature gradient as

$$\nabla_{\rm rad} = \frac{3}{16\pi acG}\frac{\kappa LP}{mT^4}. \tag{2.9}$$

2.2.2 Transport by Convection

When radiation is not able to transport the energy, convective instabilities take place, carrying the energy by means of the motion of the stellar material. It is possible to derive a criterion for convective instabilities based on the motion of random blobs of gas inside the star. Assuming that a given blob

of gas remains at pressure equilibrium with the surrounding medium, an increase in its temperature leads to a decrease in density, if the stellar matter is to obey the ideal gas law. The blob gets lighter and is lifted upwards by the buoyancy force. Once the gas becomes unstable due to turbulence, it will dissolve into the surrounding medium. If the blob follows an adiabatic motion, the layers remain stable when

$$\nabla_{\rm rad} < \nabla_{\rm ad} + \frac{\varphi}{\delta}\nabla_{\mu}, \tag{2.10}$$

where $\nabla_{\rm ad}$ is the adiabatic gradient and $\varphi = \left(\frac{\partial \ln \rho}{\partial \ln \mu}\right)_{P,T}$, $\delta = \left(\frac{\partial \ln \rho}{\partial \ln T}\right)_{P,\mu}$, and $\nabla_{\mu} = \left(\frac{\partial \ln \mu}{\partial \ln P}\right)$. This is the Ledoux criterion for convection, which takes into account the variation of the molecular weight, μ, to define the boundaries of convection. In regions of homogeneous composition, one can instead use the Schwarzschild criterion, for which convective stability is expressed as

$$\nabla_{\rm rad} < \nabla_{\rm ad}. \tag{2.11}$$

This means, if the temperature gradient is equal or greater than the adiabatic gradient, $\nabla_{\rm ad}$, the energy is transported by convective motions.

In a radiative layer, a vertically displaced blob is pushed back by buoyancy forces. This interaction creates a momentum in the gas element, which will overshoot the original position when descending. This oscillation of the gas element can occur in the form of thin needles and when it takes place adiabatically it is characterized by the Brunt-Väisälä frequency:

$$N = \frac{g\delta}{H_P}\left(\nabla_{\rm ad} - \nabla + \frac{\varphi}{\delta}\nabla_{\mu}\right), \tag{2.12}$$

where H_P is the pressure scale height given by $H_P^{-1} = -\frac{d\ln P}{dr}$. For $N^2 > 0$, the region is convectively stable (radiative).

Once the convective region is defined by the criterion in eq. 2.11, it is necessary to define the temperature gradient. To do this, the mixing-length theory for convection (MLT) is usually employed. The critical parameter in this formulation is the mixing-length parameter, $\alpha_{\rm MLT} = l/H_P$, where l is the distance which a blob travels before dissolving into the surrounding medium. This parameter indicates how efficient is the transport of energy by convection.

2.3 Energy Production

Stars have two main mechanisms to produce energy. One such mechanism uses the gravitational potential energy of the star, being responsible for the luminosity when the other mechanism of energy production, nuclear reactions, does not occur. The former mechanism is characterized by the Kelvin–Helmholtz timescale:

$$\tau_{\rm kh} \simeq \frac{GM_*^2}{2R_*L_*}, \tag{2.13}$$

where R_* is the stellar radius, M_* is the total mass of the star, and L_* is the luminosity of the star.

The latter mechanism is characterized by a nuclear timescale,

$$\tau_{\rm nuc} = \frac{\beta q M_* c^2}{L_*}, \tag{2.14}$$

where β is the amount of mass converted into energy, and q is the fraction of total mass involved in the nuclear burning. This describes for how long the star can shine with nuclear reactions as the only source of energy. Comparing the two timescales above, we find $\tau_{\rm nuc} \gg \tau_{\rm kh}$, which indicates that the star has a longer lifetime during evolutionary phases dominated by nuclear reactions.

All stars on the main sequence produce energy through nuclear reactions by burning hydrogen ^{1}H into helium ^{4}He. There are two types of chains performing this reaction: the p-p chain, which burns hydrogen directly; and the CNO cycle, which uses carbon (C), nitrogen (N), and oxygen (O) as catalysts.

Table 2.1: Diagrams of the p-p chain (top) and CNO cycle (bottom).

p-p chain

pp I	pp II	pp III
^{1}H+^{1}H$\longrightarrow$ ^{2}D+e$^+$+ν_e	^{3}He+^{4}He$\longrightarrow$ ^{7}Be+γ	^{3}He+^{4}He$\longrightarrow$ ^{7}Be+γ
^{2}D+^{1}H$\longrightarrow$ ^{3}He+γ	^{7}Be+e$^-$ $\longrightarrow$ ^{7}Li+ν_e	^{7}Be+^{1}H$\longrightarrow$ ^{8}B+γ
^{4}He+^{4}He$\longrightarrow$^{4}He+^{1}H+^{1}H	^{7}Li+^{1}H$\longrightarrow$ ^{4}He+^{4}He	^{8}B$\longrightarrow$ ^{8}Be+e$^+$+ν_e
		^{8}Be$\longrightarrow$ ^{4}He+^{4}He

CNO cycle

CN cycle	ON cycle
^{12}C+^{1}H$\longrightarrow$^{13}N+γ	^{15}N+^{1}H$\longrightarrow$ ^{16}O+γ
^{13}N$\longrightarrow$ ^{13}C+e^++ν_e	^{16}O+^{1}H$\longrightarrow$ ^{17}F+γ
^{13}C+^{1}H$\longrightarrow$ ^{14}N+γ	^{17}F$\longrightarrow$ ^{17}O+e$^+$+ν_e
^{14}N+^{1}H$\longrightarrow$ ^{15}O+γ	^{17}O$\longrightarrow$ ^{14}N +^{4}He
^{15}O$\longrightarrow$ ^{15}N+e$^+$+ν_e	
^{15}N+^{1}H$\longrightarrow$ ^{12}C+^{4}He	

These two processes occur simultaneously inside the star, with the dominant one depending on the central temperature of the star. For high temperatures, the CNO cycle is the main process producing energy, while for low temperatures the p-p chain dominates. The central temperature depends mainly on the mass of the star. The more massive a star is, the higher is its central temperature, thus the CNO cycle occurs in more massive stars. The more massive stars confine the production of energy very close to the center of the star and, since they have a CNO cycle as the dominant process, they present a greater flux of energy through the inner layers, which gives rise to convection in the stellar core.

Depending on the mass of the star, the star can have different stages of nuclear reactions. One of them is the helium-burning phase once the hydrogen in the core has been exhausted. This only occurs when the star reaches a central temperature high enough to burn helium via the triple alpha reaction, where it uses three helium atoms to produce a carbon atom,

$$^4\mathrm{He} + ^4\mathrm{He} \longrightarrow {}^8\mathrm{Be}$$

$$^8\mathrm{Be} + ^4\mathrm{He} \longrightarrow {}^{12}\mathrm{C} + \gamma.$$

Finally, the helium can be burned in two more nuclear reactions,

$$^{12}\mathrm{C} + ^4\mathrm{He} \longrightarrow {}^{16}\mathrm{O} + \gamma$$

$$^{16}\mathrm{O} + ^4\mathrm{He} \longrightarrow {}^{20}\mathrm{Ne} + \gamma,$$

showing that ^{4}He will transform mainly into ^{12}C, ^{16}O and ^{20}Ne.

2.4 The HR Diagram

We have seen the stellar physics related to observational parameters such as the effective temperature, $T_{\rm eff}$, stellar luminosity, L_*, and the iron content, [Fe/H]. The $T_{\rm eff}$ and [Fe/H] are commonly obtained by spectrometric observations. The iron content is related to the metallicity Z and the abundance of hydrogen X in the star by

$$[\mathrm{Fe/H}] = \log\left(\frac{Z_{\rm star}}{X_{\rm star}}\right) - \log\left(\frac{Z_\odot}{X_\odot}\right), \tag{2.15}$$

where $Z_\odot$ and $X_\odot$ refer to the Sun. Variations in Z affect the abundance of hydrogen (X) and helium (Y) in the star, which, in turn, will affect the mean molecular weight and, consequently, the production and transport of energy in the star, leading to a different $T_{\rm eff}$ and L_*.

The stellar luminosity, L_*, and the radius of the star, R_*, are commonly obtained by photometric

observations. It is only necessary to determine one of these two parameters, since they are related through

$$L_* = 4\pi\sigma R_*^2 T_{\rm eff}^4, \tag{2.16}$$

where σ is the Stefan–Boltzmann constant. This way, the radius can be estimated from a parallax measurement and, using eq. 2.16, we can obtain L_*. Or instead we can determine the luminosity using the extinction and parallax of the star, as expressed by

$$\log(L/{\rm L}_\odot) = 4.0 + 0.4 M_{\rm bol,\odot} - 2.0\log(\pi[{\rm mas}]) - 0.4({\rm V} - {\rm A_V} + {\rm BC_V}), \tag{2.17}$$

where $M_{\rm bol,\odot}$ is the bolometric magnitude of the Sun with a value of 4.73 mag, π is the parallax of the star, V is the magnitude of the star in the V band, A_V is the extinction in the V band, and BC_V is the bolometric correction [17].

Having L_* and $T_{\rm eff}$, we can locate the different stars in a Hertzsprung–Russell (HR) diagram (see Fig. 2.1), allowing us to locate each star on its evolution track.

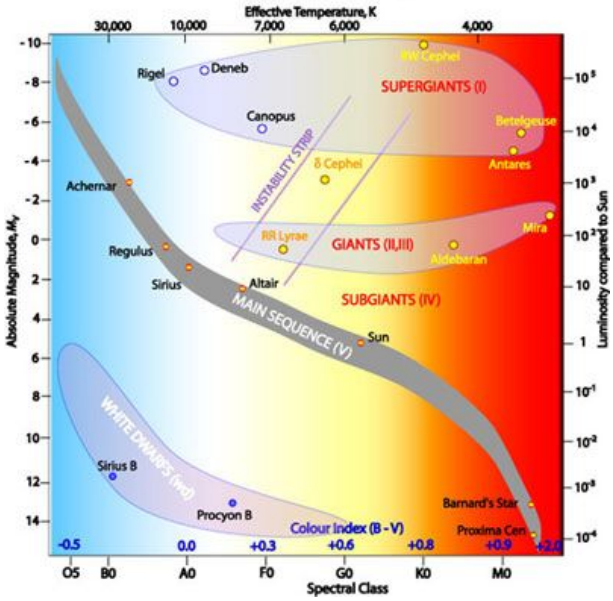

Figure 2.1: HR diagram showing the evolutionary stages of the different types of stars [credit: R. Hollow, CSIRO].

The position in the HR diagram is affected by the total mass of the star, M_*, by its chemical composition, (which changes with the time due to nuclear reaction processes), the mixing-length parameter, $\alpha_{\rm MLT}$, among other parameters. We will first examine how the stars studied here evolve and, afterwards, we will see how changing these parameters affects their evolution. In Fig. 2.2, the evolution of a solar-type star has been represented which presents a similar evolution of the stars under study that have values of M_* in the interval of $[0.7, 1.7]$ M$_\odot$.

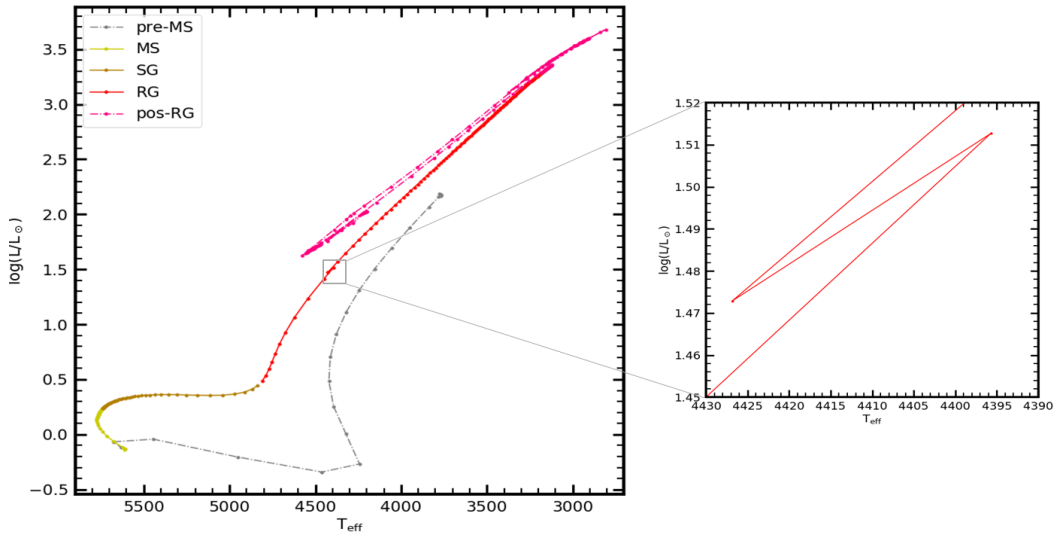

Figure 2.2: Hertzsprung–Russell (HR) diagram showing the evolution of a star with $M_* = 1.0\mathrm{M}_\odot$, $Z = 0.018$, and $\alpha_{\mathrm{MLT}} = 1.8$.

2.5 Stellar Evolution

Stars begin their evolution in the pre-main sequence (pre-MS) as protostars. They form from the gravitational collapse of subunits of a giant molecular gas cloud. These subregions form a hydrostatic core and accrete the gas from its surroundings, presenting two phases of evolution. The first phase follows the Hayashi track, characterized by a fully convective interior. During this phase, the stars contract, decreasing their L_*, and changes in their T_{eff} are small. The second phase follows the Henyey track, where a radiative core appears. During this phase, the protostars continue their contraction but this time exhibit a substantial increase in T_{eff}, with a small accompanying change in L_*, following an almost horizontal path on the HR diagram. For different masses and metallicities, the radiative zone can present different extensions, and for sufficiently mas-

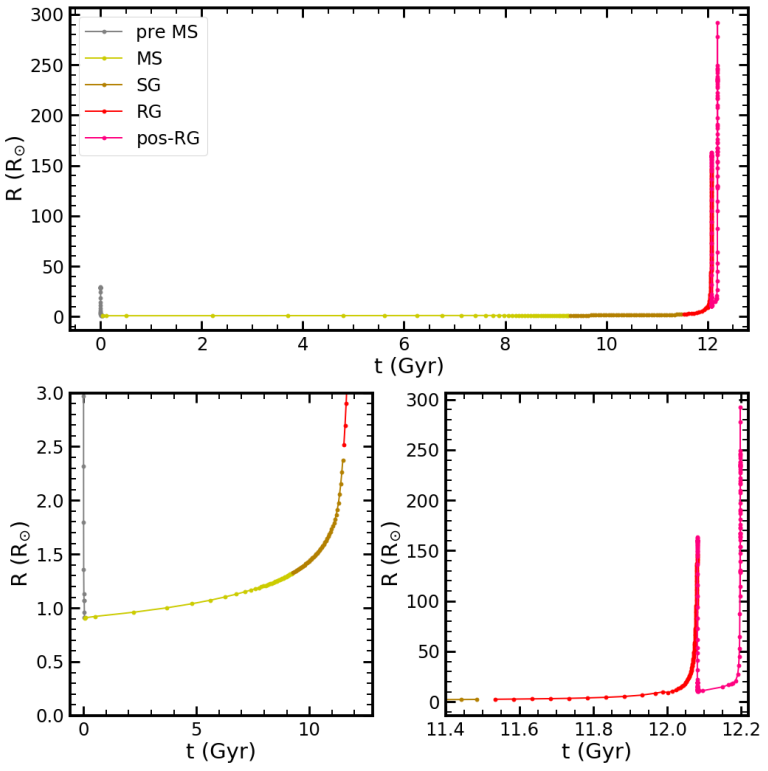

Figure 2.3: Evolution of the stellar radius with time for the same star depicted in Fig. 2.2.

sive stars, a convective core can appear within the radiative zone (this is visible in Fig. 2.9a). During all these phases the protostars are contracting, thus raising their central temperature until it is hight enough to start burning hydrogen in the core. When stars reach the Zero Age Main Sequence (ZAMS), they are fully formed and begin the second stage of their lives, the main sequence (MS).

The MS is the longest evolutionary stage. During this phase, contraction stops and stars enter an equilibrium state whereby their energy is produced due to the transformation of ^{1}H into helium ^{4}He, in the stellar core. This stage ends when the star burns all its ^{1}H in the center. The stars considered, at this stage, do not possess a high enough central temperature to immediately ignite the ^{4}He, and so they advance to the subgiant phase (SG). During the MS, it is possible to see a variation in L_* and $T_{\rm eff}$. This can be explained by the change of a star's internal chemical composition, i.e., the decrease in the hydrogen abundance X and corresponding increase in the helium abundance Y.

During the subgiant phase, once stars burn all their ^{1}H, they leave the equilibrium state. They then start to contract their inner layers, raising their central temperature and burning hydrogen in a shell around the core. However, this is not sufficient to reestablish the equilibrium, leading to a continued contraction of the inner layers of stars. In contrast, the outer layers expand, which leads to a decrease in $T_{\rm eff}$ at almost constant L_*. This phase ends when the convective envelope significantly expands and the stellar core contracts substantially and changes into a degenerate state (whereas until now it was considerated an ideal gas). Stars transit to the next stage of evolution, the Red-Giant (RG) branch.

The RG phase comes with a drastic expansion of the outer layers, and a small change in $T_{\rm eff}$. Stars develop a deep convective envelope which, at its maximum depth, diffuses some of the nuclear material throughout the star. This is the so-called first dredge-up. After this, the convective envelope starts to retreat leaving behind a chemical discontinuity.

The inner layers of these stars continue their contraction, increasing the central temperature. In the meantime, the hydrogen shell continues to burn, depositing helium in the core and increasing its mass. When the burning shell reaches the chemical discontinuity left during the first dredge-up, the star decreases its luminosity due to the abrupt decrease in mean molecular weight in this region. After the burning shell passes this discontinuity, the star continues its normal development while increasing its luminosity. In the HR diagram of Fig. 2.2, it is possible to see this phenomenon, called the luminosity bump.

The end of the red-giant phase is reached when the central temperature is high enough to ignite helium burning, the so-called helium flash. When this occurs, all the energy produced is used to remove the core degeneracy. Then, when the core is no longer degenerate, the stars reach the horizontal branch. At this stage, stars burn helium quiescently in a convective core while they continue their

hydrogen shell burning. Their outer layers contract, which leads to a decrease in their luminosity. Once helium is exhausted in the core, stars move to the asymptotic giant branch, at which point they expand once again. At the end of their lives, the outer layers escape the gravity of the stars, forming a planetary nebula and leaving behind the stellar core, which becomes a white dwarf [1, 18].

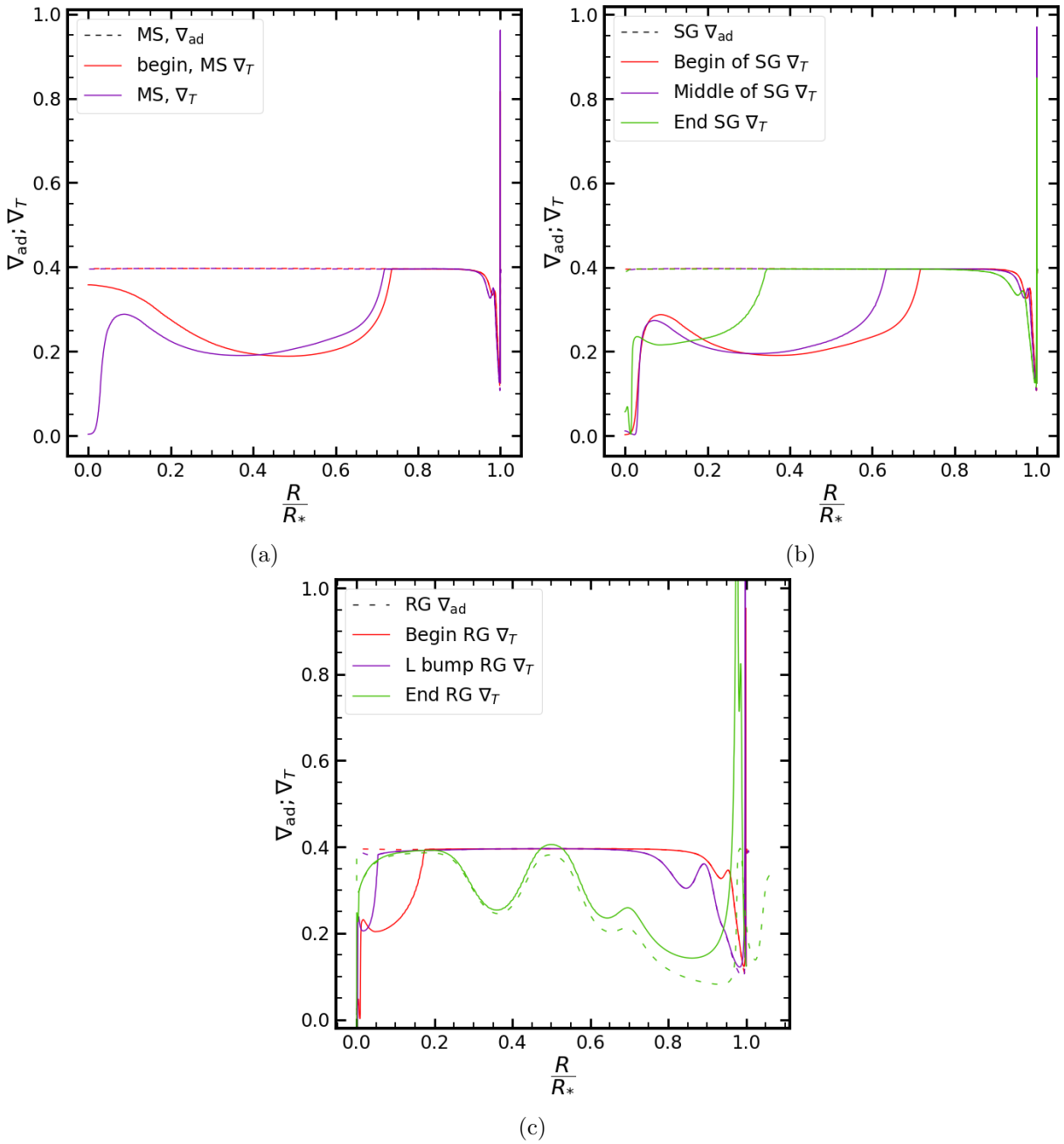

Figure 2.4: Stellar profiles for ∇_T and ∇_{ad} inside the same star depicted in Fig. 2.2 at different evolutionary stages. Zones where $\nabla_T < \nabla_{ad}$ are radiative regions. Panel (a) shows the initial and final models on the main sequence; panel (b) shows the initial, the intermediate and the final models in the subgiant phase; and panel (c) shows the initial and the final models in the red-giant phase, as well as a model at the luminosity bump. The x axis represents the fractional radius of the star. For panels (a) and (b) the ∇_{ad} is represented for the different models, overlapping each other.

We can trace a series of changes in the star along its evolutionary path. In Fig. 2.3, we can see the evolution of the stellar radius along the different stages of evolution, where it can be seen that, following the pre-MS, the radius continually increases, this increase being more pronounced during the reg-giant phase. In Fig. 2.4, we can see its temperature gradient ∇_T and adiabatic gradient $\nabla_{\rm ad}$, at different evolutionary stages. During the main sequence, the star has a small convective envelope that increases substantially during the subgiant and reaches its maximum extent during the red-giant phase.

Figure 2.5 illustrates the evolution of the central temperature, $T_{\rm c}$, and the central density, $\rho_{\rm c}$, in the core of the star. Up until the red-giant phase the gas in the core can be considered an ideal gas. During the RG phase, the core is in a degenerate, state until the occurrence of the helium flash, when it transits to the ideal gas state. When the core turns non-degenerate, the stars starts burning the helium present in the central region. When it runs out of helium, the core goes again into a degenerate state and it remains like that.

This is, in general, the evolution of low-mass, solar-type stars. Now we will see how the star changes when we vary some of the initial parameters like the mass (M_*), metallicity (Z), and mixing length parameter ($\alpha_{\rm MLT}$), and when we vary some of the physics such as introducing diffusion in the models.

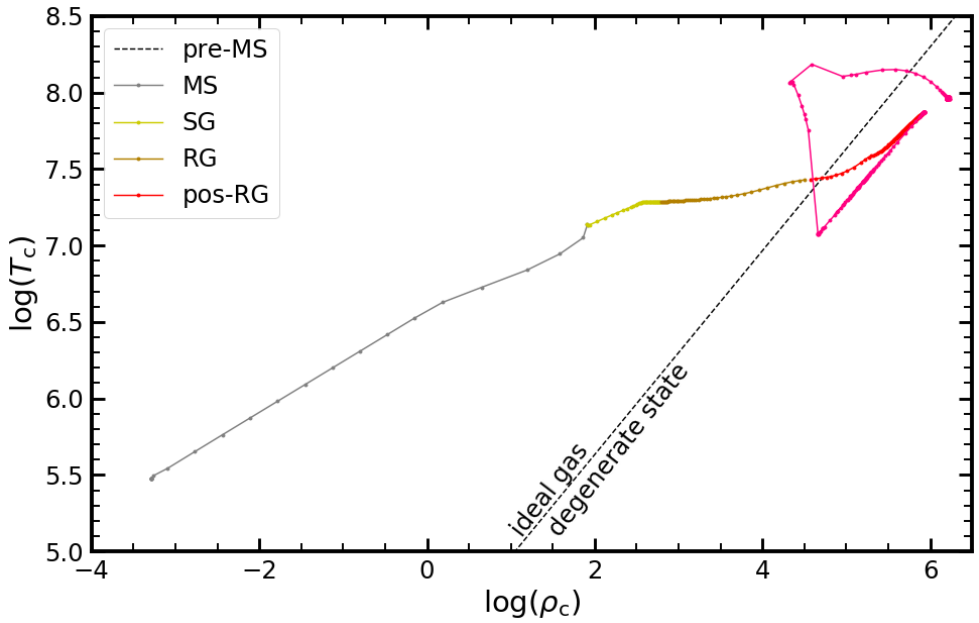

Figure 2.5: Logarithm of the central temperature versus the logarithm of density for the same star depicted in Fig. 2.2 at different evolutionary stages. The dashed line represents the approximate transition between an ideal gas and a degenerate gas.

2.5.1 Effect of Mass

Now we will change the M_* and see how this affects stellar evolution. Figure 2.6a shows the evolutionary tracks of stars with total mass in the interval $[0.8, 1.2]$ $M_\odot$ in steps of 0.05 $M_\odot$, with initial $Z = 0.018$, $\alpha_{\rm MLT} = 1.8$, and no diffusion.

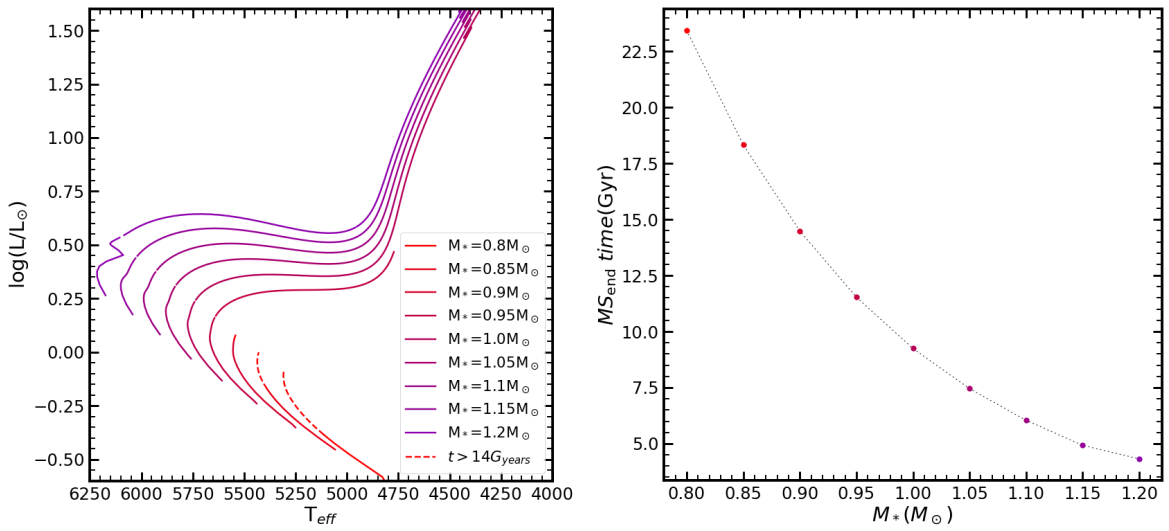

(a) (b)

Figure 2.6: (a) HR diagram showing stars with different masses; (b) Estimated age at the end of the Main Sequence for different masses.

We see that changes in the mass produce significant changes in the HR diagram. Higher-mass stars present higher L_* and $T_{\rm eff}$ than lower-mass stars, but also a faster evolution. The lowest-mass stars present an age higher than that of the Universe ($\sim$ 14Gyr); see Fig. 2.6b.

For stars with $\gtrsim 1.1 M_\odot$, a hook starts appearing [18] (there is also a dependence in Z), being perfectly visible for the $1.2 M_\odot$ evolutionary track. This hook appears in stars with convective cores and occurs when the hydrogen is almost depleted. In order to maintain the energy production constant, the star contracts. This event leads to an increase in effective temperature and luminosity until the hydrogen is completely burned at the center [18].

We look now at the stellar interiors. The central temperature increases with mass, its evolution occurring in parallel (with respect to mass) until the RG phase, at which point paths converge (see Fig. 2.7). Based on the gradient profiles in Fig. 2.9, we see that profiles have a convective region in the outer layers, whose extension decreases with increasing mass. The only convective core develops for the 1.2 $M_\odot$ model at the beginning of the MS.

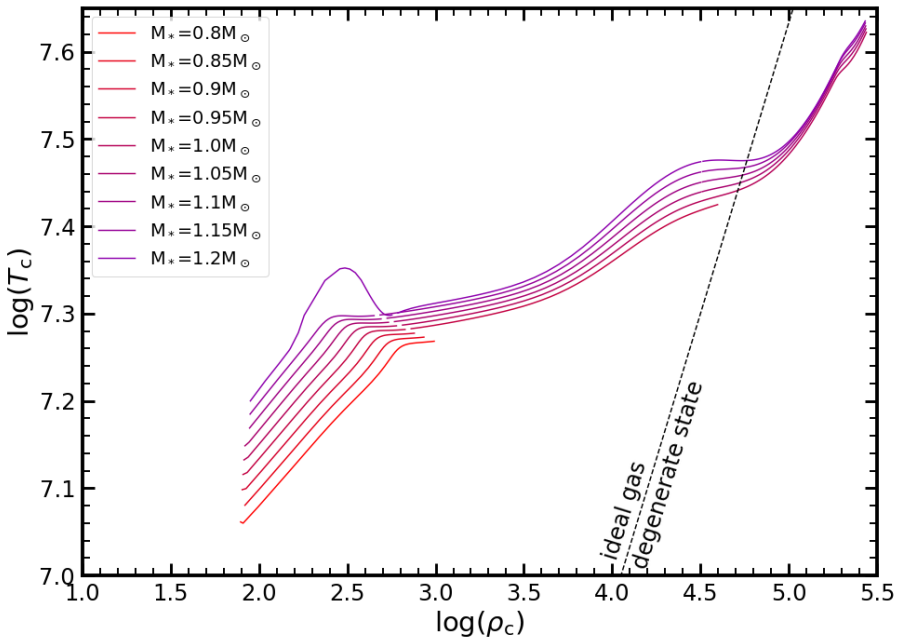

Figure 2.7: $\log(T_c)$ versus $\log(\rho_c)$ for stars of distinct mass at different evolutionary stages.

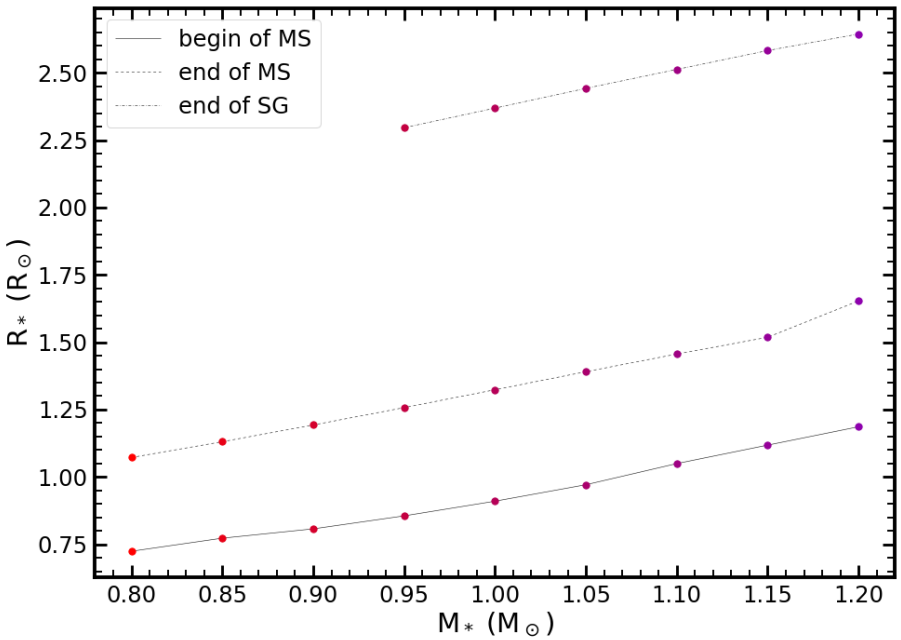

Figure 2.8: Radii of stars of distinct mass at approximately the same given point of evolution.

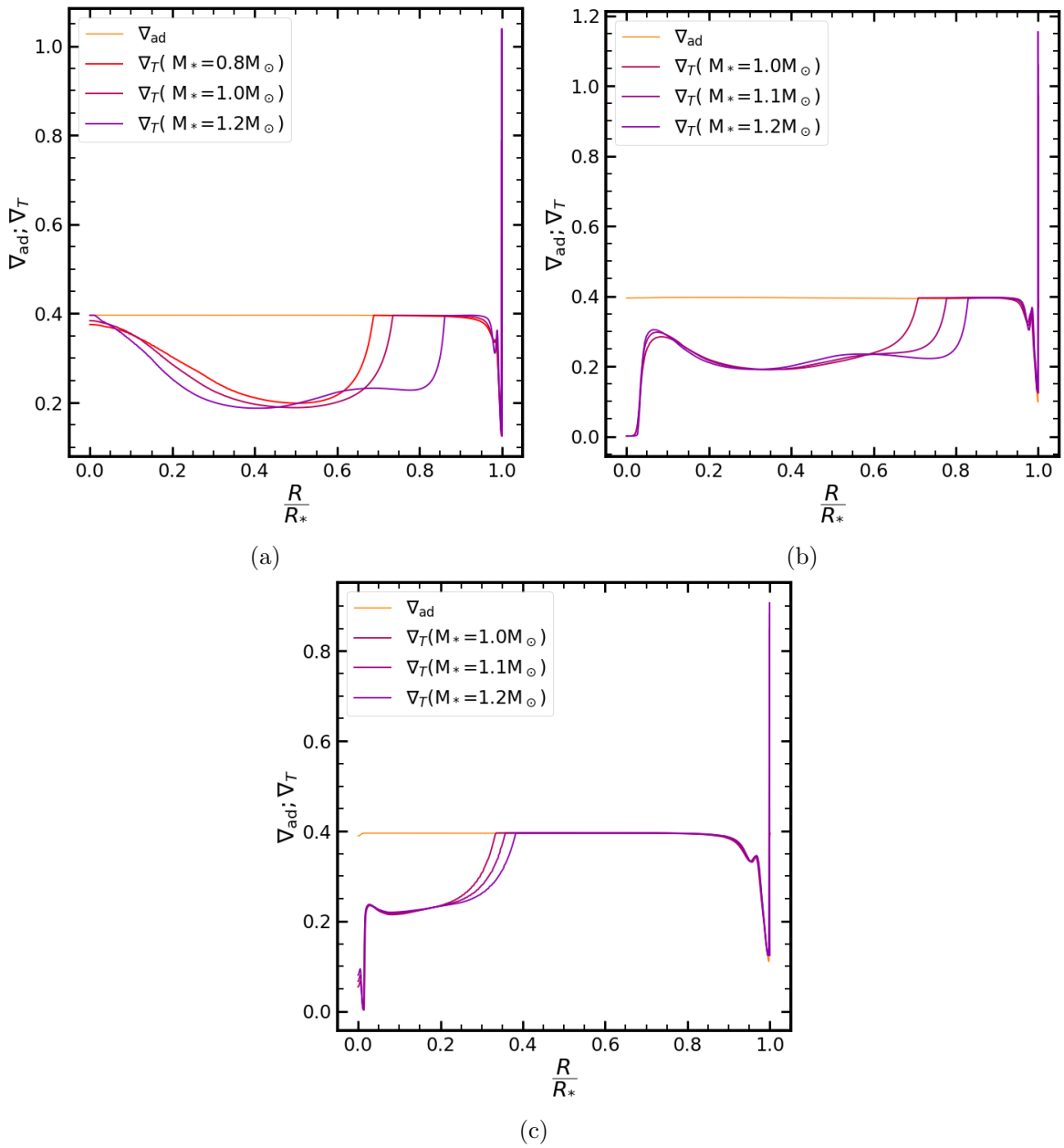

Figure 2.9: (a) Gradients at the beginning of the MS; (b) Gradients at the end of the MS/beginning of SG phase; (c) Gradients at end of the SG/beginning of the RG phase. Gradients are given as a function of the fractional radius for three different values of the stellar mass. For all models the $\nabla_{\rm ad}$ are almost the same and overlap.

2.5.2 Effect of Metallicity

Now, we will see how Z affects stellar evolution. To do this, we used metallicities in the interval $[0.010, 0.026]$ in steps of 0.004, with mass $M_* = 0.95$ $M_\odot$, mixing-length parameter $\alpha_{\rm MLT} = 1.8$, and no diffusion. In Fig. 2.10, the evolution of the corresponding evolutionary tracks in the HR diagram is represented.

When we change the initial Z of the star, we also change the initial abundance of the hydrogen (X) and helium (Y). These three parameters are related by the expression

$$X + Y + Z = 1. \tag{2.18}$$

We can determine Z through spectroscopy, but we can not observe the spectral lines of helium for the type of stars being considered. Then, it is necessary to use a second equation to relate Z with the other two abundances. For this we can use the helium enrichment law,

$$Y = \left(\frac{\Delta Y}{\Delta Z}\right) Z + Y_0, \tag{2.19}$$

where $Y_0 = 0.2484$ [15] is the value at the Big Bang nucleosynthesis, when $Z = 0$. $\frac{\Delta Y}{\Delta Z}$ is the helium enrichment ratio, which can be determined observationally. However, this parameter is still poorly constrained. We will work on this problem later. For now, we will see the effects of changing the metallicity, where we have assumed $\frac{\Delta Y}{\Delta Z} = 1.4$.

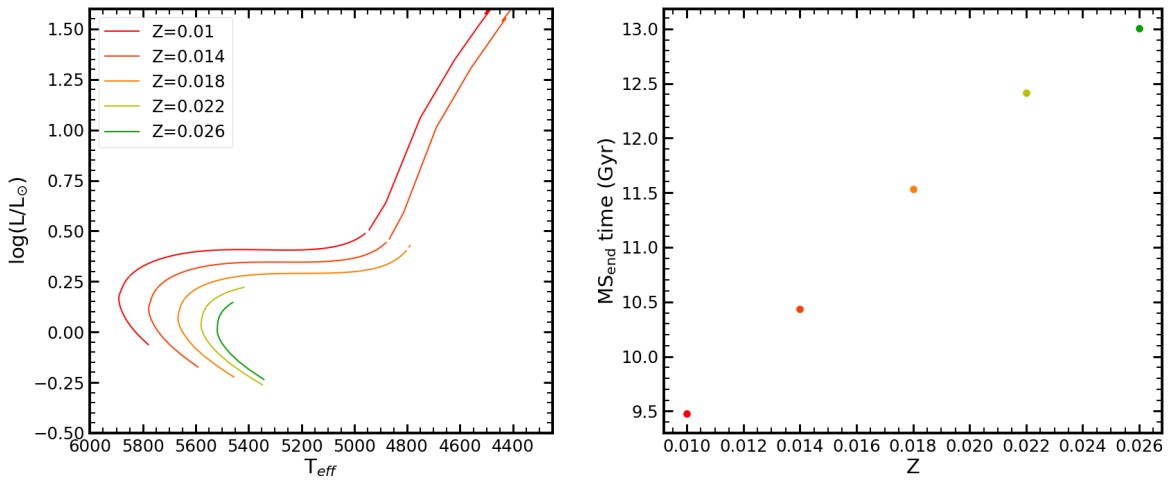

(a) (b)

Figure 2.10: (a) HR diagram showing stars with different metallicity; (b) Estimated age at the end of the Main Sequence stage.

Looking at Fig. 2.10a, we see that the increase of Z affects the luminosity and effective temperature of the star. Increasing Z leads to an increase of the stellar opacity, which complicates the transport of energy to the surface and hence results in decreasing $T_{\rm eff}$ and L_*. Evolution takes longer for stars with higher metallicity, as we can see from Fig. 2.10b.

Looking at the evolution of the stellar interiors (see Fig. 2.11), we do not see significant changes as a result of changing the metallicity of the star. The central temperature and density are virtually the same during the MS and RG phase, irrespective of Z, only showing a slight difference during the subgiant phase. The convective regions in Fig. 2.13 have a similar evolution throughout the different stages of evolution, presenting a more extended envelope at higher metallicities. This is due to the increase in opacity with Z, as the star transports energy more efficiently through convection. Figure 2.12 shows that, for a given evolutionary stage, the radius does not have a marked difference, although we notice a small decrease of the radius with increasing metallicity. Across the different evolutionary stages the radii of the stars increases as expected.

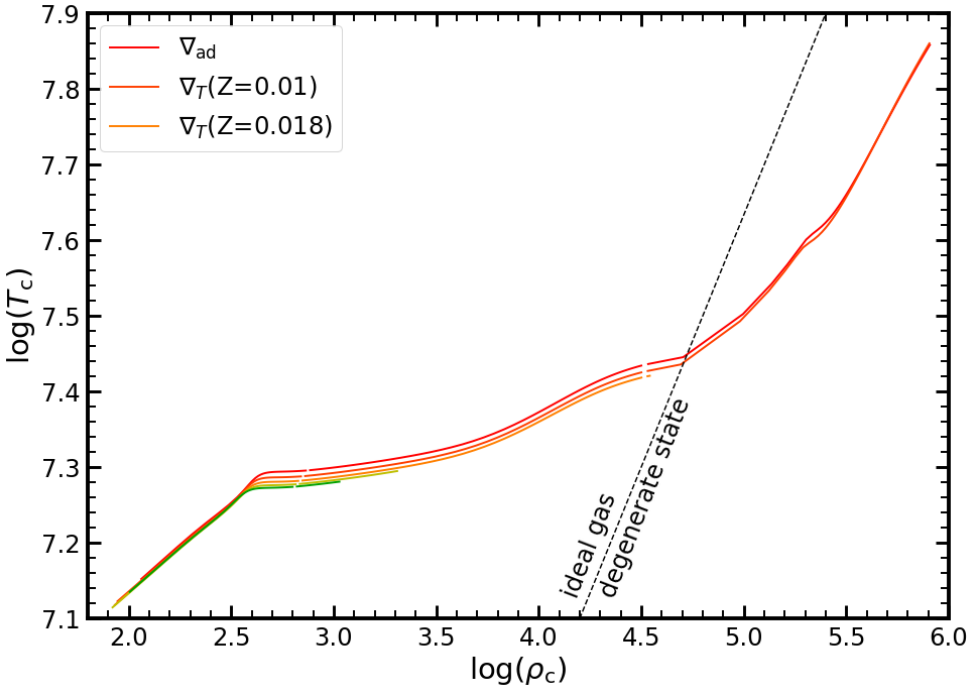

Figure 2.11: $\log(T_{\rm c})$ versus $\log(\rho_{\rm c})$ for star of different metallicity.

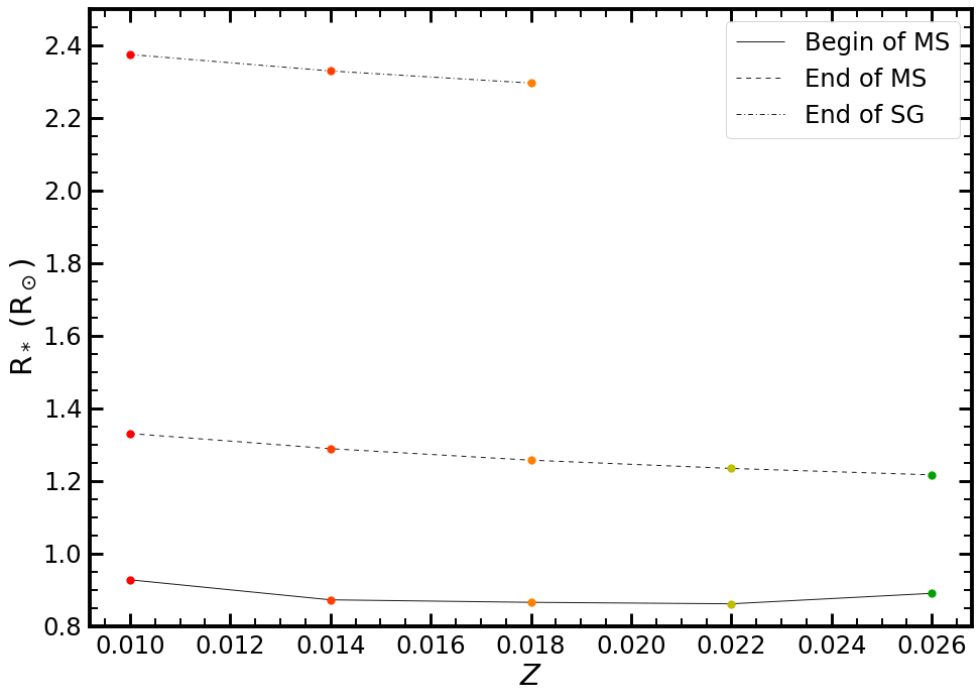

Figure 2.12: Radii of stars with different Z at approximately the same given point of evolution.

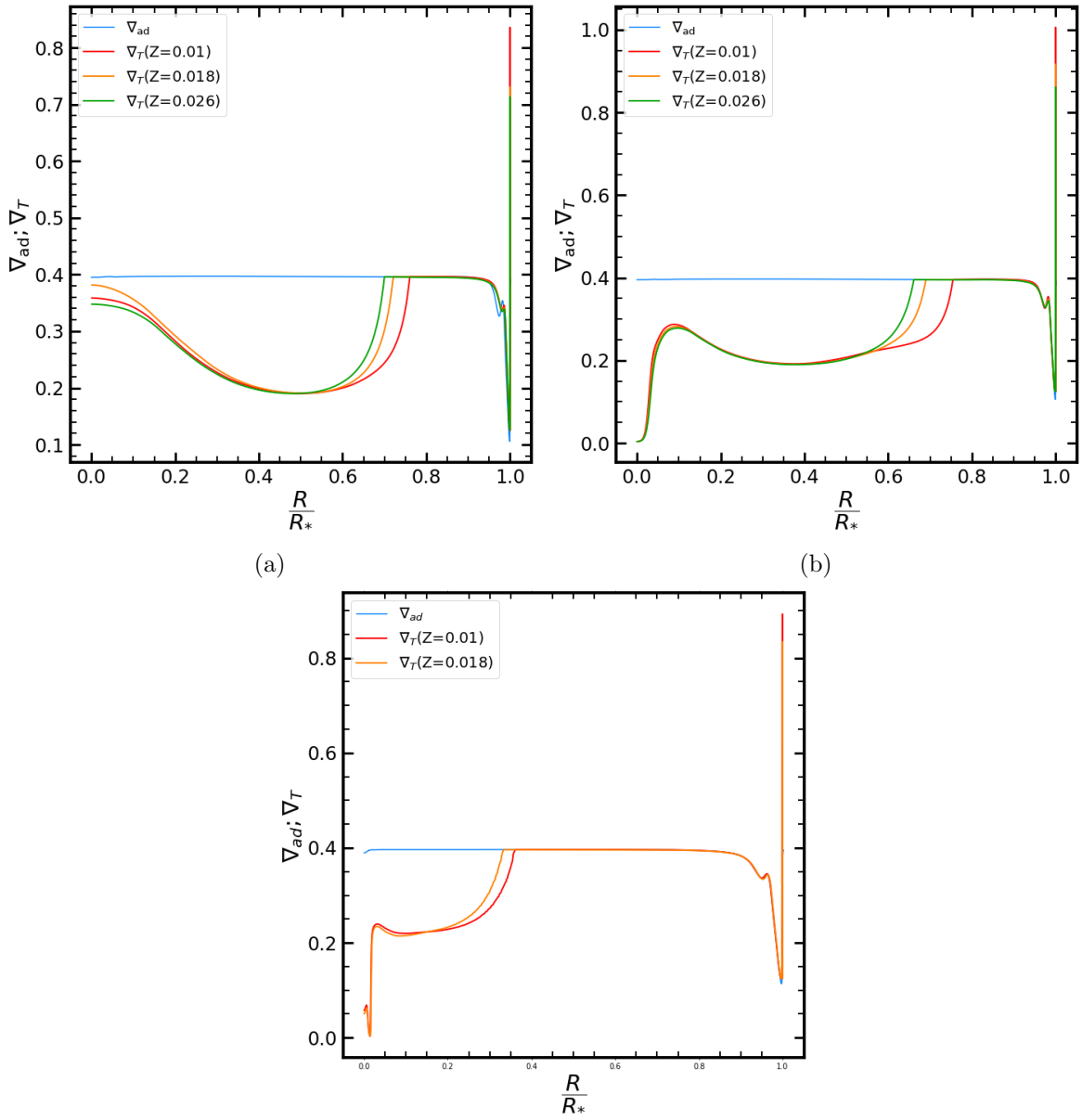

Figure 2.13: (a) Gradients at the beginning of the MS; (b) Gradients at the end of the MS/ beginning of the SG phase; (c) Gradients at the end of the SG/ beginning of the RG phase. For all models the $\nabla_{\rm ad}$ are almost the same and overlap.

2.5.3 Mixing Length Parameter

This time, we will see how the $\alpha_{\rm MLT}$ parameter affects stellar evolution. For this, we vary the mixing length parameter ($\alpha_{\rm MLT}$) in the interval $[1.0, 3.0]$ in steps of 0.4 and show in Fig. 2.14 an HR diagram for a star with $M_* = 1.0 M_\odot$ and $Z = 0.018$.

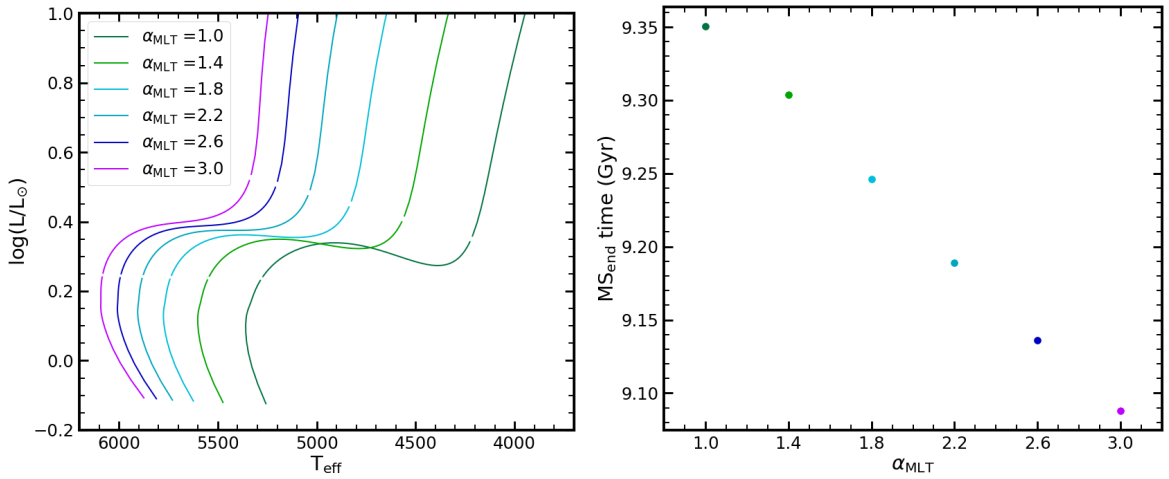

(a) (b)

Figure 2.14: (a) HR diagram showing stars with different values of the mixing length parameter; (b) Estimated age at the end of the Main Sequence.

By increasing this parameter we see a translation of the evolutionary tracks in the HR diagram, with an increase in $T_{\rm eff}$ with $\alpha_{\rm MLT}$ at approximately constant luminosity. $\alpha_{\rm MLT}$ is related to the efficiency of energy transport in convective regions, with higher values meaning the more easily the matter in convective regions is transported. This implies it has less time to decrease its temperature until reaching the surface. Differences in age at the end of the MS are of the order of a few tens of Myr, an order of magnitude less compared to changes when varying the mass and/or metallicity.

At the stellar center, models have a similar temperature and density along most of their evolution (see Fig. 2.15), starting to present some differences at the end of the SG phase, probably due to their convection regions becoming more extended. Looking at the radius of the star for a given stage of evolution, we see a decrease with increasing $\alpha_{\rm MLT}$ (see Fig. 2.16), which is expected according to eq. 2.16. Their convection layers appear to be similar at different stages of evolution (see Fig. 2.17).

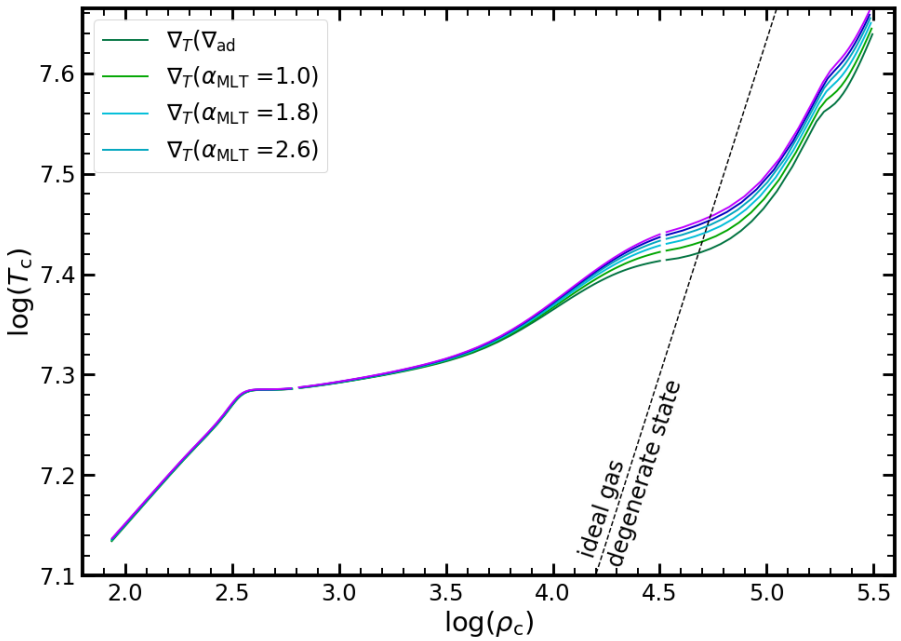

Figure 2.15: $\log(T_c)$ versus $\log(\rho_c)$ for stars with different α_{MLT}.

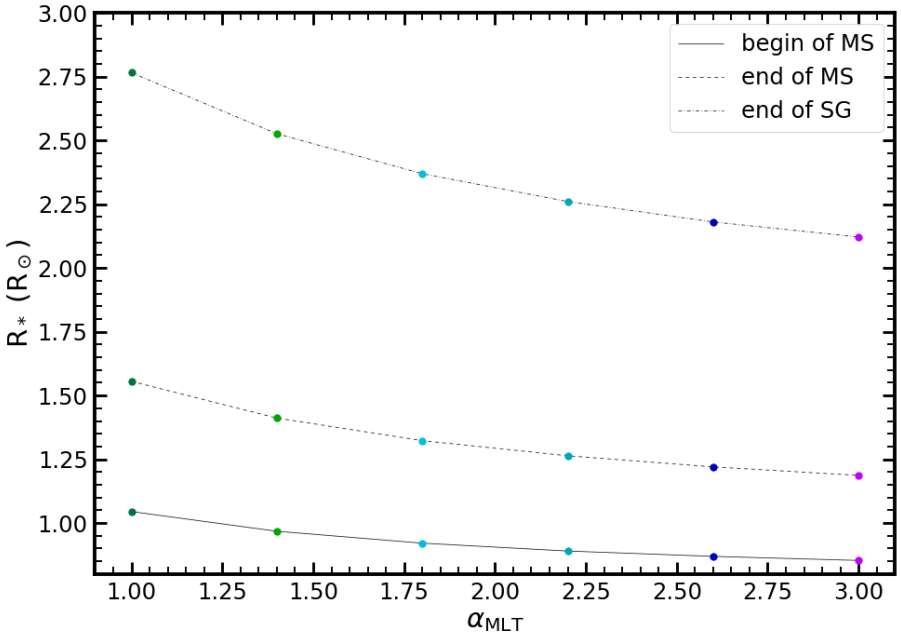

Figure 2.16: Radii of stars with different α_{MLT} at approximately the same given point of evolution.

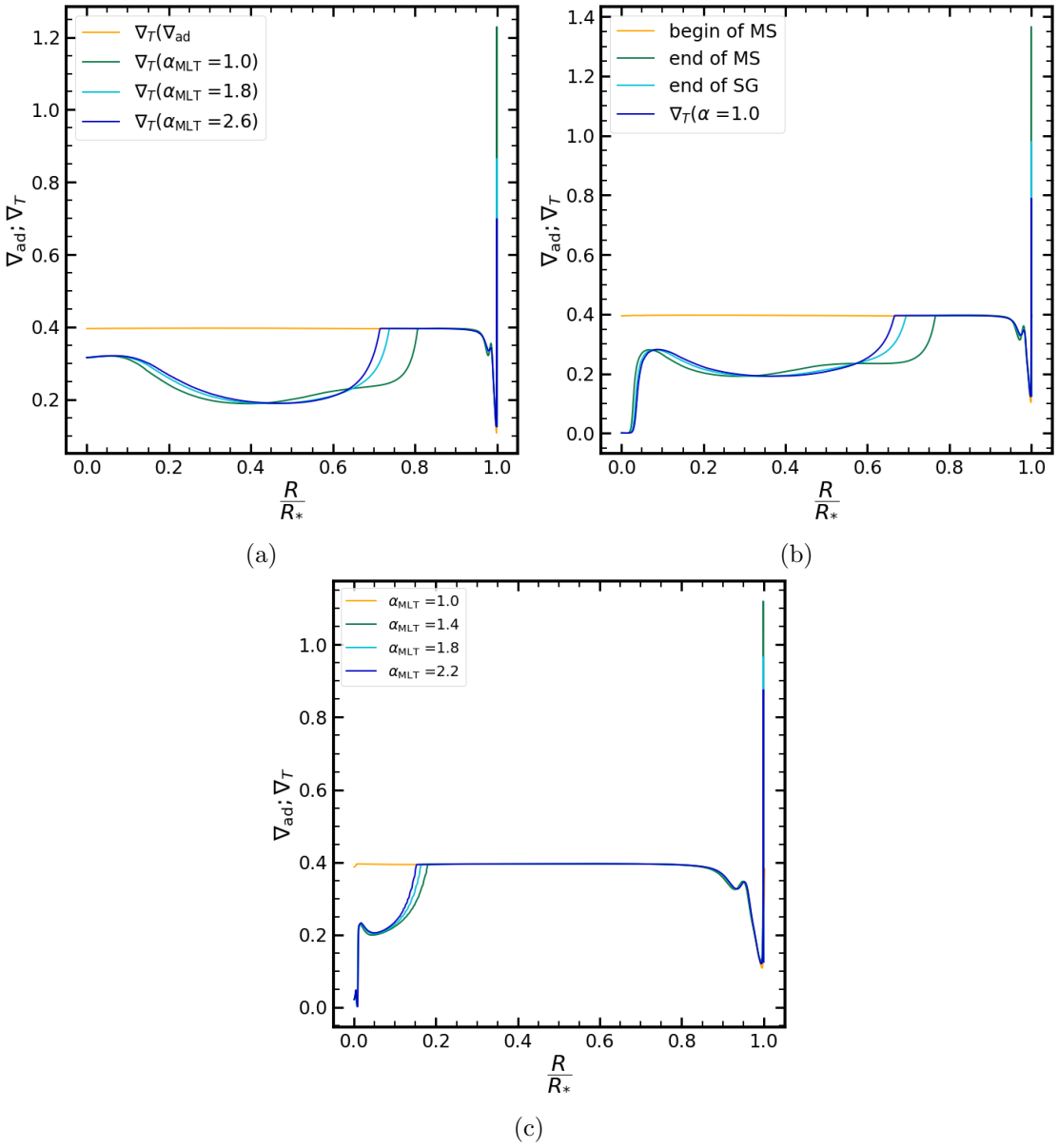

Figure 2.17: Stars with different mixing-length parameter. (a) Gradients at the beginning of the MS; (b) Gradients at the end of the MS/ beginning of the SG phase; (c) Gradients at the end of the SG/ beginning of the RG phase. For all models the ∇_{ad} are almost the same and overlap.

2.5.4 Atomic Diffusion

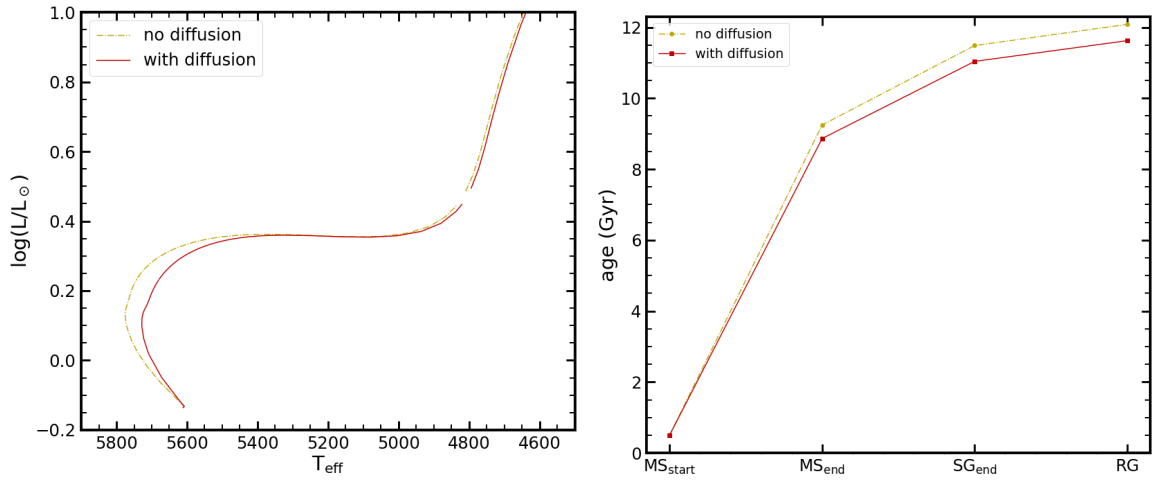

(a) (b)

Figure 2.18: (a) HR diagram showing evolutionary tracks for a solar-type star with and without diffusion. (b) Stellar age along the main stages of evolution for the same star in panel (a).

Previously, we saw how a star evolves without the presence of additional mixing processes, specifically, atomic diffusion. Atomic diffusion affects the chemical composition of the star by causing the migration of helium and some heavy elements from the surface to the center, and hydrogen in the opposite way [19]. This will not only impact the evolution of the star, but also the determination of modeled frequencies [20]. Atomic diffusion will be implemented during model construction to obtain a better match with observations.

This process is usually more effective in radiative regions than in convective regions, due to the timescale of this phenomenon being larger than the timescale of convection [19]. This happens due to the existence of different gradients in the interior of the star: gravitational settling which is induced by pressure gradients, thermal diffusion which is induced by temperature gradients, and chemical diffusion which is induced by differences in element abundances [20].

We modeled two stars, both with M_* =1M$_\odot$, $Z = 0.018$, and $\alpha_{\rm MLT} = 1.8$. In Fig. 2.18, we see a difference in $T_{\rm eff}$ during the main sequence, when including diffusion. During the later phases of evolution, the convective envelope is more extense and its effect dominates over the diffusion effect, thus explaining the nearly indistinguishable evolutionary tracks. For the stellar age, a difference appears during the MS. The star with diffusion evolves faster, which is to be expected since part of the hydrogen is transported to the surface due to diffusion. In their interior, it is possible to observe a small difference in the central temperature, starting on the MS and extending to the end of the SG phase.

For the helium and hydrogen, we can see in Fig. 2.20 different internal profiles of the star at dif-

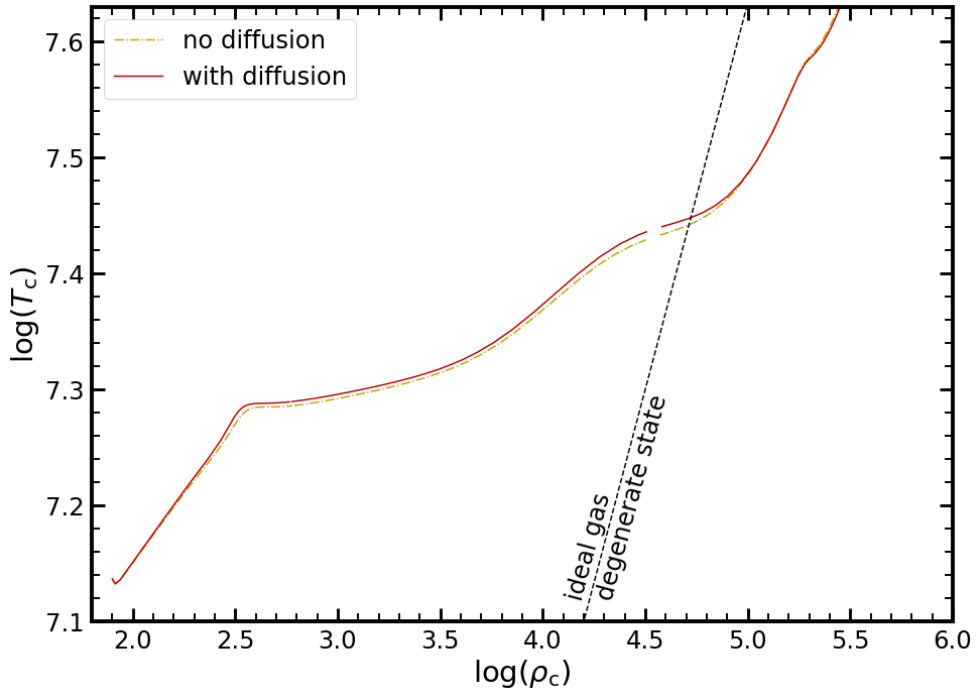

Figure 2.19: $\log(T_c)$ vs. $\log(\rho_c)$ for stars with and without diffusion.

ferent ages along the MS. At the beginning of the main sequence, the star has a homogeneous interior, but, along its evolution, the star burns hydrogen in the core, forming helium, until the core is depleted. A difference that arises when including diffusion is that the decrease of hydrogen is faster due to its migration to the surface and the opposite happening for helium. With no diffusion included, the abundances of hydrogen and helium beyond the core are constant. However, the inclusion of diffusion induces an increase/decrease in their abundances, respectively. Within the convective envelope, their abundances are, nevertheless, homogeneous.

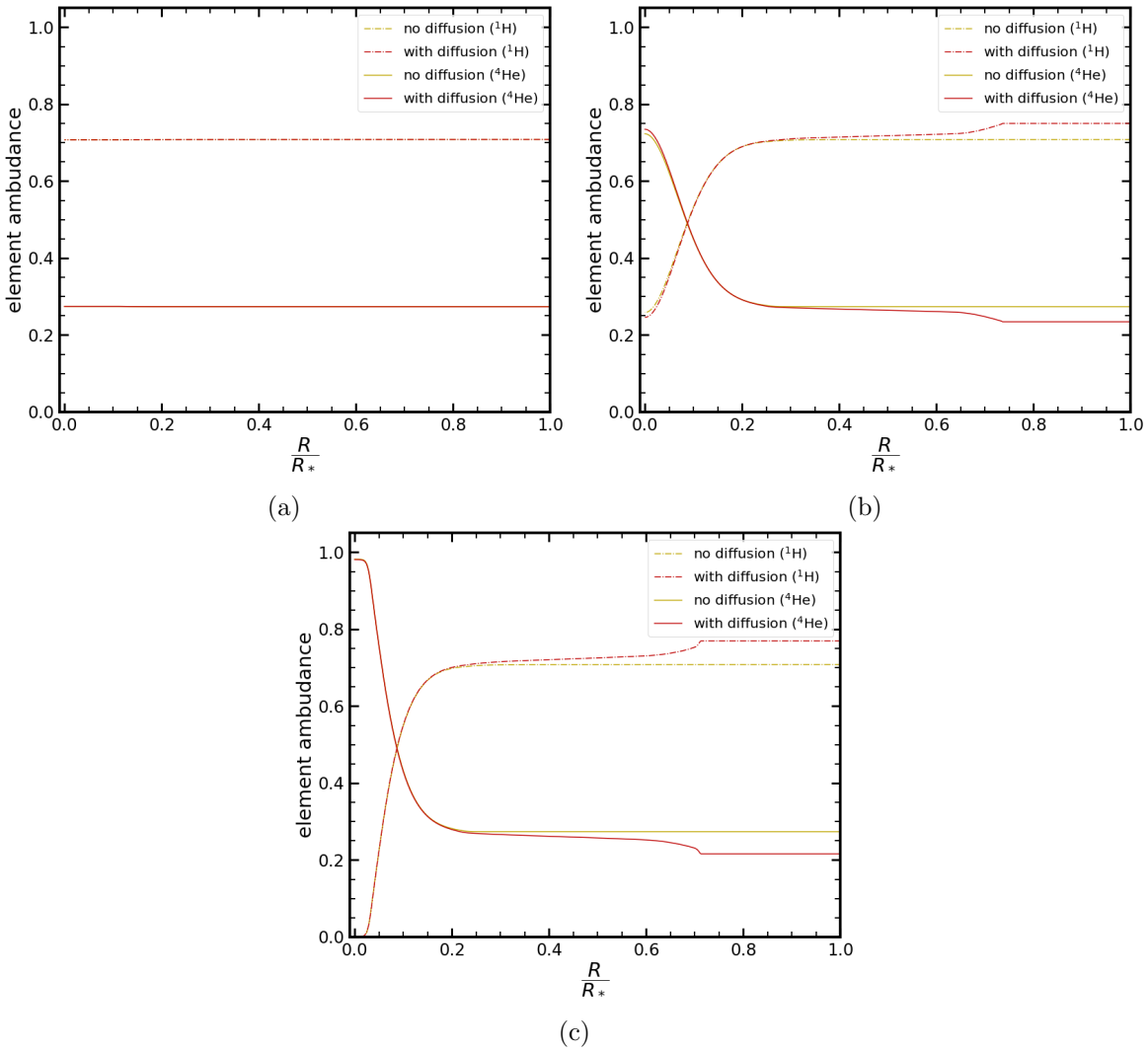

Figure 2.20: Internal profile of H and He abundances with and without diffusion (a) at the beginning of the MS, (b) at an age of 5 Gyr on the MS, and (c) at the end of the MS.

3 Theoretical Asteroseismology

Asteroseismology is the study of the oscillations of stars, providing information about the internal stellar structure and dynamics. It enables the measurement of accurate and precise stellar parameters due to the availability of high-quality data and the mature theory of stellar pulsations.

3.1 Stellar Pulsation Equations

The stellar material can be treated as a fluid and described using the equations of mass conservation,

$$\frac{\partial \rho}{\partial t} = -\nabla(\rho \mathbf{v}), \tag{3.1}$$

momentum conservation,

$$\rho \frac{\partial \mathbf{v}}{\partial t} + \rho(\mathbf{v}\nabla)\mathbf{v} = -\nabla P + \rho \nabla \Phi, \tag{3.2}$$

and Poisson's equation,

$$\nabla^2 \Phi = -4\pi G \rho, \tag{3.3}$$

where t is time, $\mathbf{v} = \dfrac{\partial \boldsymbol{\xi}}{\partial t}$ is the velocity vector, $\boldsymbol{\xi}$ is the displacement vector, and Φ is the gravitational potential.

Take adiabatic fluctuations in a sphere, with a small period of oscillation so as to prevent energy transfer with the surroundings, and the adiabatic coefficient $\Gamma_1 = \frac{\rho}{P}\frac{\delta P}{\delta \rho}$. Then take a linear perturbation in the variables:

$$\begin{aligned} \rho &= \rho_0 + \rho', \\ P &= P_0 + P', \\ \mathbf{v} &= \mathbf{v'}, \\ \Phi &= \Phi_0 + \Phi', \end{aligned} \tag{3.4}$$

where the terms ρ_0, P_0 and Φ_0 are the equilibrium quantities, and ρ', P', Φ', $\mathbf{v'}$ and $\boldsymbol{\xi'}$ are the perturbation terms. Now replacing the set of eqs. 3.4 in equations 3.1 to 3.3, making use of the Γ_1 equation, and neglecting terms of second and higher order, we obtain the perturbation equations:

$$\frac{\partial \rho'}{\partial t} = -\nabla(\rho_0 \frac{\partial \boldsymbol{\xi}}{\partial t}), \tag{3.5}$$

$$\rho_0 \frac{\partial^2 \boldsymbol{\xi}}{\partial^2 t} = -\nabla P' + \rho_0 \nabla \Phi' + \rho' \nabla \phi_0, \tag{3.6}$$

$$\nabla^2 \Phi' = -4\pi G \rho', \tag{3.7}$$

$$P' + \boldsymbol{\xi} \nabla P_0 = \frac{\Gamma_{1,0} P_0}{\rho_0} \left(\rho' + \boldsymbol{\xi} \nabla \rho_0\right). \tag{3.8}$$

The problem can be treated in spherical coordinates (r, θ, φ), whereby the variables will have a dependence on r, θ, φ and t. This way, it is possible to show, by substitution, that equations 3.5 to 3.8 have solutions

$$f'(r, \theta, \varphi, t) = \Re\{f'(r) Y_\ell^m(\theta, \varphi) e^{-i\omega t}\}, \tag{3.9}$$

and

$$\boldsymbol{\xi}(r, \theta, \varphi, t) = \Re\left\{\left[\xi_r(r) Y_\ell^m(\theta, \varphi); \xi_h(r) \frac{\partial Y_\ell^m(\theta, \varphi)}{\partial \theta}; \frac{\xi_h(r)}{\sin(\theta)} \frac{\partial Y_\ell^m(\theta, \varphi)}{\partial \varphi}\right] e^{-i\omega t}\right\}, \tag{3.10}$$

where f may represent ρ, P and Φ, and the terms ξ_r and ξ_h are, respectively, the depth-dependent amplitudes of the radial and horizontal components of the displacement. Y_ℓ^m are spherical harmonics, and ω is the angular oscillation frequency which is real in order to be consistent with a fully reflective boundary.

Spherical harmonics exhibit a dependence on 2 quantum numbers: the angular degree ℓ, which is a positive integer, corresponds to the number of surface nodes of the perturbation; and the azimuthal order m, which takes integer values between $-\ell$ and ℓ, corresponding to the subset of surface nodes which cross the equator. Figure 3.1 illustrates some of the spherical harmonics for different values of ℓ and m.

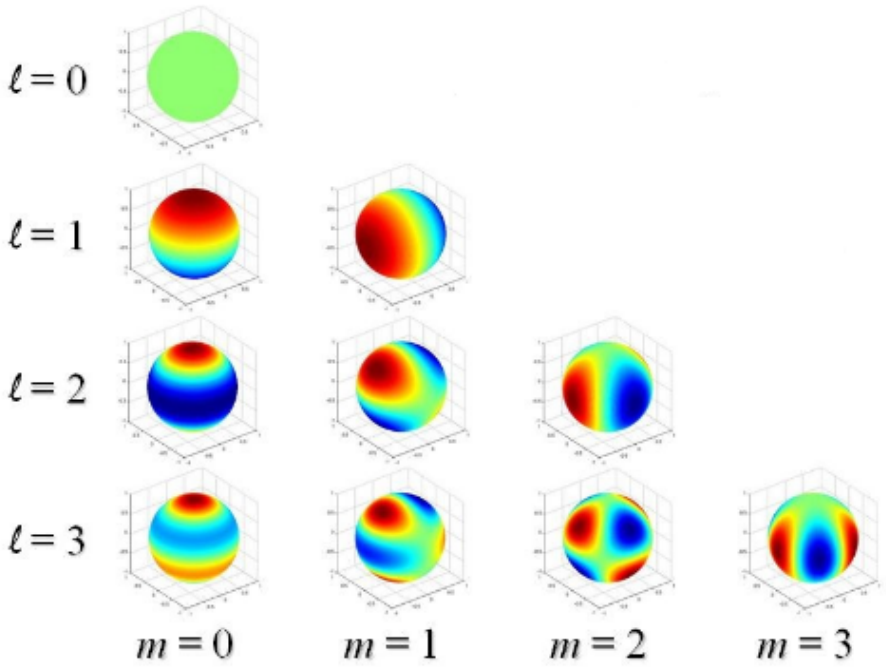

Figure 3.1: Examples of spherical harmonics for $\ell = 0$ to $\ell = 3$ and all allowed non-negative values of m. Red and blue regions show the perturbation at opposite phases [3].

Taking the perturbation equations and making use of the property $\nabla_h^2 Y_\ell^m = -\frac{\ell(\ell+1)}{r^2} Y_\ell^m \equiv -\kappa_h^2 Y_\ell^m$, we can obtain a system of differential equations:

$$\frac{c_0^2}{r^2}\frac{d}{dr}(r^2\xi_r) - g_0\xi_r - \left(\frac{S_\ell^2}{\omega^2} - 1\right)\frac{P'}{\rho_0} = \frac{S_\ell^2}{\omega^2}\Phi', \tag{3.11}$$

$$\frac{dP'}{dr} + \frac{g_0}{c_0^2}P' - \rho_0(\omega^2 - N^2)\xi_r = -\rho_0\frac{d\Phi'}{dr}, \tag{3.12}$$

$$\frac{1}{r^2}\frac{d}{dr}\left(r^2\frac{d\Phi'}{dr}\right) - \frac{\ell(\ell+1)}{r^2}\Phi' = 4\pi G\left(\frac{P'}{c_0^2} + \frac{\rho_0 N^2}{g_0}\xi_r\right). \tag{3.13}$$

We define two characteristic frequencies: the Lamb frequency, S_ℓ, and the buoyancy frequency, N, which are given by

$$S_\ell^2 = \frac{\ell(\ell+1)c_0^2}{r^2}, \quad N^2 = g_0\left[\frac{1}{\Gamma_{1,0}}\frac{d\ln P_0}{dr} - \frac{d\ln\rho_0}{dr}\right], \tag{3.14}$$

where c_0 is the sound speed and g_0 is the gravity at equilibrium. We can also introduce a third characteristic frequency, i.e., the critical frequency ω_c:

$$\omega_c^2 = \frac{c_0^2}{4H^2}\left(1 - 2\frac{dH}{dr}\right), \tag{3.15}$$

where $H = \rho\left(\frac{d\rho}{dr}\right)^{-1}$.

In Fig. 3.2 we can see these three frequencies for a model of the Sun and a model of a star in the red-giant phase. The buoyancy frequency is only defined for $N^2 > 0$, which corresponds to radiative regions (see eq. 2.12). For the red-giant model, the convective region extends deeper into the interior of the star. The Lamb frequency has a similar behavior in both models.

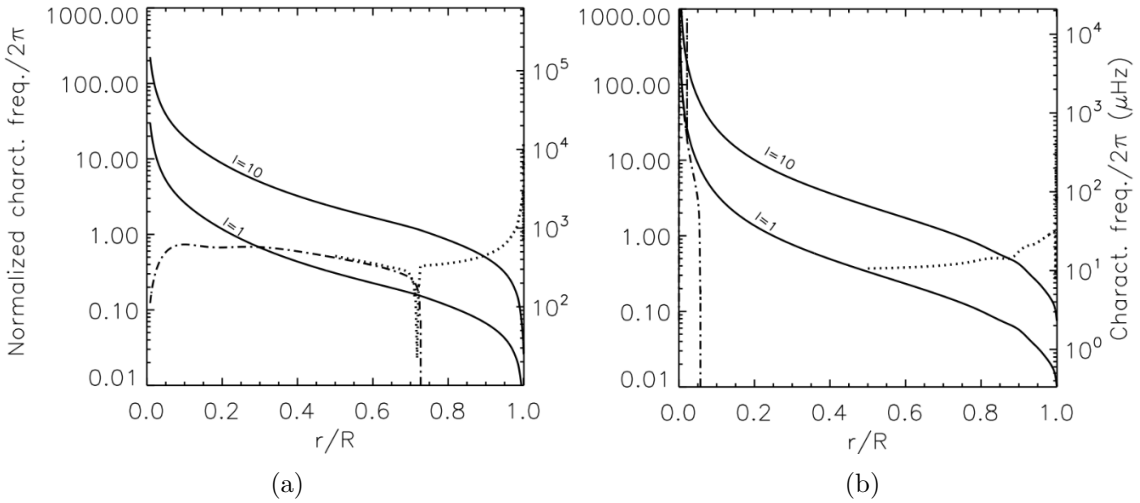

(a) (b)

Figure 3.2: Lamb frequency, S_ℓ (continuous line), for $\ell = 1$ and $\ell = 10$, the buoyancy frequency, N (dashed-dotted line), and the critical frequency, ω_c (dotted line). Panel (a) is for a model of the Sun and (b) is for an RG star [3].

3.2 Oscillation Modes

The system of differential equations (see eqs. 3.11 - 3.13) can be solved numerically if appropriate boundary conditions are defined. Solutions only exist for discrete values of the eigenfrequencies ω, which is associated to an integer n (the radial order), corresponding to the number of nodes of the perturbation along the radial direction. The solution is then characterized by three quantum numbers, i.e., $\omega = \omega(n, \ell, m)$. The absence of physical agents capable of breaking spherical symmetry (such as rotation) will, however, lead to a degeneracy in m. In such case, one simply has $\omega = \omega(n, \ell)$.

There are two forces acting inside the star, the pressure force and gravity, and it is possible to find solutions associated with either force. We can have acoustic waves (pressure or p-modes), which are generated by radial or non-radial perturbations in the pressure gradient. These modes are associated with a positive n and present an increase in the frequency with n and ℓ.

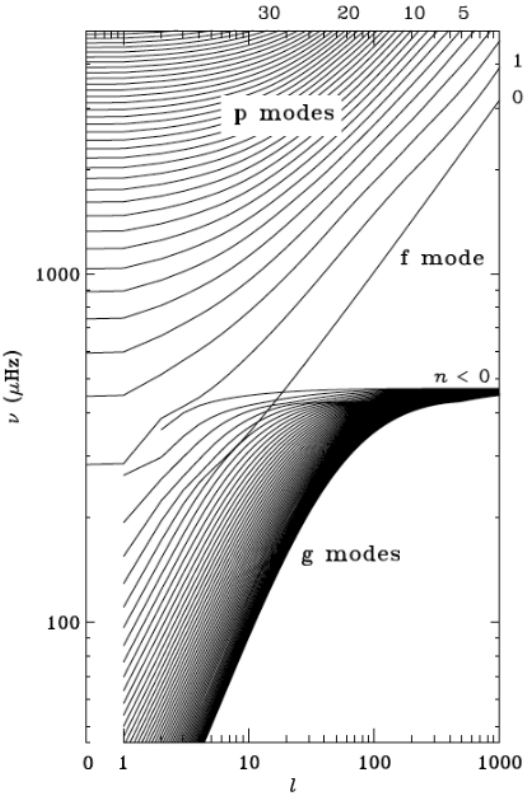

Figure 3.3: p- and g-modes for a model of the Sun. Modes connected by a continuous line have the same discrete value of the radial order n. Figure adapted from [21].

Another solution are gravity waves (gravity or g-modes), which only propagate in radiative regions, being generated by a slow displacement of an element of the fluid, whose pressure is kept in equilibrium with the surroundings. Buoyancy will restore the fluid toward the equilibrium position if the density of the element is larger than the surrounding medium, leading to an oscillatory motion. The movement of the element of fluid can not be strictly vertical, and present horizontal component, implying that these oscillations are non-radial, i.e., with $\ell > 0$. These modes are associated with negative values of n and present an increase in frequency with a decrease in $|n|$ and an increase in ℓ.

One last solution are surface waves (f-modes). These modes appear when considering an incompressible medium near the surface. This solution is identified as a gravity wave and propagates across the surface like waves in a deep ocean. These modes are intermediate between g-modes and p-modes, being identified by a radial order $n = 0$.

Figure 3.3 shows the computed solution for a model of the Sun, displaying the three types of modes presented before and showing how the frequency varies with radial order, n, and mode degree, ℓ.

3.3 Scaling Relations

We can extract two global parameters from an asteroseismic analysis that can be related to the stellar parameters. One of them is the frequency of maximum power, $\nu_{\rm max}$, which is related to the stellar surface gravity, g, and the effective temperature, $T_{\rm eff}$, through the scaling relation

$$\nu_{\rm max} \propto \frac{g}{\sqrt{T_{\rm eff}}} \propto \frac{M_*}{R_*^2\sqrt{T_{\rm eff}}}. \tag{3.16}$$

The other is the large frequency separation, $\Delta\nu$, which is the separation between modes of the same degree ℓ and consecutive radial order n. This can be related to the mean density of the star, $\bar{\rho}$, by

$$\Delta\nu = \nu_{n\ell} - \nu_{n-1\ell} \propto \sqrt{\bar{\rho}} \propto \sqrt{\frac{M_*}{R_*^3}}. \tag{3.17}$$

These two parameters can be combined to obtain expressions to estimate the stellar mass and radius:

$$\frac{R_*}{\rm R_\odot} \approx \left(\frac{\nu_{\rm max}}{\nu_{\rm max,\odot}}\right)\left(\frac{\Delta\nu}{\Delta\nu_\odot}\right)^{-2}\left(\frac{T_{\rm eff}}{T_{\rm eff,\odot}}\right)^{1/2}, \tag{3.18}$$

$$\frac{M_*}{\rm M_\odot} \approx \left(\frac{\nu_{\rm max}}{\nu_{\rm max,\odot}}\right)^{3}\left(\frac{\Delta\nu}{\Delta\nu_\odot}\right)^{-4}\left(\frac{T_{\rm eff}}{T_{\rm eff,\odot}}\right)^{3/2}. \tag{3.19}$$

We can see the power density spectrum for observations of the Sun in Fig. 3.4, showing the individual frequencies and the two global parameters described above. In this figure, we also see a third parameter, i.e., the small frequency separation, which we will not discuss.

These are the parameters related to p-modes that are observed in the type of stars studied herein. However, g-modes can be important for post-MS evolution phases, during which they couple with p-modes giving rise to mixed modes. Mixed modes are non-radial ($\ell > 0$).

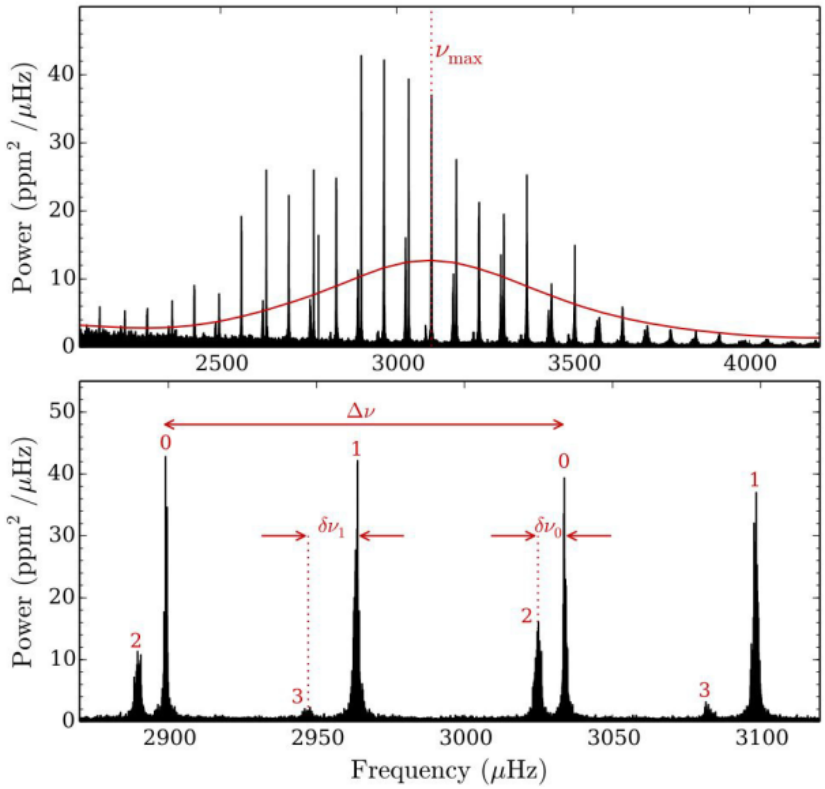

Figure 3.4: Power density spectrum of the Sun. The red line on the top panel shows a smoothing of the spectrum. The bottom panel shows a close-up of the large and small frequency separations [3].

4 MESA - Modules for Experiments in Stellar Astrophysics

MESA is an open source, robust and efficient code containing vast libraries for applications in computational stellar astrophysics constructed in FORTRAN 95. It combines numerical and physical tools for simulation of different stellar evolution scenarios, providing information on equations of state, opacity, nuclear reactions, element diffusion, atmosphere conditions and more. MESA uses different methods to solve diverse systems of ordinary differential equations, like the linearly implicit Runge-Kutta method, with second-, third-, or fourth-order, and the two implicit extrapolation integrators, that can use a midpoint or an Euler method, and also presenting the Newton-Raphson solver to find non-linear roots in multidimensional systems [6].

MESA works with the microphysics and macrophysics of the star, having different modules which work with the relevant constants for stellar physics (in cgs units). For the equations of state, it works primarily with density, ρ, and temperature, T, which are natural variables for Helmholtz free energy. However, some calculations are performed with pressure, P, and T, for Gibbs free energy. For opacity it combines the radiative opacity with the electron conduction opacity, including the molecular grains effect in radiative opacity. Also, in cases where ρ and T present degeneracy, MESA uses the electron conduction opacity. For thermonuclear reactions, it presents different rates for elements up to nickel, and also includes the weak reactions required for the hydrogen burning, as well as neutron-proton conversion and electron and neutron capture[6]. Furthermore, it can calculate the energy loss from neutrino production and also implement nuclear reaction networks [22].

For macrophysics, it uses the mixing length theory (MLT) of convection, computing the temperature gradient, ∇_T, and the convective luminosity, $L_{\rm conv}$. It calculates the diffusion coefficient and can include overshoot. This module treats a convective element as a diffusion process, calculating the diffusion coefficient. Also, it can be set to include overshoot for the upper and lower boundaries of the convective regions. For the stellar atmosphere, it presents different models which use mass, M_*, radius, R_*, and luminosity, L_*, to obtain the superficial pressure, $P_{\rm s}$, superficial temperature, $T_{\rm s}$, and their partial derivatives [6]. Finally, MESA can calculate particle diffusion and gravitational settling by solving Burger's equation and also compute the material transport using a semi-implicit method of finite difference [23, 24].

To run MESA we need to define the initial parameters such as the mass, M_*, initial metallicity, Z, abundance of hydrogen, X, and helium, Y, the mixing-length parameter, $\alpha_{\rm MLT}$, and others that might be necessary. It is also required that we introduce constraints on the step in time to promote the convergence of models along the evolution of the star, but also stop conditions that can be defined based on variations of different parameters such as time, density, element abundance, and others. We

can also define the different physical mechanisms such as diffusion, atmosphere, nuclear reactions, convection mechanism, and more. These inputs will affect the stellar evolution, as well as the parameters obtained during the creation of the models in MESA [4]. Table 4.1 shows some of the main criteria for the selection of the time step and stopping condition used at different stages of evolution for the demonstration in Section 2.

Table 4.1: Criteria used for the selection of the time steps and stopping conditions in the production of models in Section 2.

	Criteria	
Stage	Time step	Stopping condition
Pre-MS	———	$\frac{L_{\rm nuc}}{L_*} = 0.99$
MS	$\Delta \log(X_{\rm center}) \lesssim 0.01$	$X_{\rm center} \lesssim 1 \times 10^{-4}$
SG	$\Delta t \lesssim 10^7$ yr	$\log(\rho_{\rm c}) = 4.5$
RG	———	$M_{\rm core} = 0.45$ M$_\odot$

In previous models, different stopping conditions were used between different evolution phases. The main condition used to define the end of the MS was that the hydrogen abundance at the center reaches a value close to zero. However, for stars that do not have a convective core, this condition is satisfied before the star reaches the SG phase. Consequently, these stars end up having a longer life time than expected in the SG phase due to the fact that the hydrogen in the core has not been completely exhausted yet. One additional condition which we introduced in all computed models was that the age must be less than the age of the Universe ($\sim$ 14Gyr).

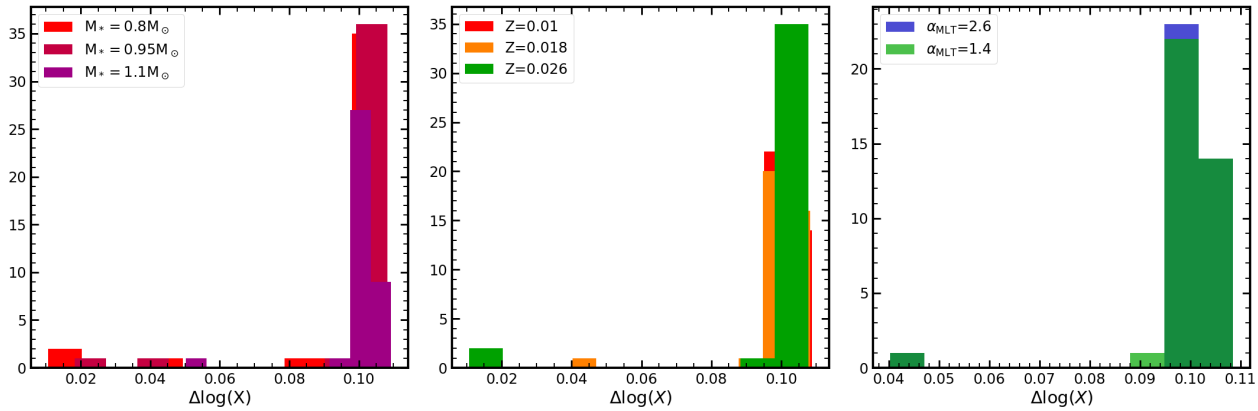

(a) (b) (c)

Figure 4.1: Histograms of the time step between models during the MS, where (a) is for different masses, (b) for different metallicities, and (c) for different $\alpha_{\rm MLT}$.

In the construction of a model grid, it is necessary to use an appropriate time step to obtain convergence of the models, and a reasonable number of them. When we run MESA we choose that it keeps one model every 10 times steps to avoid an excess of models that could lead to memory problems. As we can see in the histograms of Fig. 4.1, most of the time steps obtained are approximately 10

times larger than the step imposed (see Table 4.1), as a result of what was mentioned above. Those with smaller values are due to other conditions that may be necessary to stabilize the star, e.g., in the transition between the pre-MS and the MS.

Now our goal is to model the Sun. For this we will build two grids. In one we will only vary mass and metallicity, whereas in the other we will take into account the effects of $\alpha_{\rm MLT}$ and diffusion. In Table 4.2 the parameters used in each grid are shown.

Table 4.2: Parameters used when building the two grids.

	M ($M_\odot$)	ΔM ($M_\odot$)	Z	ΔZ	$\alpha_{\rm MLT}$	$\Delta\alpha_{\rm MLT}$	Diffusion
Grid 1	$[0.9 - 1.1]$	0.05	$[0.01 - 0.022]$	0.002	2.0	———	OFF
Grid 2	$[0.9 - 1.1]$	0.05	$[0.01 - 0.028]$	0.002	$[1.6 - 2.2]$	0.2	ON

The grids are shown in Figs. 4.2 and 4.3. Figure 4.2 shows the two grids, with models in Grid 2 having $\alpha_{\rm MLT} = 2.0$. Figure 4.3 shows all models of Grid 2. In both figures, the location of the Sun is represented by a star symbol.

To proceed with the modeling of the Sun, we need to compute the frequencies of oscillation for each model. For this we will use another code, called GYRE, to solve the stellar pulsation equation.

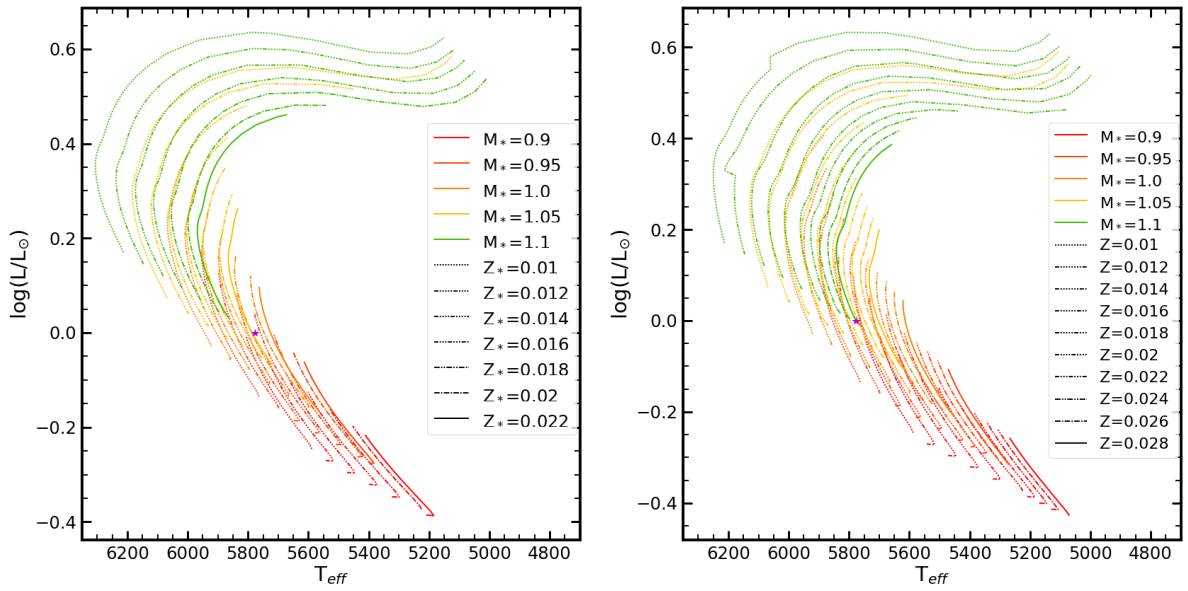

(a) (b)

Figure 4.2: Representation in the HR diagram of (a) Grid 1 and (b) Grid 2 (with $\alpha_{\rm MLT} = 2.0$, as in Grid 1).

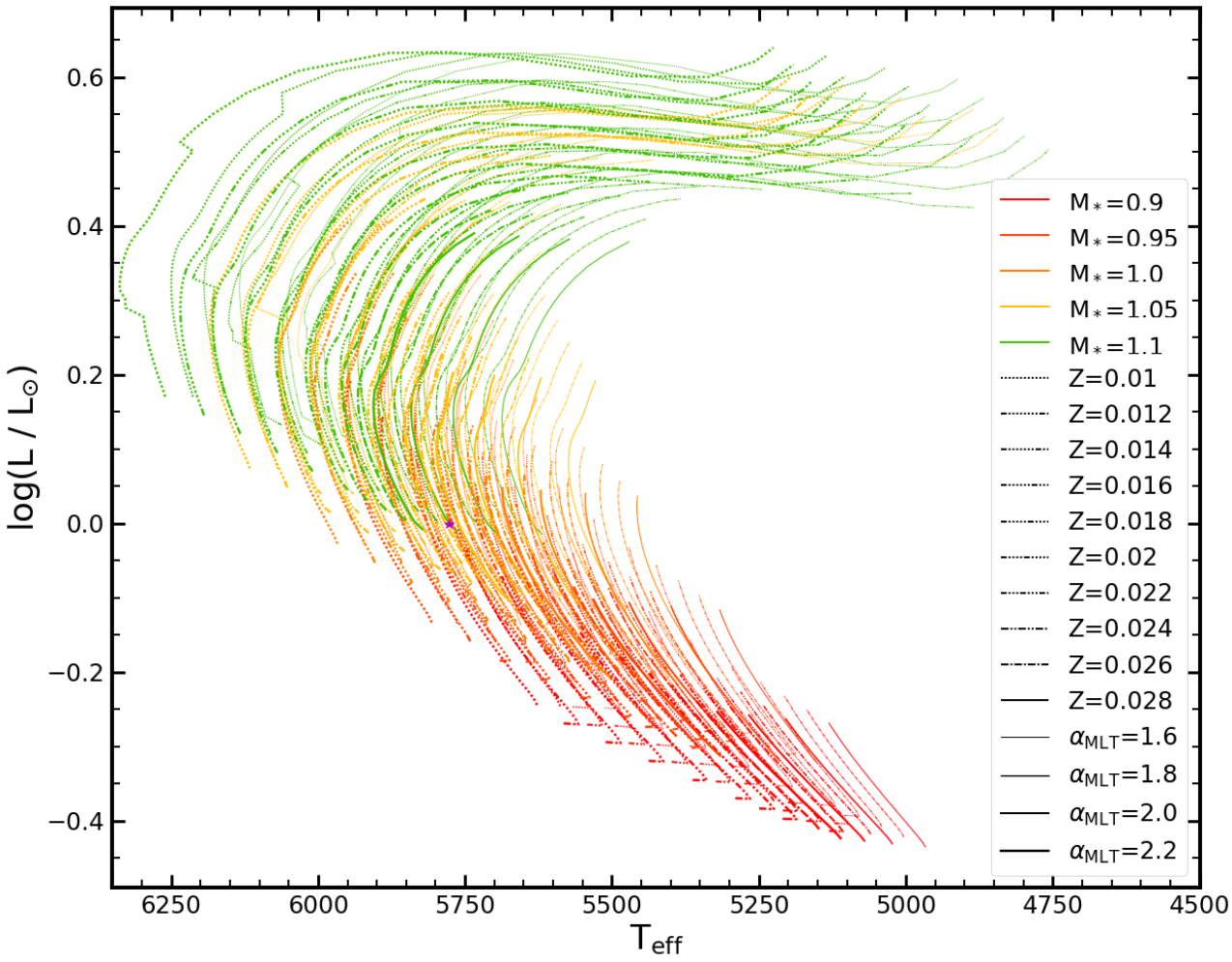

Figure 4.3: HR diagram for the complete Grid 2.

5 GYRE

GYRE is an oscillation code built in FORTRAN 2008 with a modular architecture that allows dealing with complicated problems. It uses the Magnus Multiple-Shooting (MMS) scheme to calculate the eigenfrequencies and the eigenfunctions of stellar models. GYRE will solve numerically the linearized stellar pulsation equations (eqs. 3.11, 3.12, and 3.13), and is prepared to deal with the adiabatic and the non-adiabatic pulsations problem [5].

GYRE starts by reading the files containing the information about the stellar models. It creates a grid for the multiple-shooting in order to reconstruct the eigenfunctions. Then it builds a matrix with the pulsation equations, S, and determines the eigenfrequencies, which are the roots of $D(\omega) = \det[S(\omega)]$. From the obtained roots, and using the Magnus' integrator, it reconstructs the corresponding eigenfuctions for the multiple-shooting grid, and reevaluates them in a separately reconstructed grid [5].

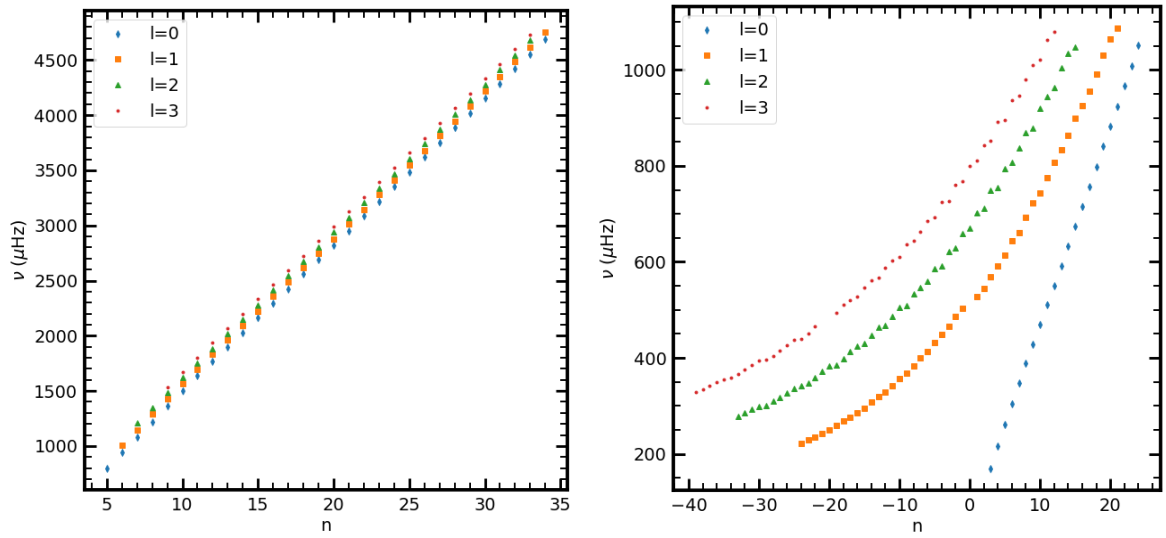

Figure 5.1: Theoretical frequencies as a function of the radial order for a model with $M_* = 1.1\mathrm{M}_\odot$ and $Z = 0.01$ at two different evolutionary stages. (a) Theoretical frequencies at the beginning of the MS and (b) during the SG phase.

For the grids previously built with MESA, we obtained the theoretical oscillation frequencies of each stellar model with the respective radial orders, n, and angular degrees, ℓ. We now have to look at the theoretical frequencies obtained for Grid 1. By observing the models in the MS and SG phase, shown in Fig 5.1, we see that the frequencies increase, in both cases, with radial order, n, and with angular degree, ℓ. In the SG phase, we notice that non-radial modes ($\ell > 0$) do not follow a linear distribution like in the MS. This occurs due to the emergence of mixed modes, whereby coupling between g-modes and p-modes starts to appear. Radial modes ($\ell = 0$) are pure p-modes, as we have seen before.

Figure 5.2 shows the evolution of mode frequencies along the evolutionary track of a star with $M_* = 1.1\mathrm{M}_\odot$ and $Z = 0.01$. Mode frequencies tend to decrease over time, with the right panel ($\ell = 1$) exhibiting mixed modes as the star enters the SG phase. For $\ell = 2$ and $\ell = 3$ modes, we chose not to show their evolution since it is identical to that of $\ell = 1$ modes.

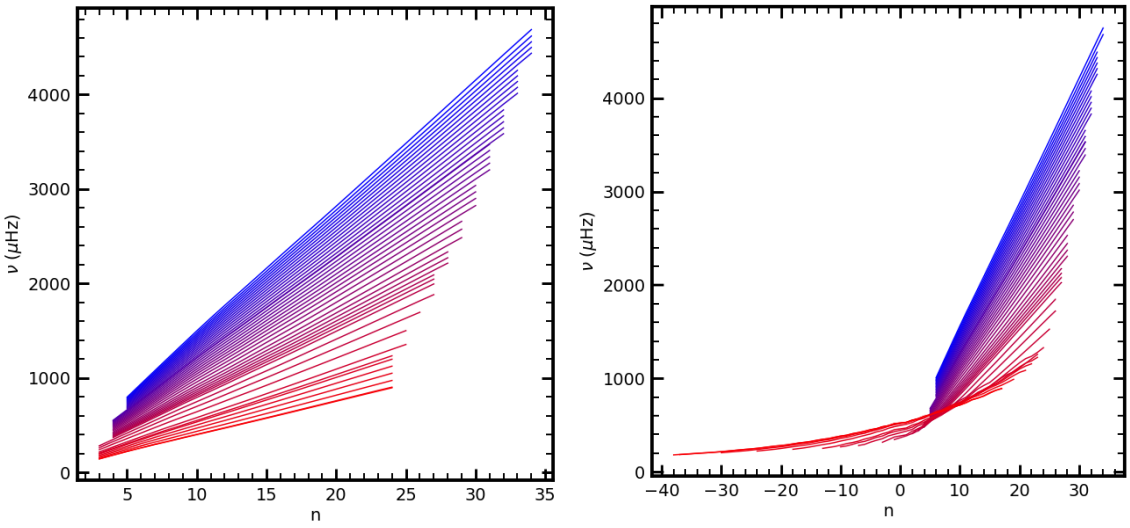

Figure 5.2: Evolution of theoretical frequencies during the lifetime of a star with $M_* = 1.1\mathrm{M}_\odot$ and $Z = 0.01$. The temporal evolution is represented by a color gradient going from blue (beginning of the MS) to red (end of the SG phase). (a) Evolution for $l = 0$ modes and (b) $\ell = 1$ modes.

We can estimate the large frequency separation, $\Delta\nu$, by performing a linear fit to the $l = 0$ frequencies. In Fig. 5.3 we see the evolution of $\Delta\nu$ with stellar age for a star with $M_* = 0.1\mathrm{M}_\odot$ and $Z = 0.01$, observing that this parameter tends to decrease with age, which can be explained by the decreasing average density as the stellar radius grows with time.

We build a contour map of $\Delta\nu$ (Grid 1) in Fig. 5.4. Keeping metallicity constant, we see not only how $\Delta\nu$ decreases with stellar age but also with the mass of the star. This happens because, with increasing stellar mass, the radius also increases, thus reducing $\bar{\rho}$, since R_* dominates the density calculation.

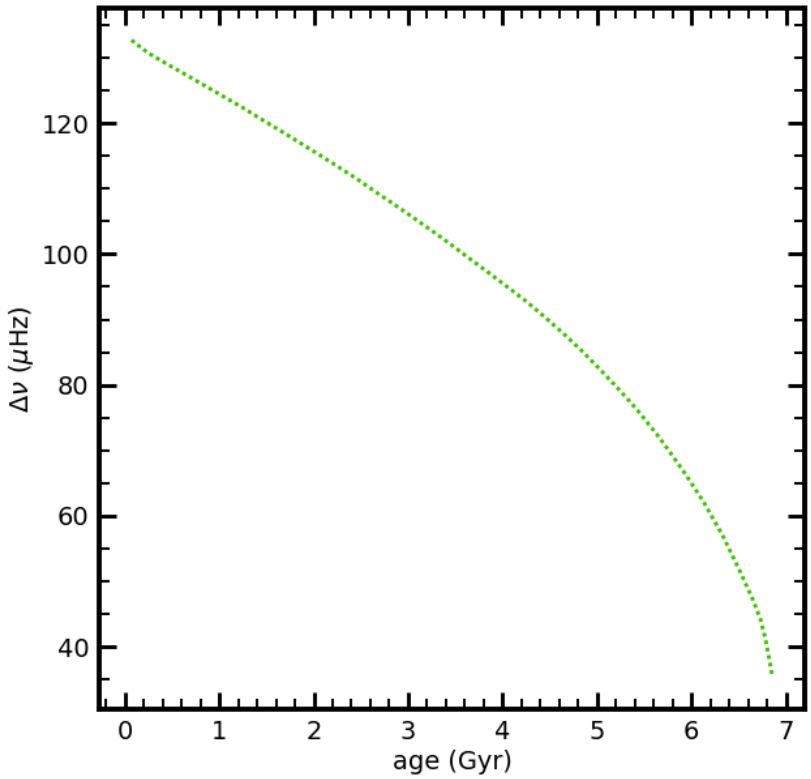

Figure 5.3: Evolution of the large frequency separation, $\Delta\nu$, with stellar age for a star with $M_* = 1.1\mathrm{M}_\odot$ and $Z = 0.01$.

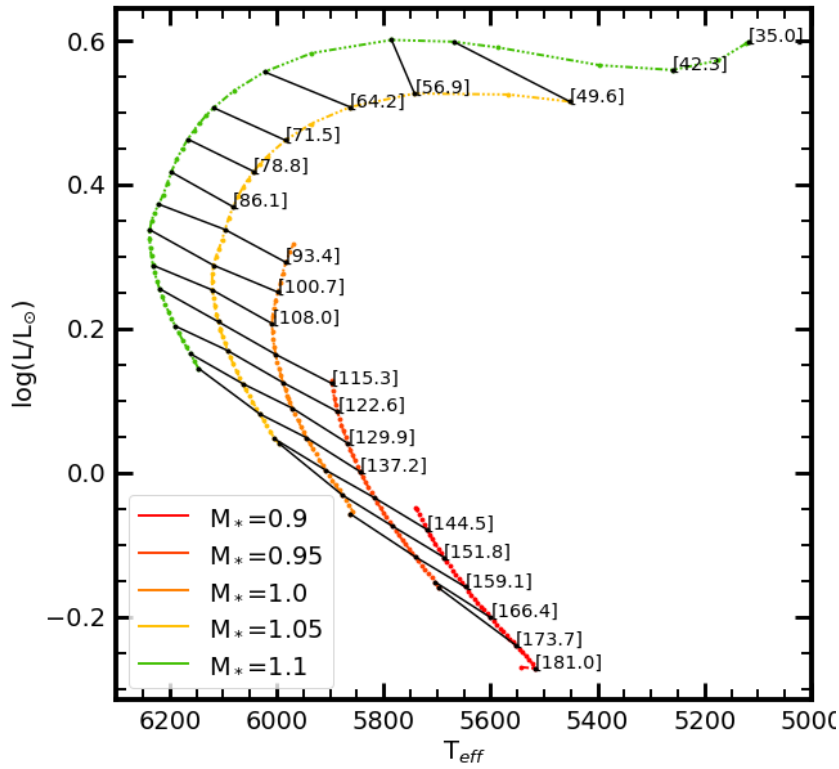

Figure 5.4: Contour map of the large frequency separation for a star with $Z = 0.012$ (Grid 1).

6 AIMS - Asteroseismic Inference on a Massive Scale

AIMS is an optimization code built in Python. It uses Bayesian statistics and a Markov Chain Monte Carlo (MCMC) algorithm to identify a model that matches the input parameters by interpolating the pre-built grid, allowing an efficient search in the space of parameters defined by the grid. For greater efficiency in the use of the MCMC algorithm, AIMS initiates the search of the grid within a set of models with higher posterior probability, which allows it to converge quickly [6, 25, 26].

During the interpolation process, AIMS takes into account the surface correction. This correction is introduced to compensate for shortcomings in the frequency calculations, i.e., the use of an adiabatic approximation and the lack of a description of the interaction between convection and oscillations [27]. The surface correction adopted has been proposed in reference [27], whereby the surface effect is modeled by two terms, $a_{-1} \propto \nu^{-1}/\mathcal{I}$ and $a_3 \propto \nu^3/\mathcal{I}$, where ν is the frequency of an oscillation mode and $\mathcal{I}$ is the corresponding inertia. The frequency correction is then parameterized as:

$$\delta\nu = [a_{-1}(\nu/\nu_{\rm ac})^{-1} + a_3(\nu/\nu_{\rm ac})^3]/\mathcal{I}, \tag{6.1}$$

where $\nu_{\rm ac}$ is the acoustic cutoff frequency.

Now we want to obtain the stellar parameters for the Sun. To do this, we use the two constructed grids presented in Table 4.2 and use as constraints: the observed frequencies, as well as $T_{\rm eff}$ and [Fe/H] (see last row of Table A.1 in the Appendix).

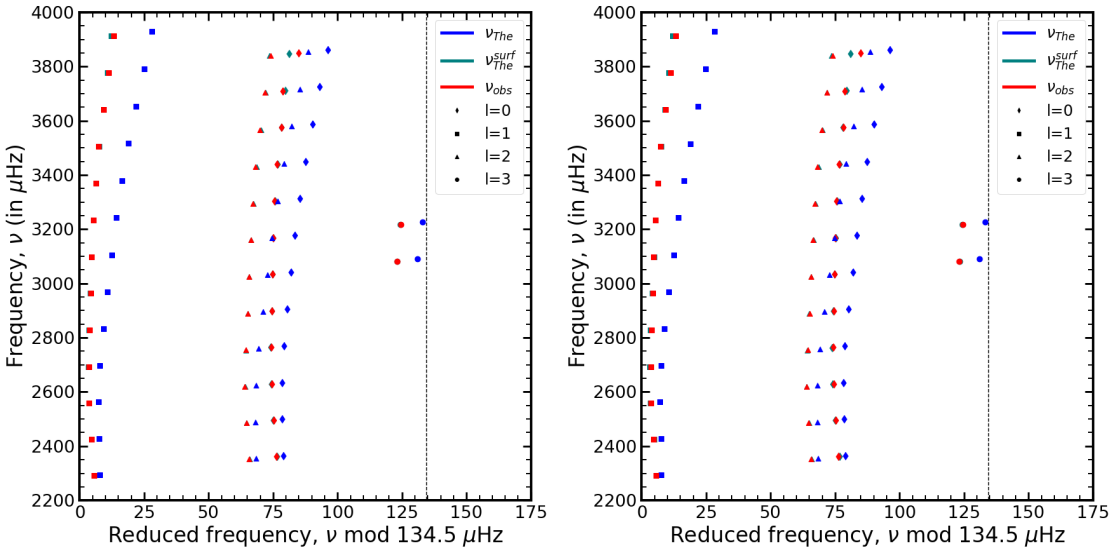

Figure 6.1: Échelle diagrams for the best-fit models returned by AIMS showing the observed frequencies of the Sun and the theoretical frequencies with and without the surface corrections: (a) Grid 1 and (b) Grid 2.

AIMS will do the calculation and provide the requested parameters and corresponding probability distributions, and the échelle diagram [25]. The échelle diagrams (see Fig. 6.1) are constructed after model interpolation and present the observed frequencies and the best-fit model frequencies with and without the surface correction. We see that the discrepancy between the observed and theoretical frequencies without the application of the surface correction is more significant for the higher-frequencies modes because these are more sensitive to stellar atmospheric models.

AIMS produces histograms of the probability distributions for the fitted parameters and also the correlation between each pair of parameters [25]. In Fig. 6.2, the mass probability distribution is shown. Figure 6.3 shows a corner plot for Grid 1, showing the correlation between mass, age, metallicity, and surface parameters.

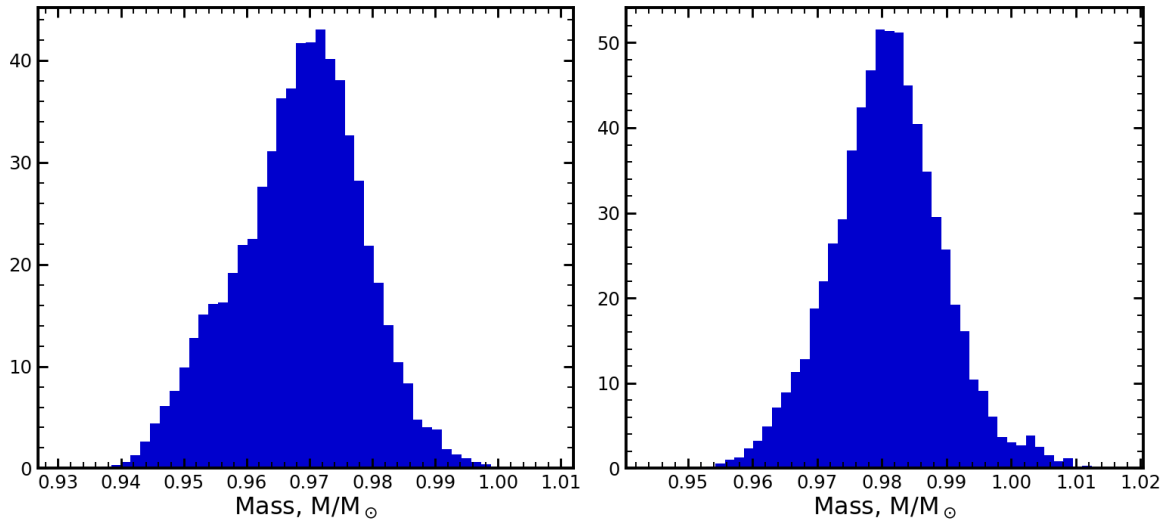

(a) (b)

Figure 6.2: Mass probability distribution for (a) Grid 1 and (b) Grid 2.

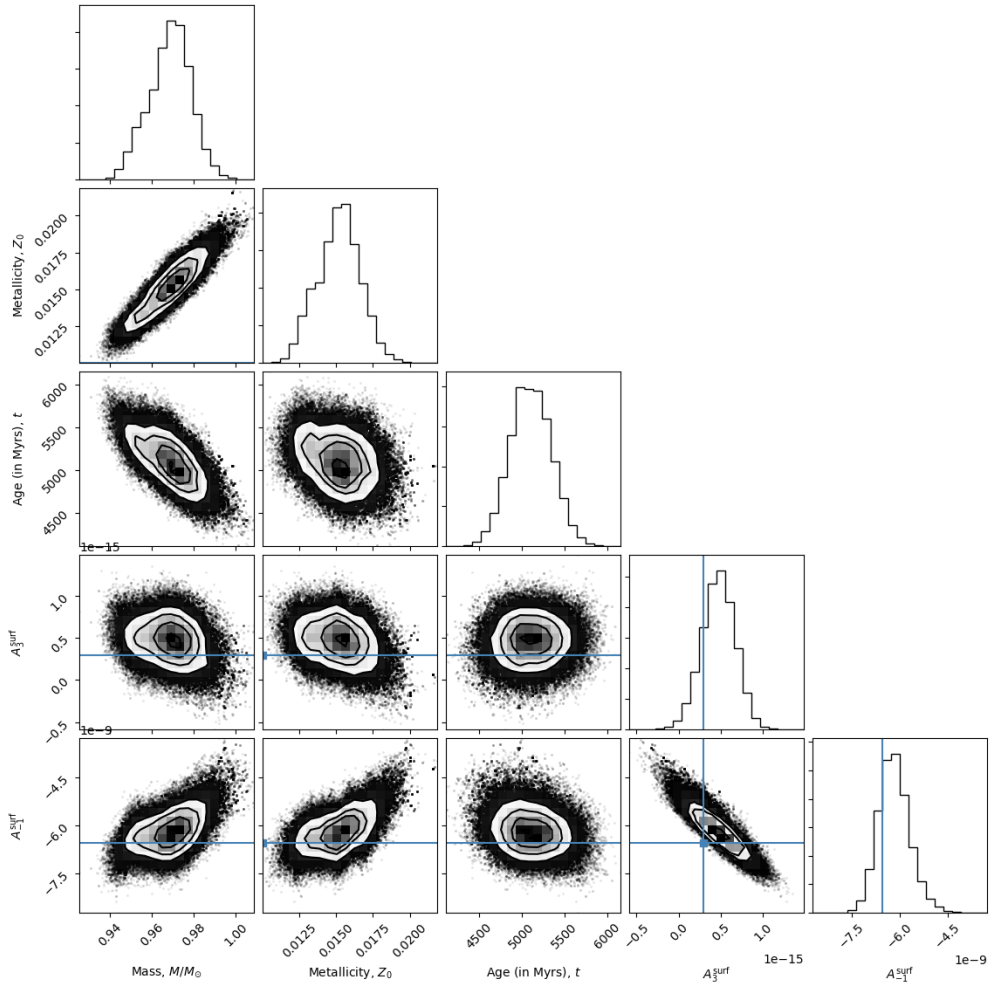

Figure 6.3: Corner plot showing the correlation between different stellar parameters for Grid 1

AIMS provides the values for the different parameters and we have organized them in Table 6.1, with the solar values for comparison. We see that, for Grid 2, the majority of the parameters are closer to the real ones than for Grid 1. This is due to the fact that in the former grid we included diffusion, which constitutes a more accurate representation of the physics for the real Sun. Regarding the surface correction, they significantly deviate from those in [27], likely due to the use of a different set of frequencies as constraints and/or different input physics in the models.

We further compare our results for the Sun with other results obtained by different pipelines [26] (see Table 6.2). We note that the uncertainties returned by our modeling of the Sun are purely statistical (no systematic uncertainties included) and may thus be underestimated. We conclude that our stellar models are capable of satisfactorily reproducing the Sun. We now proceed to study the effects of the helium abundance in stellar models.

Table 6.1: Table with the obtained solar values.

	Sun	Grid 1	Grid 2
$M(\mathrm{M}_\odot)$	1	0.968±0.010	0.981±0.009
$R(\mathrm{R}_\odot)$	1	0.987±0.004	0.992±0.003
$L(\mathrm{L}_\odot)$	1	0.988±0.010	0.977±0.021
T_{eff}(K)	5772	5799±21	5768±30
ρ (g cm^{-3})	1.408	1.419±0.002	1.416±0.002
[Fe/H]	0.0	-0.038±0.044	-0.047±0.034
Age (Myr)	4570 [27]	5106±238	4704±203
Z_{s}	0.0169 [28]	0.0151±0.0014	0.0154±0.0011
Y_{s}	0.248[27]	0.269±0.002	0.244±0.003
$\mathrm{a}_3^{\mathrm{surf}}$ (μHz)	-2.25×10^{-7}[27]	(4.69±1.97)×10^{-16}	(5.10±2.10)×10^{-16}
$\mathrm{a}_{-1}^{\mathrm{surf}}$ (μHz)	1.73×10^{-9}[27]	(-6.17±0.49)×10^{-9}	(-5.56±0.78)×10^{-9}
α_{MLT}	1.83[29]	2.0	2.10±0.06
$\Delta\nu$ (μHz)	135.1[28]	136.94±0.03	136.85±0.06
ν_{max} (μHz)	3104.0[28]	3060.7±12.1	3083.6±9.2

Table 6.2: Parameter values obtained by different pipelines [26], plus the solar values and the values obtained using Grid 2.

	Mass($\mathrm{M}_\odot$)	Radius ($\mathrm{R}_\odot$)	Age (Myr)	Luminosity ($\mathrm{L}_\odot$)	Density (g cm^{-3})	Y_{s}
Sun	1	1	4570	1	1.408	0.248
AIMS (Grid 2)	0.981± 0.009	0.992±0.003	4704±203	0.977±0.021	1.416±0.002	0.242±0.003
AIMS [26]	0.979±0.013	0.992±0.005	4840±367	1.060±0.048	1.413±0.004	—
ASTFIT	0.986±0.027	0.994±0.008	4686±393	0.972±0.052	1.411±0.003	0.249±0.009
BASTA	$0.978^{+0.039}_{-0.030}$	$0.993^{+0.012}_{-0.012}$	4852^{+1181}_{-1069}	$0.976^{+0.054}_{-0.052}$	$1.411^{+0.021}_{-0.022}$	$0.247^{+0.012}_{-0.010}$
C2kSMO	1.021±0.003	1.006±0.010	4331±85	1.084±0.048	1.412±0.048	0.245±0.003
GOE	0.997±0.006	0.995±0.018	4859±128	0.947±0.041	1.412±0.002	0.234±0.009
V&A	0.927±0.030	0.973±0.015	4621±200	0.937	1.418±0.006	0.27
YMCM	$1.037^{+0.031}_{-0.047}$	$1.012^{+0.005}_{-0.005}$	5297^{+350}_{-350}	$1.008^{+0.043}_{-0.022}$	$1.406^{+0.001}_{-0.001}$	$0.248^{+0.010}_{-0.010}$

7 Helium Abundance

In this chapter, we explore the treatment of the initial helium abundance on the derived stellar parameters. Helium abundances for solar-type stars are not measurable using spectroscopy. This is because the surface temperature of these stars does not reach 20,000K, meaning that the spectral lines associated with this element are not detected, thus preventing the measurement of the helium abundance. Therefore, to set the helium abundances for these stars, we use the helium enrichment law (eq. 2.19), which depends on the helium enrichment ratio, $\left(\frac{\Delta Y}{\Delta Z}\right)$, obtainable through observations. Nevertheless, there is no consensus regarding the value of this ratio, since different observations have led to different values for this parameter.

To tackle this problem, we employ two stellar grids (described in Sect. 7.1), with different values of $\frac{\Delta Y}{\Delta Z}$, to assess how this parameter affects the estimation of stellar parameters.

7.1 Stellar Grids

We constructed two stellar grids using MESA version 9793 (namely, A and B), varying only in the treatment of the initial helium mass fraction (Y). The evolutionary tracks were evolved from the pre-main sequence and stellar models were stored starting from the zero-age main sequence (ZAMS), which we defined as the region along the evolutionary tracks where the model nuclear luminosity is approximately 99% of its total luminosity. Two termination criteria were specified during the grid construction, i.e., evolutionary tracks were terminated when: (i) models reach a stellar age of 16 Gyr, explaining why the evolutionary tracks with stellar masses of 0.8 $M_\odot$ and 0.9 $M_\odot$ shown in Fig. 7.1 do not reach the subgiant stage; (ii) they reach a region along the evolutionary track where $\log(\rho_c) = 4.5$.

The general input physics used in both grids include nuclear reaction rates obtained from JINA REACLIB version 2.2 [15], with specific rates for $^{12}C(\alpha,\gamma)^{16}O$ and $^{14}N(p,\gamma)^{15}O$ described in [31] and [32], respectively. At high temperatures, OPAL tables [33] were used for the opacities, while tables from [34] were used at lower temperatures. Both grids used the 2005 updated version of the OPAL equation of state [35]. The surface boundary of stellar models was described using the standard Gray–Eddington atmosphere. It should be noted that both stellar grids used surface chemical abundances as in [36], with $Z_\odot = 0.0169$.

Note that both grids take into consideration different mixing processes (atomic diffusion and overshooting; see section 2), which are expected to depend on the stellar mass and core properties of each star. For stars above 1.2 $M_\odot$, these grids were built without considering diffusion, due to its extreme efficiency in the transport of chemical elements, which usually leads to the depletion of heavy elements at the stellar surface. For models with M_* in the interval $[1.2, 1.6]$ $_\odot$, we include convective

core overshoot by adopting the exponential diffusive overshoot procedure implemented in MESA [37]:

$$Q_{\rm c} = Q_0 \exp(\frac{-2d}{fH_P}), \tag{7.1}$$

where $Q_{\rm c}$ is the diffusion coefficient in the overshoot region, Q_0 is the diffusion in the convective unstable region near the convective boundary determined using the mixing length theory (MLT), d is the distance from the edge of the convective zone, and f is the overshoot parameter.

The input parameters used to build both grids are similar, as shown in Table 7.1. The only difference resides in the value of $\frac{\Delta Y}{\Delta Z}$, which takes the values 1.4 and 2.0 for Grids A and B, respectively. Table 7.2 also shows the range of values used for the different input parameters, namely, mass (M_*), metallicity (Z), mixing length parameter ($\alpha_{\rm MLT}$) and overshoot parameter (f).

Table 7.1: Physical characteristics and differences between the grids.

Grid	Mass($M_\odot$)	Diffusion	Overshoot	$\Delta Y/\Delta Z$
A	0.7-1.1	Yes	No	1.4
	1.15	Yes	Yes	
	1.2-1.6	No	Yes	
B	0.7-1.1	Yes	No	2.0
	1.15	Yes	Yes	
	1.2-1.6	No	Yes	

Table 7.2: Input parameter range for the grids.

	Range	Step
M_* ($M_\odot$)	0.7-1.6	0.05
Z	0.004-0.04	0.002
$\alpha_{\rm MLT}$	1.0-3.0	0.4
f	0.0-0.03	0.005

For each computed model, the corresponding oscillation frequencies for spherical degrees l = 0, 1, 2, and 3 were computed using GYRE.

7.2 *Kepler* LEGACY Sample

The target sample considered in this study consists of some of the highest signal-to-noise solar-type stars observed by the *Kepler* satellite, with at least 12 months of short-cadence data (Δt = 58.89s) observed by the *Kepler* satellite. In particular, our sample consists of 66 *Kepler* LEGACY sample stars [16, 28]. These stars are located in the main sequence and early subgiant stage. Figure 7.1 shows the distribution of our sample in a HR diagram.

We use the observed frequencies from [16], selecting those modes whose detection probability is high. Classical parameters, which are presented in Table A.1, were extracted from different sources. Values of $T_{\rm eff}$ were taken from [38], except for KIC 12069424 and KIC 12069449 (16 Cyg A and 16 Cyg

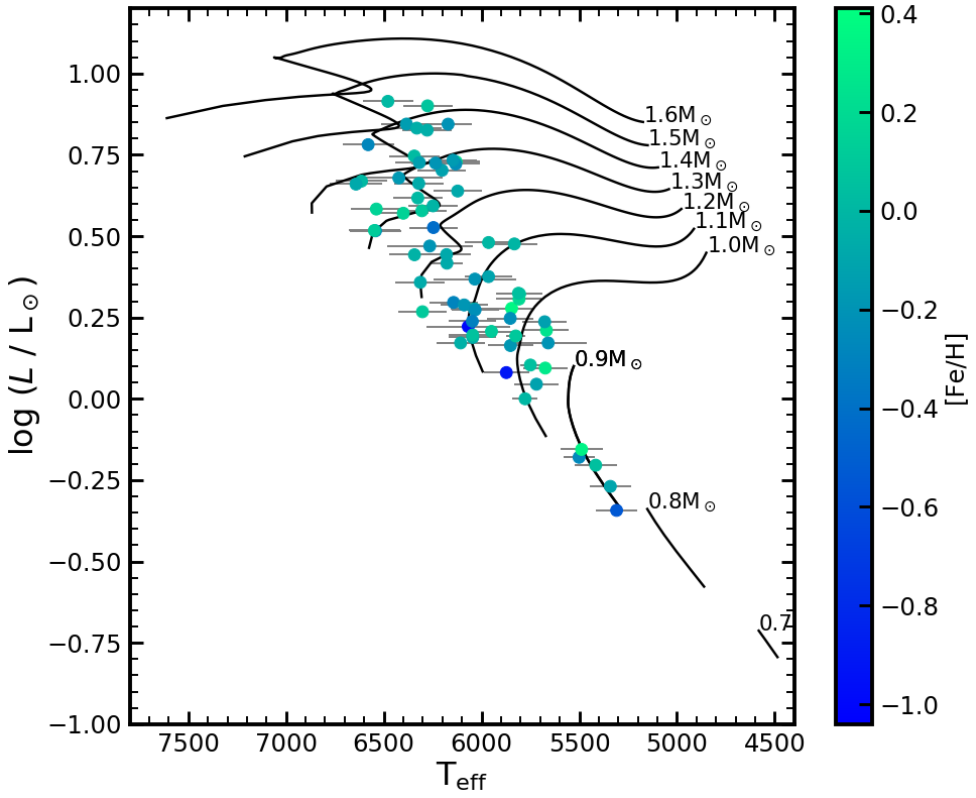

Figure 7.1: Stars from the *Kepler* LEGACY sample in HR diagram. Black lines correspond to evolutionary tracks of stars with different masses (indicated in units of $M_\odot$) at constant metallicity, $Z = 1.8$. The color of each point represents the observed iron content of the respective star.

B), which were taken from [39], and for KIC 7871531 and KIC 10454113, taken from [40]. Values of [Fe/H] were taken from [40], with the exception of 16 Cyg A and 16 Cyg B, whose values were taken from [39].

Finally, the luminosity values for 16 Cyg A and 16 Cyg B were taken from [39]. For the remaining stars, these had to be calculated. For the most part, we used eq. 2.16 to determine them, taking into account $T_{\rm eff}$ and the GAIA-parallax-based radius (R_*) from [38]. For KIC 7871531 and KIC 10454113, L_* was calculated taking into account the photometric parameters and using eq. 2.17. Parallaxes (π) were taken from SIMBAD as well as the magnitude in the V band. The extinction in the V band (A_V) was taken from [40] and the bolometric correction (BC_V) was obtained from the polynomial expansion in [41],

$$BC_V = a + b(\log T_{\rm eff}) + c(\log T_{\rm eff})^2 + d(\log T_{\rm eff})^3 + \ \ldots\ , \tag{7.2}$$

where the coefficients $a,\ b,\ c, \ldots$ are shown in Table A.2.

7.3 Results

We ran AIMS for our sample of 66 stars twice for each of the grids, one considering L_* as a constraint, and another where we do not consider it. The other classical parameters, namely, $T_{\rm eff}$ and [Fe/H], were considered in all cases, in addition to the list of oscillation frequencies for each star. First, we will assess what are the effects of considering luminosity as a constraint for a given grid. Then, we will compare our results with those in the literature, specifically those from [26]. Finally, we will compare the abundances of helium we obtained with the values obtained based on glitches [14].

The following plots show the relative deviations of the stellar parameters given by

$$\Delta x = \frac{x_a - x_b}{x_b}, \tag{7.3}$$

where x can be any parameter (M_*, R_*, $\bar{\rho}$, age and $Y_{\rm s}$), x_a is the value returned by the grid modeling, and x_b is the value taken as reference (when we compare between grids, we will use Grid A as a reference.). In our analysis, we use median statistics [42], which is not affected by outliers.

The median (μ) is the value for which 50% of the sampled values are either above or below. For the standard deviation (σ), we use the percentiles, with 1σ being the region that includes $\sim 68\%$ of the sample values about the median value.

In the appendix we present the derived values for the mass, radius, density, and age (in Tables A.3, A.4, A.5, and A.6) from each modeling procedure.

7.3.1 Impact of Luminosity Constraint on the Optimization

We look into the effect of including the luminosity as a classical constraint in our optimization procedure. For Grid A, Figs. 7.2 to 7.5 present the relative deviation for each of the different parameters M_*, R_*, $\bar{\rho}$, and t_*. For Grid B, the same is done in Figs. 7.6 to 7.9.

For most of the stars, the inclusion of the luminosity as a constraint in the optimization procedure does not lead to a significant relative desviation of the stellar parameters. The bias (median) is always close to zero and a small dispersion (standard deviation), can be seen which indicates that the effect of including the stellar luminosity as a constraint is negligible.

For Grid B we can identify a larger number of extreme points compared to Grid A. This may be due to the fact that, when we change the abundance of helium, an increase of the mean molecular weight ensues which increases the rate of nuclear reactions, which in turn leads to an increase in energy production that induces a higher luminosity for a given mass. Consequently, we are led to the conclusion that the helium derived from Grid B is harder to reconcile with the luminosity observed for some of our target stars.

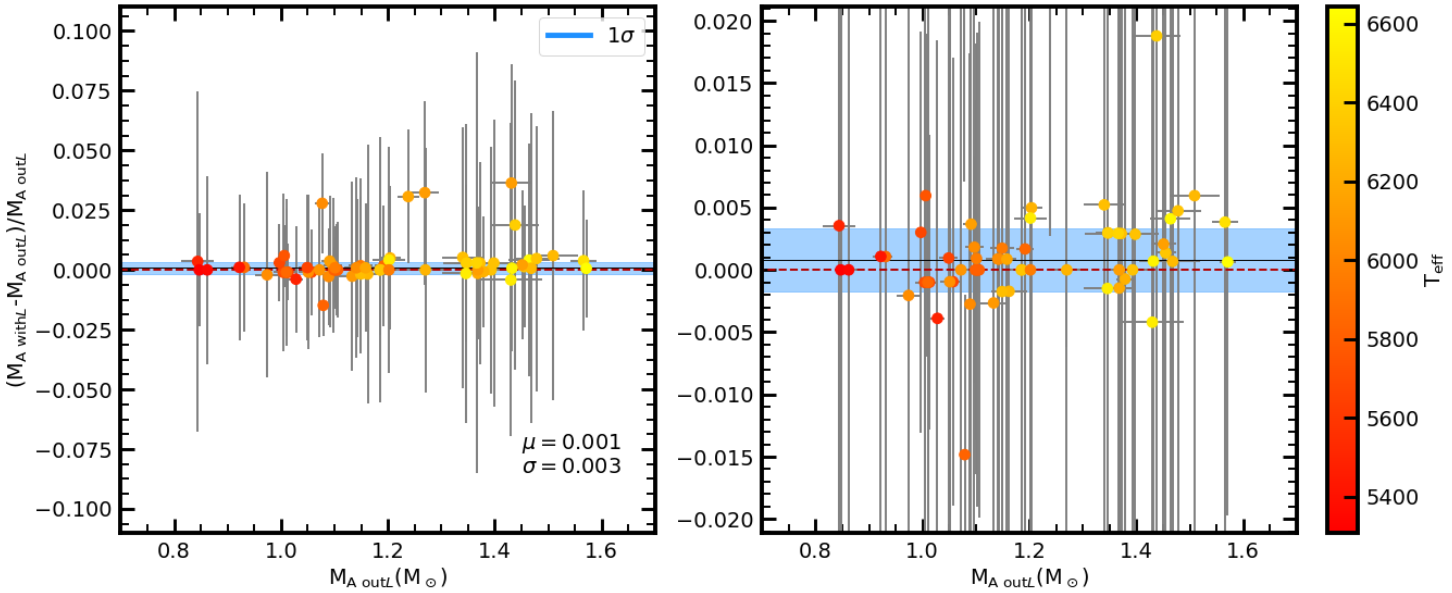

Figure 7.2: Relative mass deviation for Grid A resulting from the inclusion of L_* as a constraint in the optimization procedure. The panel on the left shows all stars. The panel on the right shows a close-up of the confidence interval region, highlighting the dispersion of the points close to the bias (continuous horizontal line).

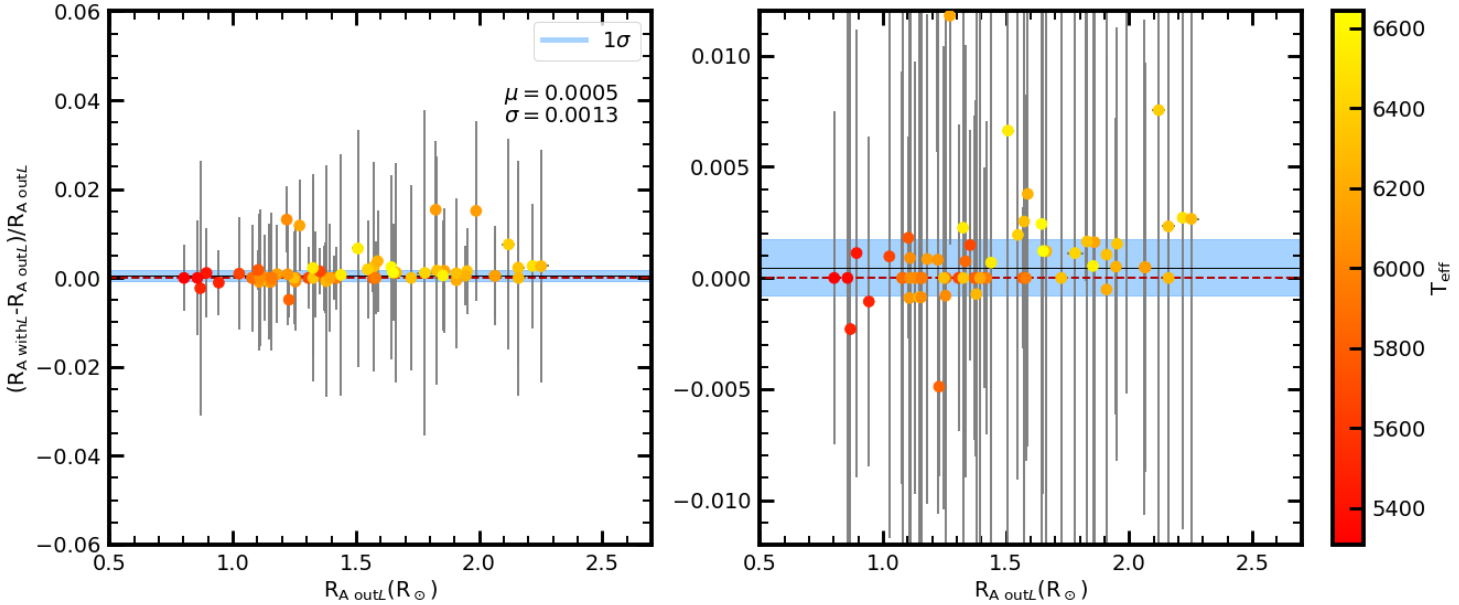

Figure 7.3: Relative radius deviation for Grid A resulting from the inclusion of L_* as a constraint in the optimization procedure. The panel on the left shows all stars. The panel on the right shows a close-up of the confidence interval region, highlighting the dispersion of the points close to the bias (continuous horizontal line)

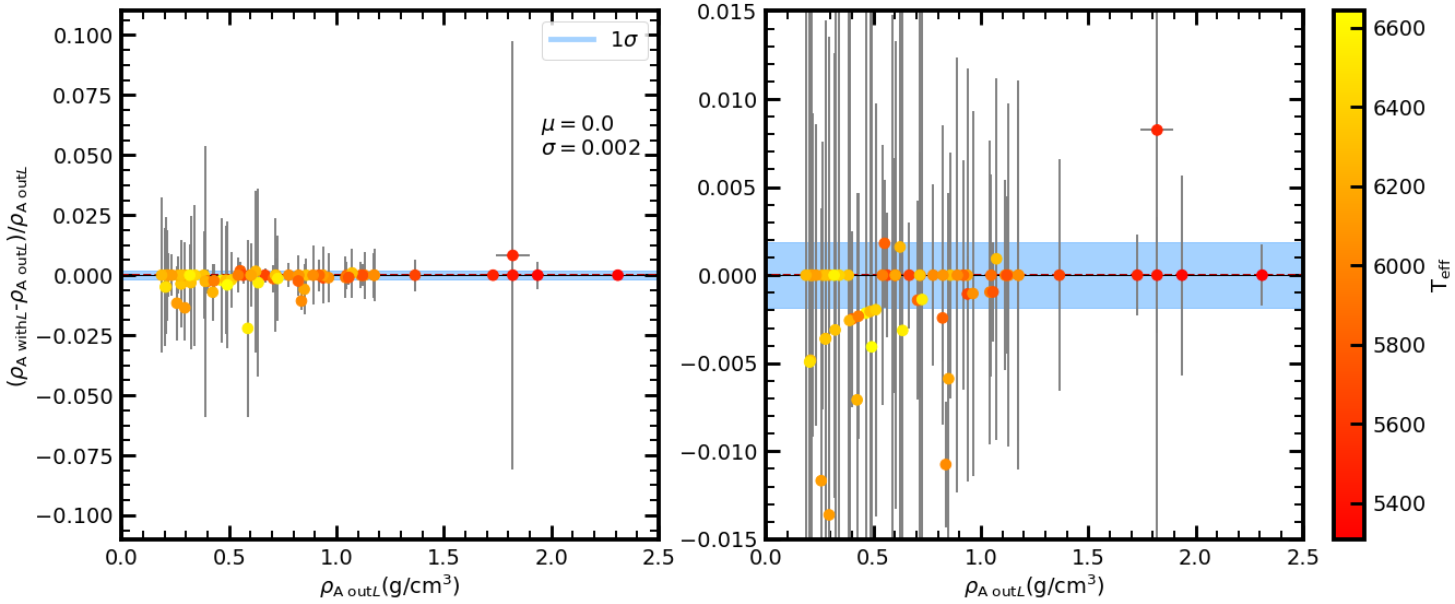

Figure 7.4: Relative density deviation for Grid A resulting from the inclusion of L_* as a constraint in the optimization procedure. The panel on the left shows all stars. The panel on the right shows a close-up of the confidence interval region, highlighting the dispersion of the points close to the bias (continuous horizontal line).

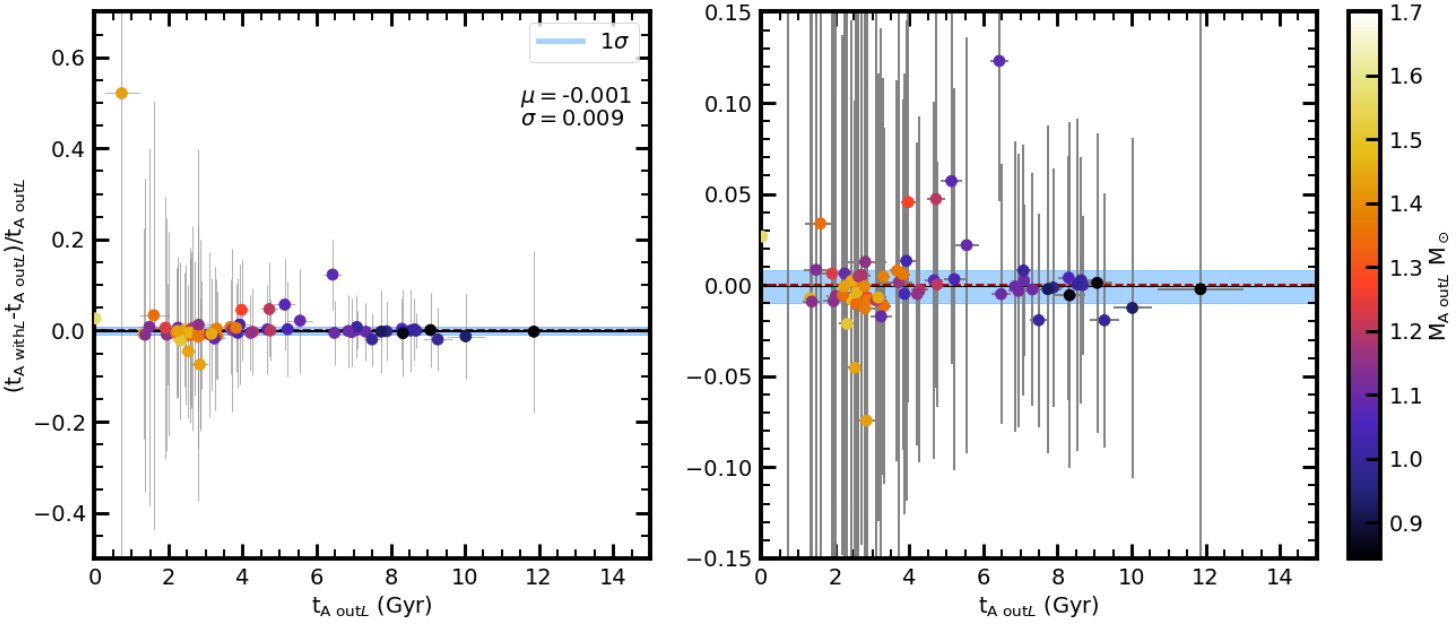

Figure 7.5: Relative age deviation for Grid A resulting from the inclusion of L_* as a constraint in the optimization procedure. The panel on the left shows all stars. The panel on the right shows a close-up of the confidence interval region, highlighting the dispersion of the points close to the bias (continuous horizontal line)

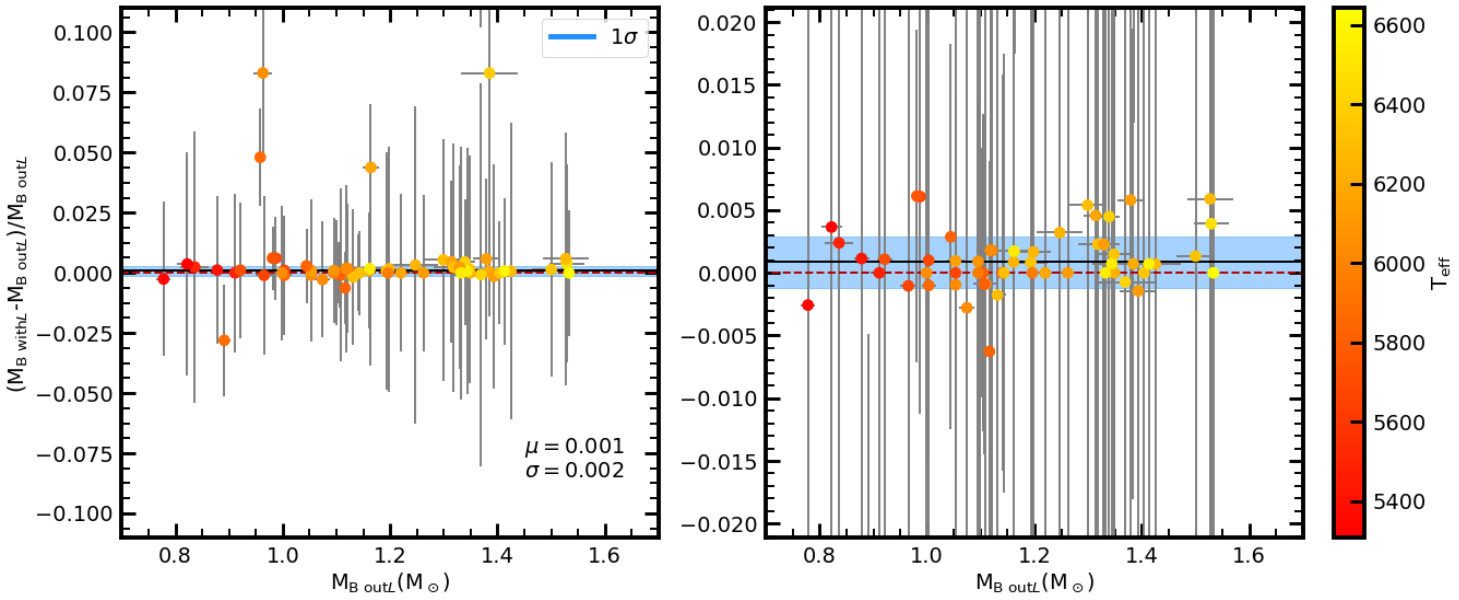

Figure 7.6: Relative mass deviation for Grid B resulting from the inclusion of L_* as a constraint in the optimization procedure. The panel on the left shows all stars. The panel on the right shows a close-up of the confidence interval region, highlighting the dispersion of the points close to the bias (continuous horizontal line)

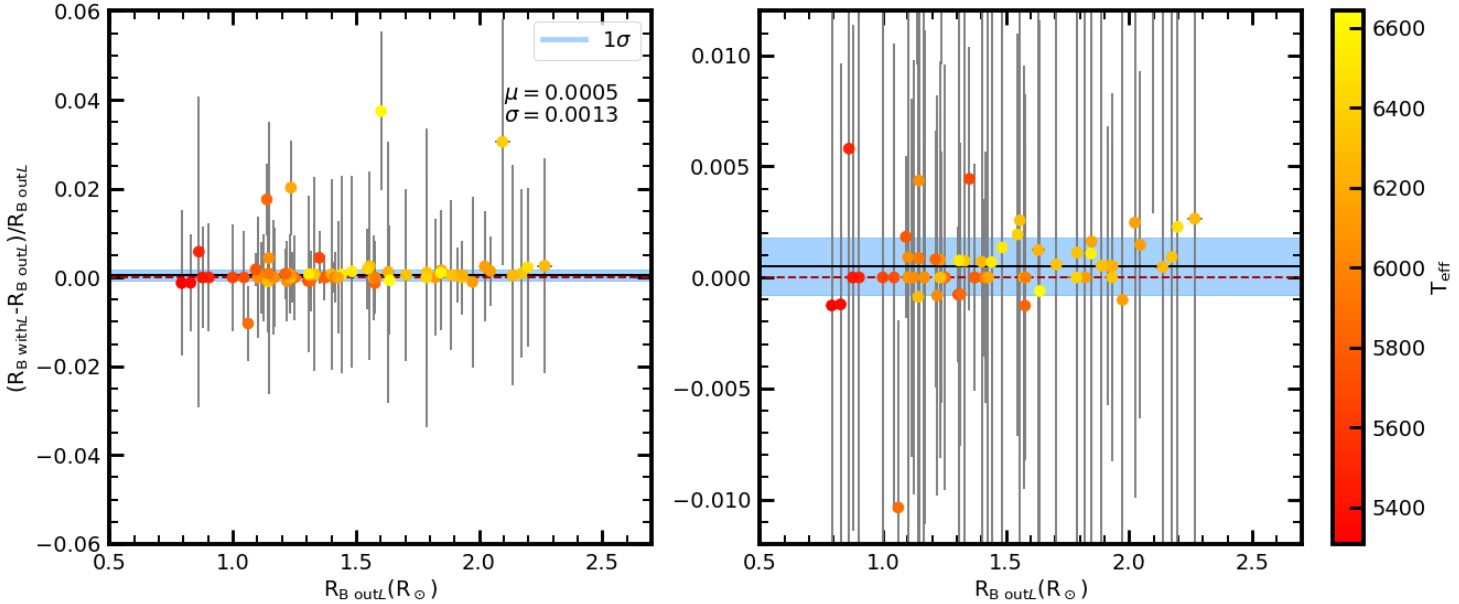

Figure 7.7: Relative radius deviation for Grid B resulting from the inclusion of L_* as a constraint in the optimization procedure. The panel on the left shows all stars. The panel on the right shows a close-up of the confidence interval region, highlighting the dispersion of the points close to the bias (continuous horizontal line)

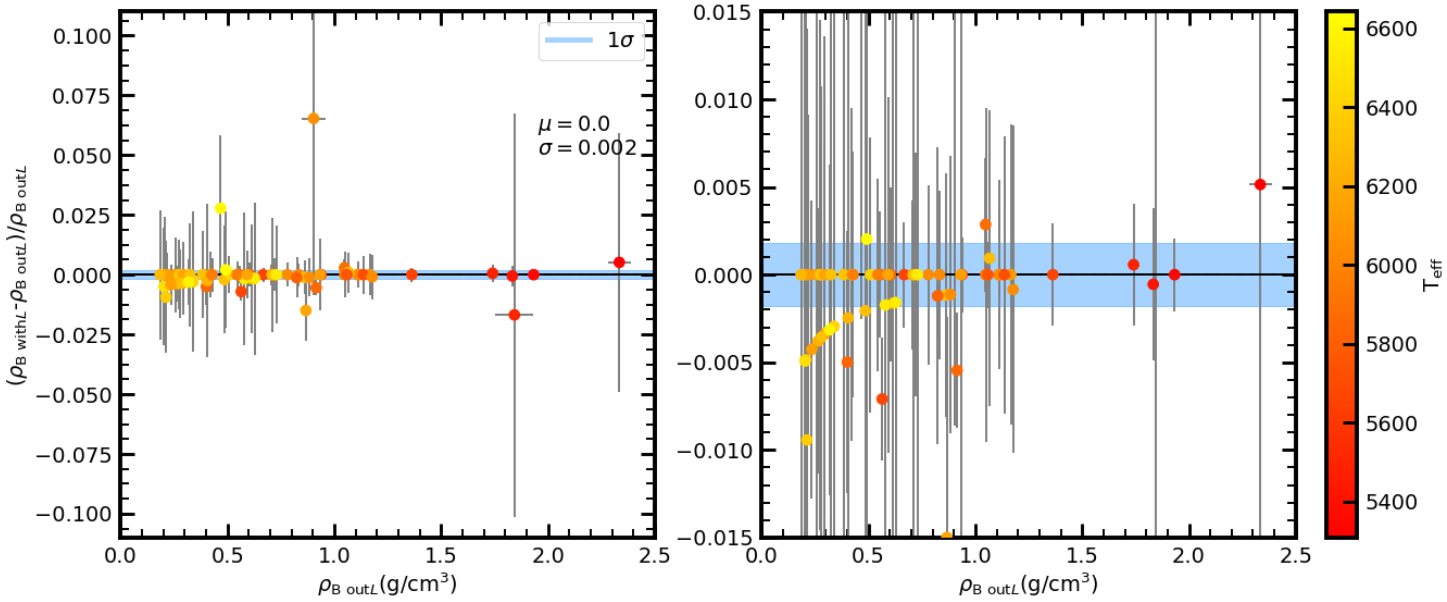

Figure 7.8: Relative density deviation for Grid B resulting from the inclusion of L_* as a constraint in the optimization procedure. The panel on the left shows all stars. The panel on the right shows a close-up of the confidence interval region, highlighting the dispersion of the points close to the bias (continuous horizontal line)

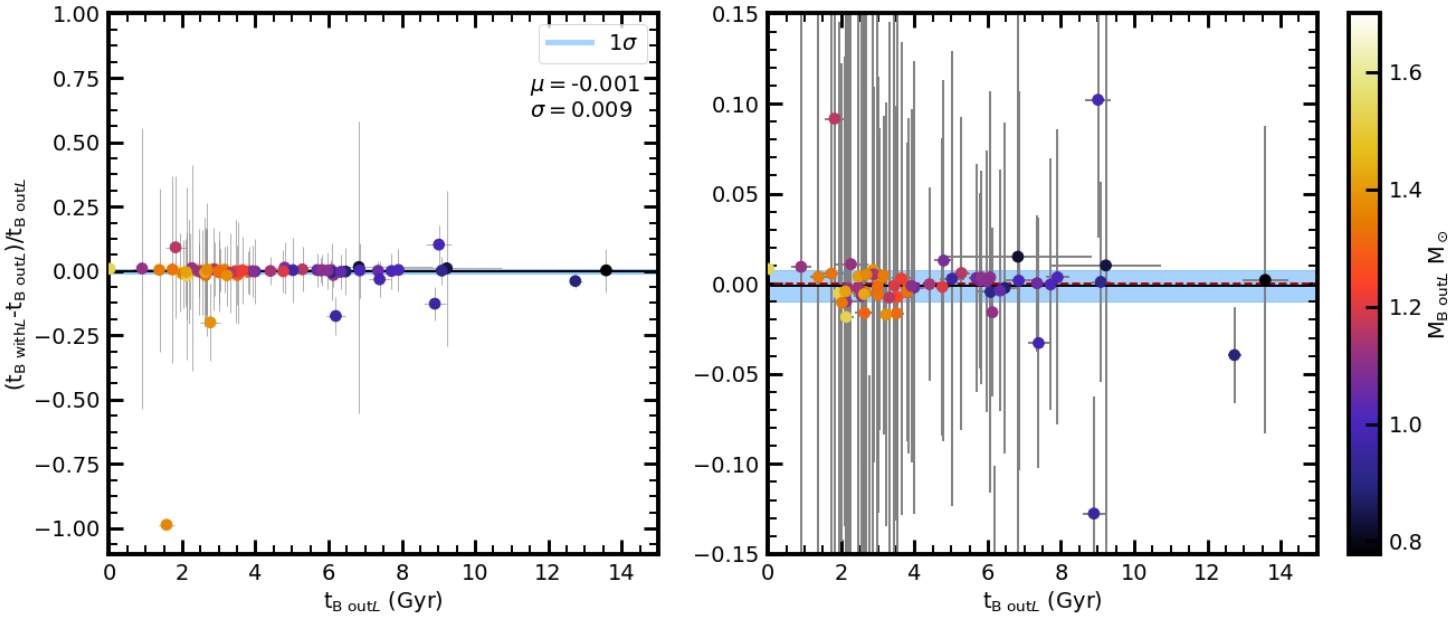

Figure 7.9: Relative age deviation for Grid B resulting from the inclusion of L_* as a constraint in the optimization procedure. The panel on the left shows all stars. The panel on the right shows a close-up of the confidence interval region, highlighting the dispersion of the points close to the bias (continuous horizontal line)

7.3.2 Comparison with the Literature

Before comparing the values obtained with the two grids, we will compare them with results in the literature. We resort to [26], where the authors present different sets of results based on different codes. For this comparison we use three of the available sets of results, namely, ASTFIT, BASTA, and YMCM. In the appendix we show the tables containing the stellar parameters obtained by each of the above three codes as well as the comparison plots (ASTFIT: Figs. 7.10 to 7.17; BASTA: Figs. 7.18 to 7.25; YMCM: Figs. 7.26 to 7.33).

Concerning the relative deviations with respect to Grid A, we see that for the mass (Figs. 7.10, 7.18, and 7.26), the ASTFIT and BASTA codes lead to a positive bias while YMCM leads to a negative bias. The dispersion is seen to be largest when comparing to ASTFIT. For the radius (Figs. 7.11, 7.19, and 7.27), we find similar results to those for the mass. For the density (Figs. 7.12, 7.20, and 7.28), results present a bias closer to zero and a smaller dispersion. Finally, for the age (Figs. 7.13, 7.21, and 7.29), we find the largest dispersion, especially for the higher-mass stars, which have the smallest ages. We notice that no significant variation is observed when including the luminosity as an input, which was to be expected from what we have seen in the previous section.

With respect to Grid B, and starting with the mass (Figs. 7.14, 7.22, and 7.30), we see that the bias is now smaller and negative. This is due to the fact that $\frac{\Delta Y}{\Delta Z}$ is larger than for Grid A, with the resulting larger abundance of helium leading to a larger mean molecular weight, in turn causing a larger rate of nuclear reactions which produces more energy and promotes a higher L_* and $T_{\rm eff}$. This way, if we keep the same constraints in $T_{\rm eff}$ and L_*, it is necessary to decrease the mass to obtain matching values. For the radius (Figs. 7.15, 7.23, and 7.31), we can make similar remarks as those for the mass. For density (Figs. 7.16, 7.24, and 7.32), we find a similar result to that obtained with Grid A, which is due to the individual frequency constraints, which are very sensitive to the density, being the same in both cases. For the age (Figs. 7.17, 7.25, and 7.33), we draw similar conclusions to those based on Grid A.

Overall, results obtained present a small bias, even when considering the dispersion value. This way, the confidence interval turns out to be around zero, indicating that the parameters obtained are in agreement with those in the literature. Nevertheless, for a few stars, the differences are substantial. While it was not the aim of this thesis to investigate differences on the individual basis, our results clearly indicate that for such stars further investigation is needed to understand the origin of the differences observed.

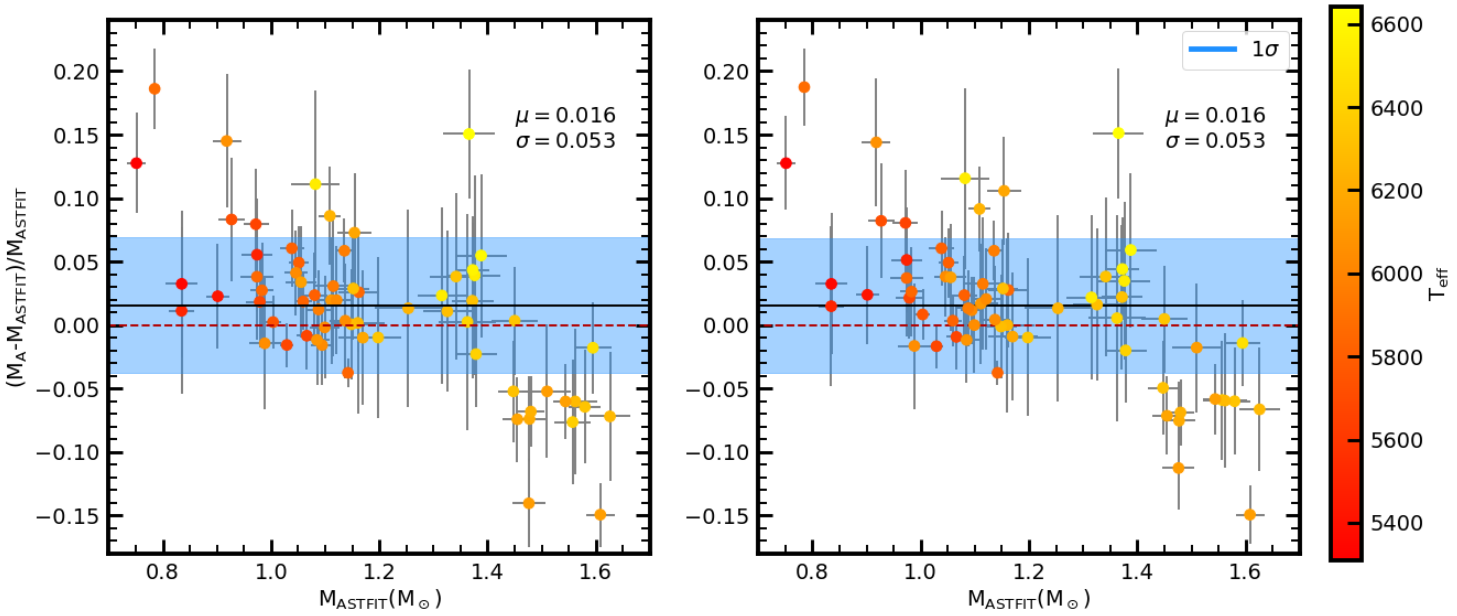

Figure 7.10: Relative mass deviation (comparison of ASTFIT and Grid A results). The left panel presents the results considering $T_{\rm eff}$ and [Fe/H] as classical constraints only. Adding to these, luminosity is also considered as a constraint on the right panel.

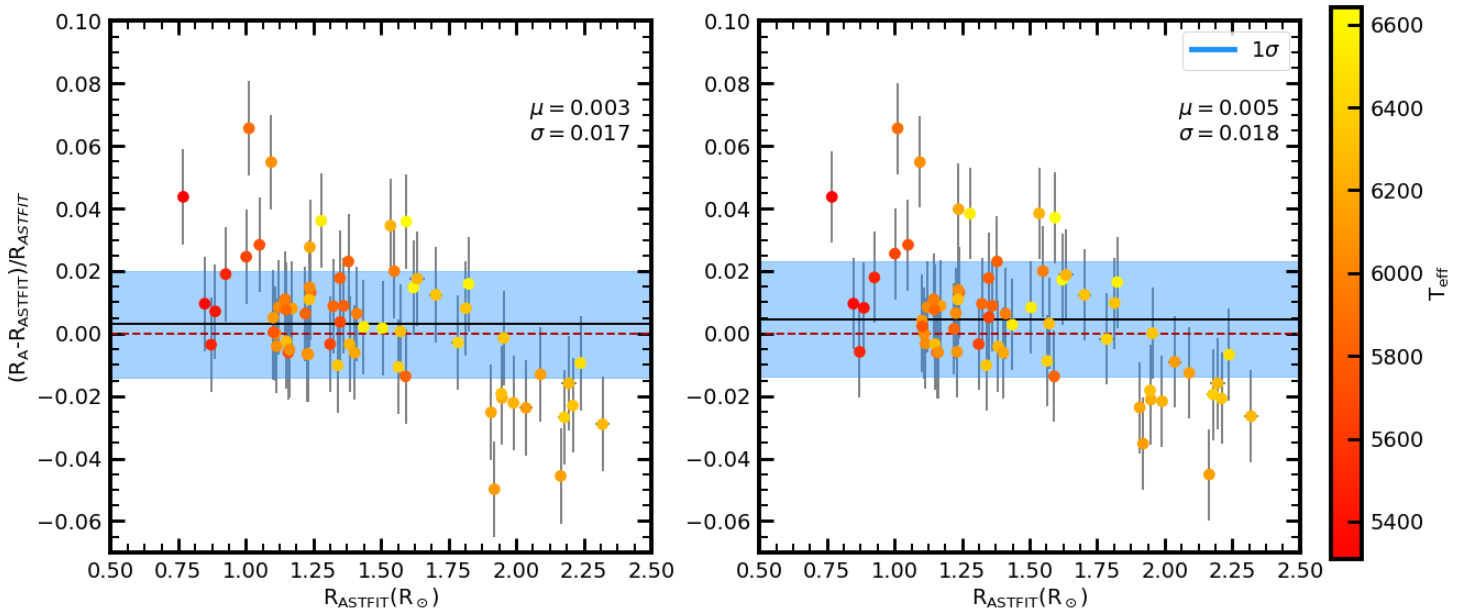

Figure 7.11: Relative radius deviation (comparison of ASTFIT and Grid A results). The left panel presents the results considering $T_{\rm eff}$ and [Fe/H] as classical constraints only. Adding to these, luminosity is also considered as a constraint on the right panel.

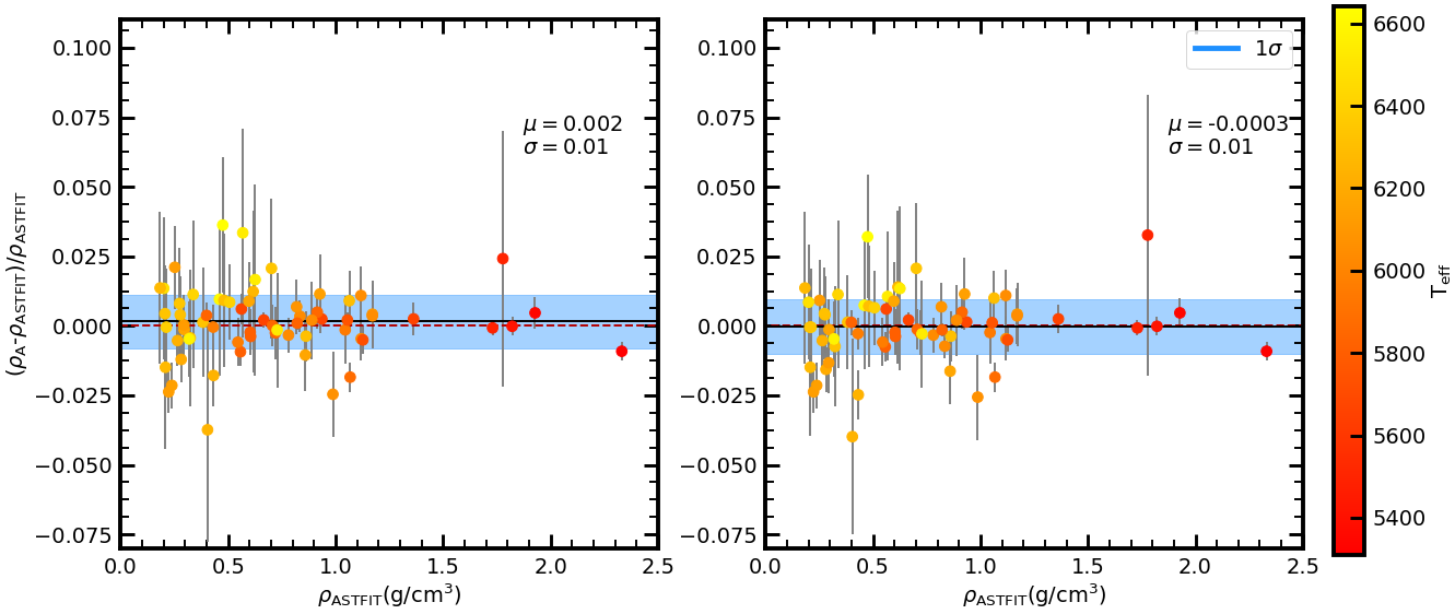

Figure 7.12: Relative density deviation (comparison of ASTFIT and Grid A results). The left panel presents the results considering $T_{\rm eff}$ and [Fe/H] as classical constraints only. Adding to these, luminosity is also considered as a constraint on the right panel.

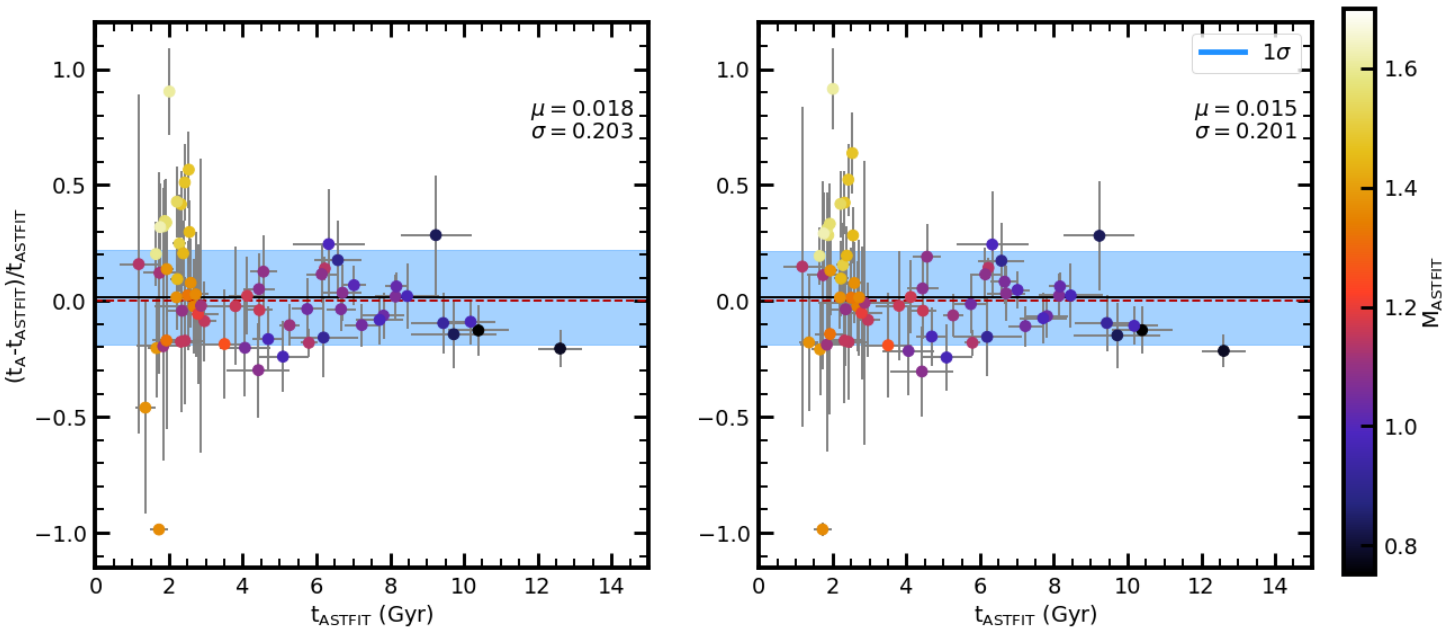

Figure 7.13: Relative age deviation (comparison of ASTFIT and Grid A results). The left panel presents the results considering $T_{\rm eff}$ and [Fe/H] as classical constraints only. Adding to these, luminosity is also considered as a constraint on the right panel.

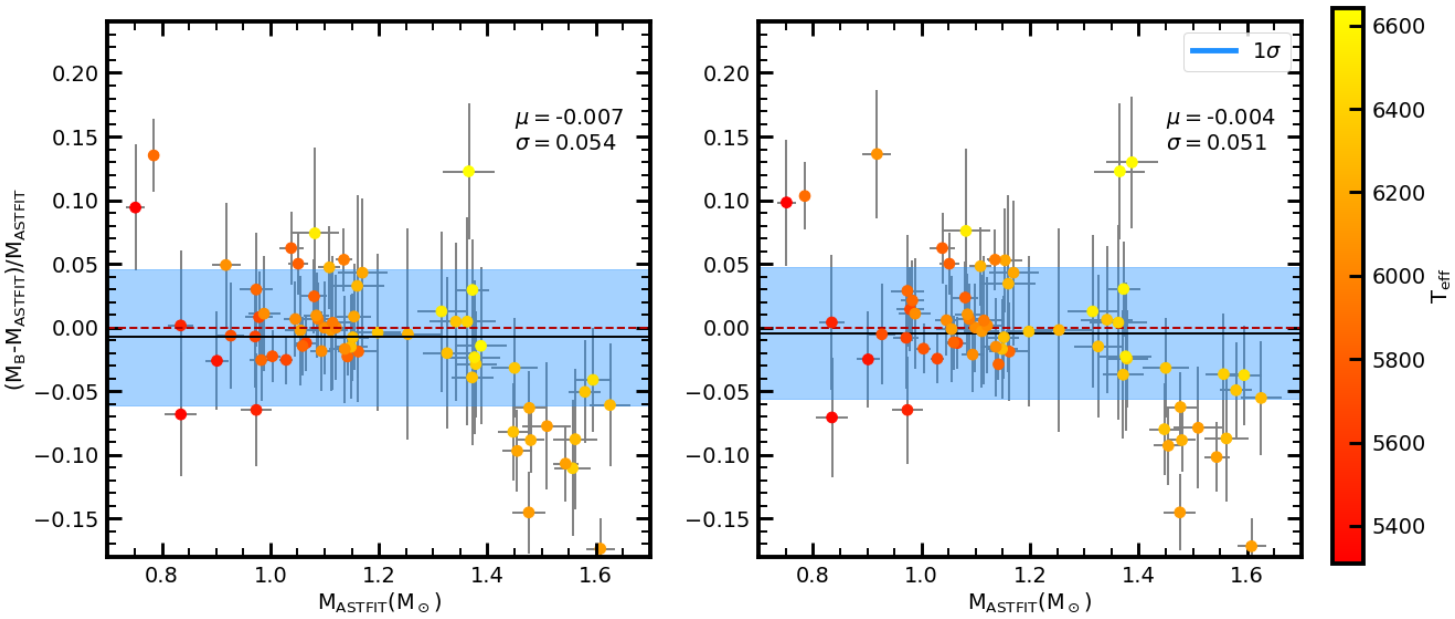

Figure 7.14: Relative mass deviation (comparison of ASTFIT and Grid B results). The left panel presents the results considering $T_{\rm eff}$ and [Fe/H] as classical constraints only. Adding to these, luminosity is also considered as a constraint on the right panel.

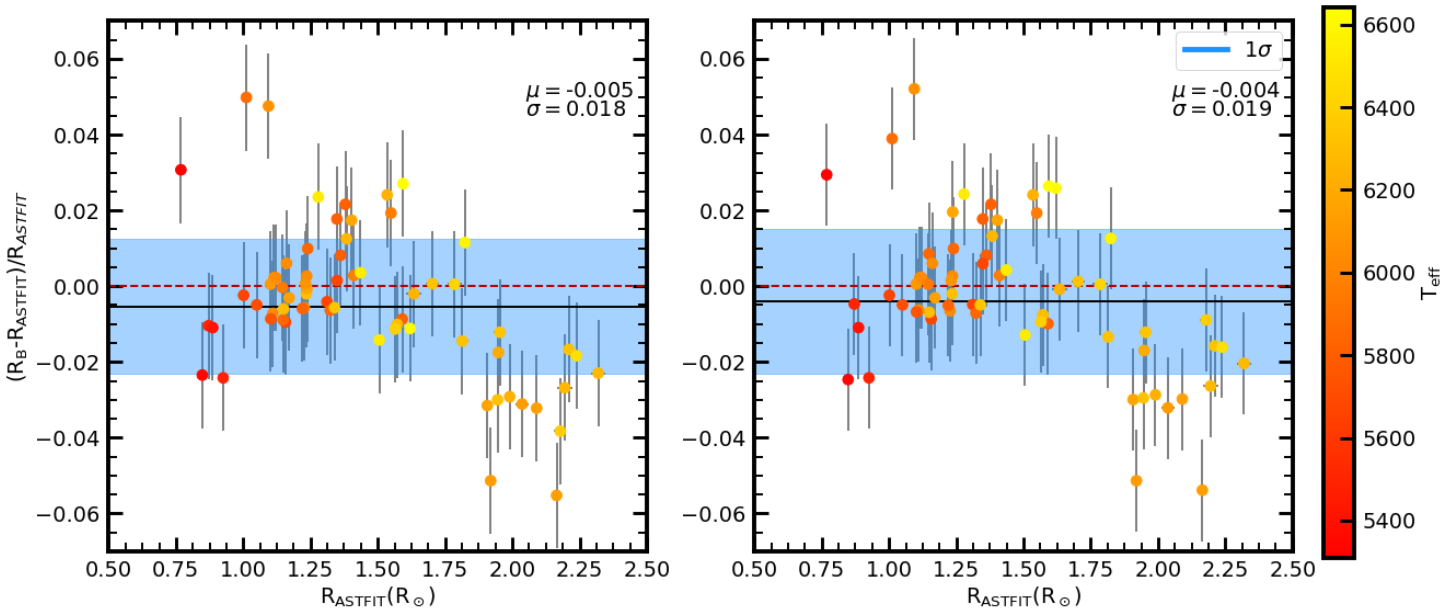

Figure 7.15: Relative radius deviation (comparison of ASTFIT and Grid B results). The left panel presents the results considering $T_{\rm eff}$ and [Fe/H] as classical constraints only. Adding to these, luminosity is also considered as a constraint on the right panel.

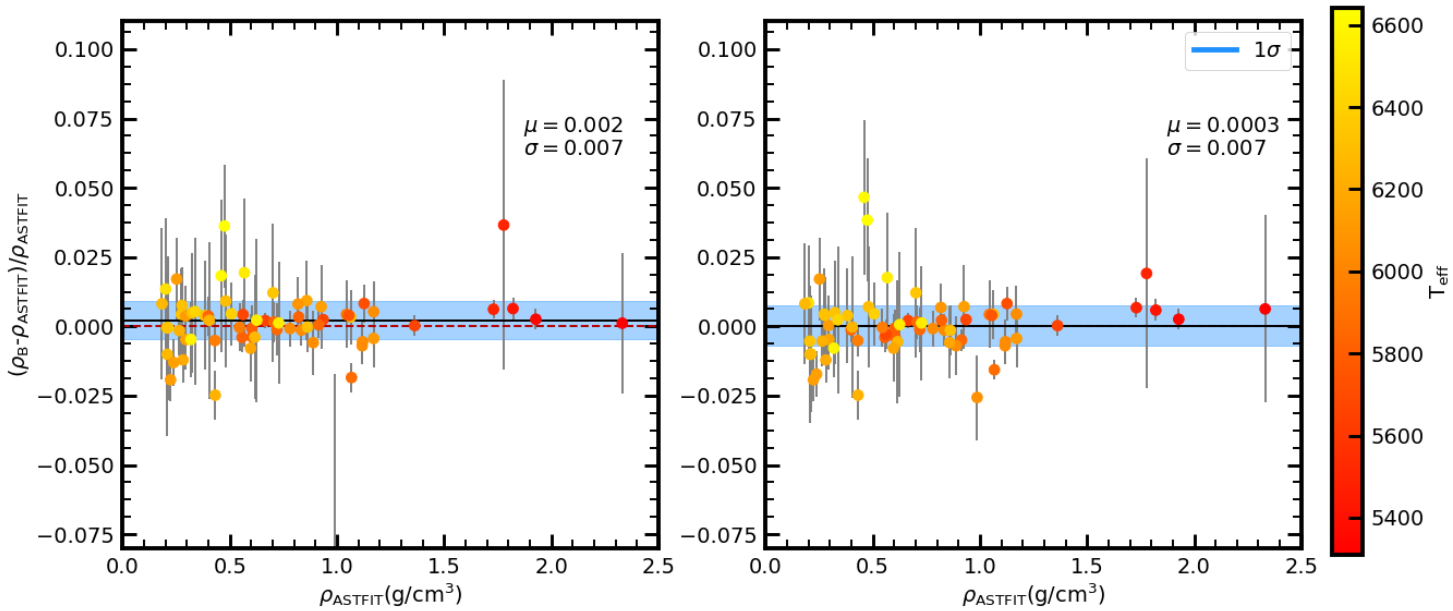

Figure 7.16: Relative density deviation (comparison of ASTFIT and Grid B results). The left panel presents the results considering $T_{\rm eff}$ and [Fe/H] as classical constraints only. Adding to these, luminosity is also considered as a constraint on the right panel.

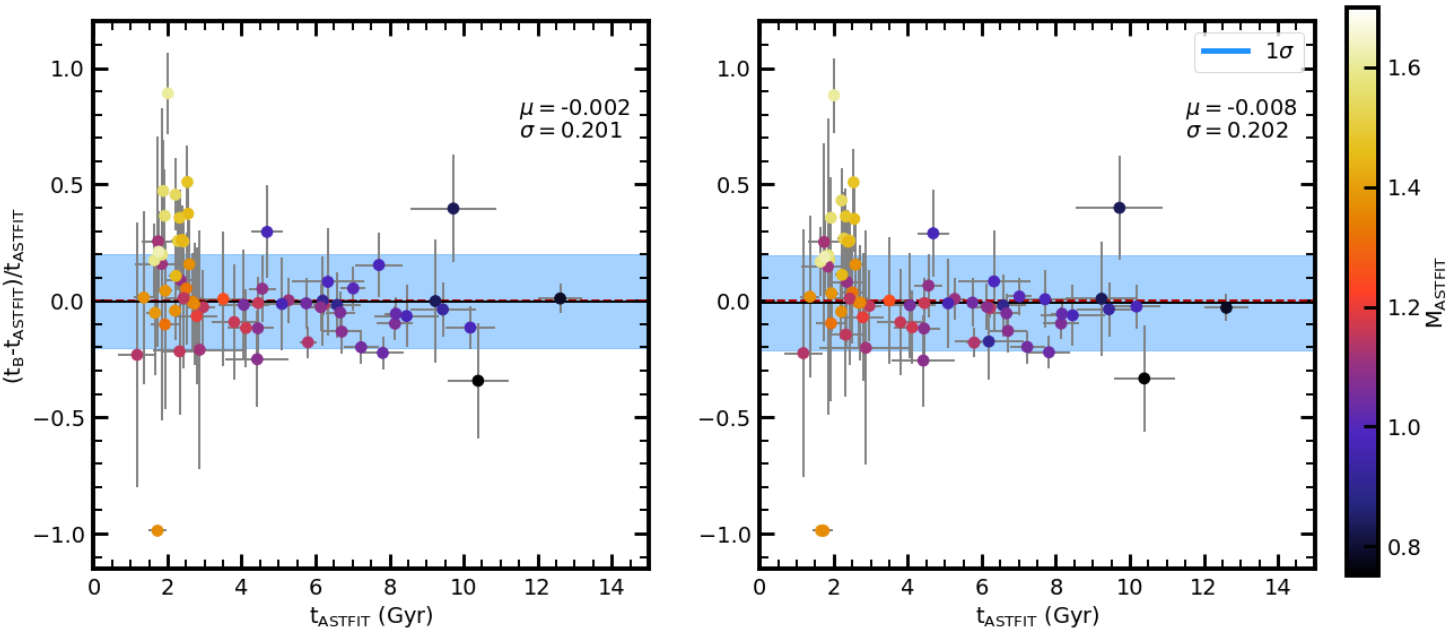

Figure 7.17: Relative age deviation (comparison of ASTFIT and Grid B results). The left panel presents the results considering $T_{\rm eff}$ and [Fe/H] as classical constraints only. Adding to these, luminosity is also considered as a constraint on the right panel.

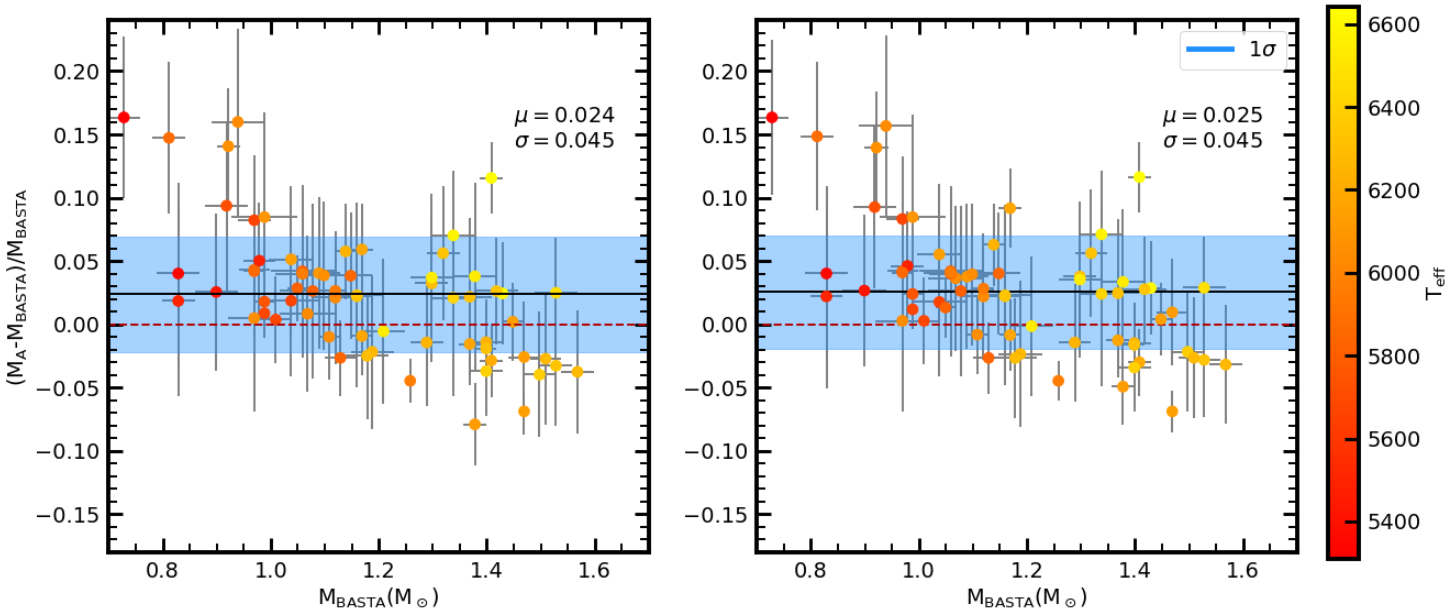

Figure 7.18: Relative mass deviation (comparison of BASTA and Grid A results). The left panel presents the results considering $T_{\rm eff}$ and [Fe/H] as classical constraints only. Adding to these, luminosity is also considered as a constraint on the right panel.

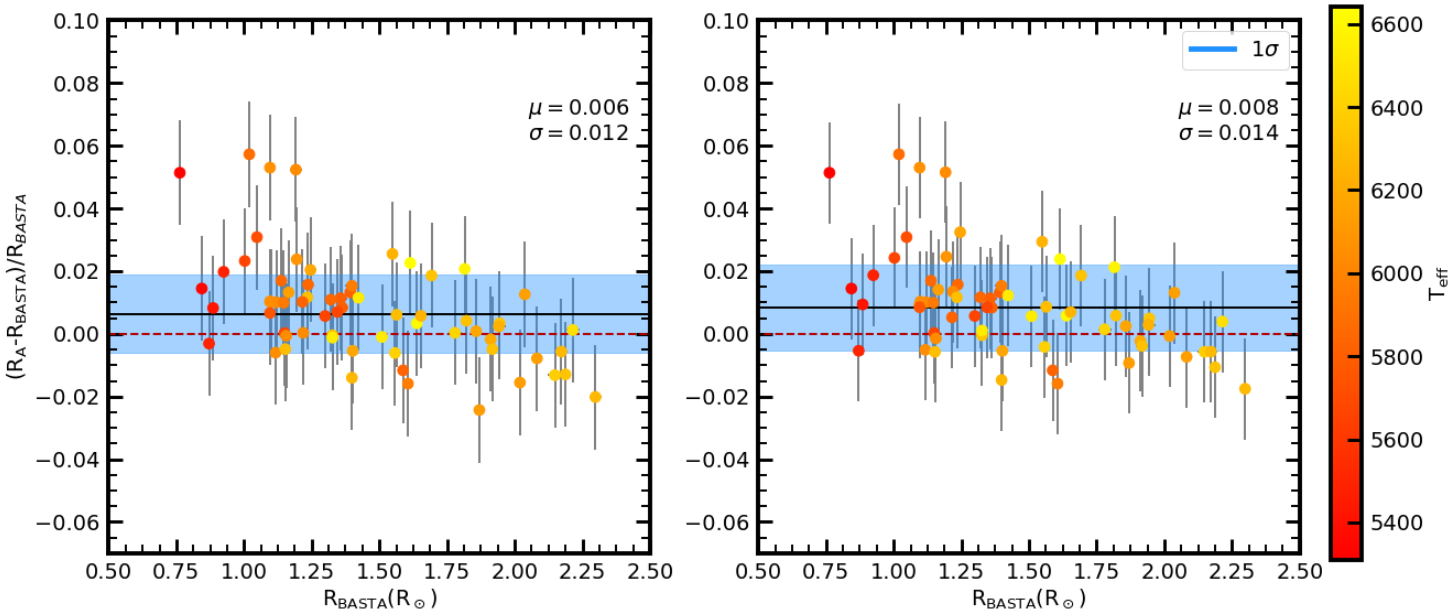

Figure 7.19: Relative radius deviation (comparison of BASTA and Grid A results). The left panel presents the results considering $T_{\rm eff}$ and [Fe/H] as classical constraints only. Adding to these, luminosity is also considered as a constraint on the right panel.

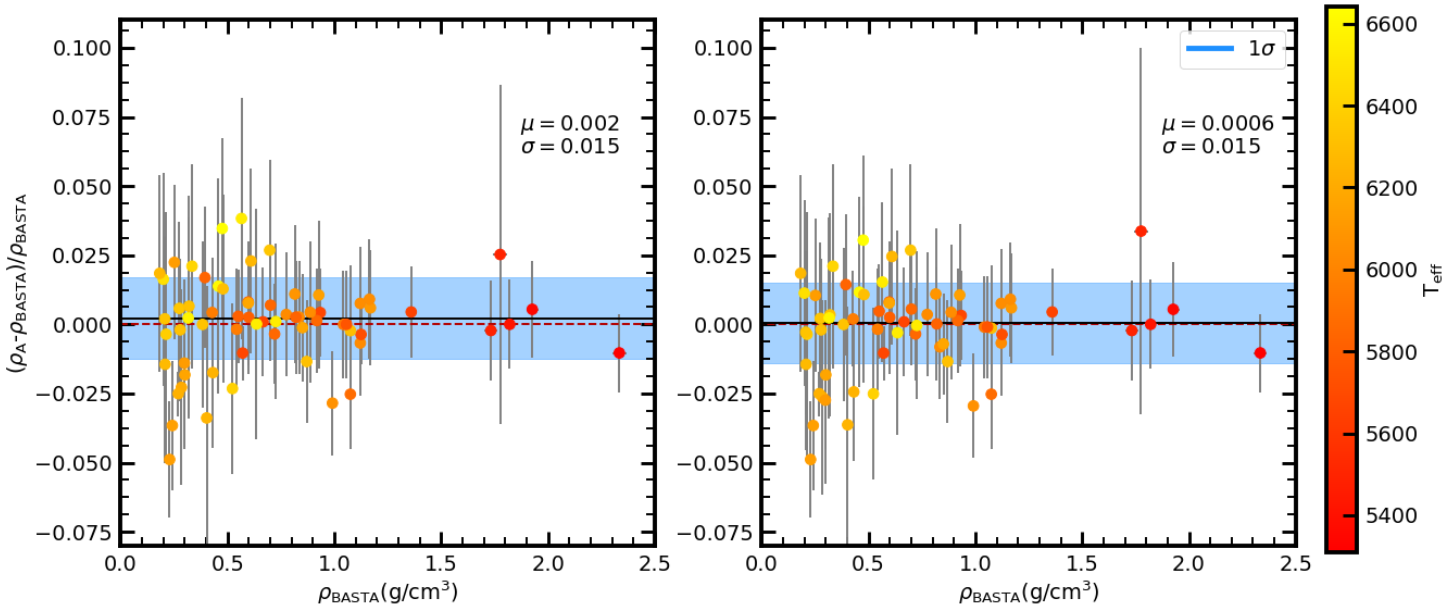

Figure 7.20: Relative density deviation (comparison of BASTA and Grid A results). The left panel presents the results considering $T_{\rm eff}$ and [Fe/H] as classical constraints only. Adding to these, luminosity is also considered as a constraint on the right panel.

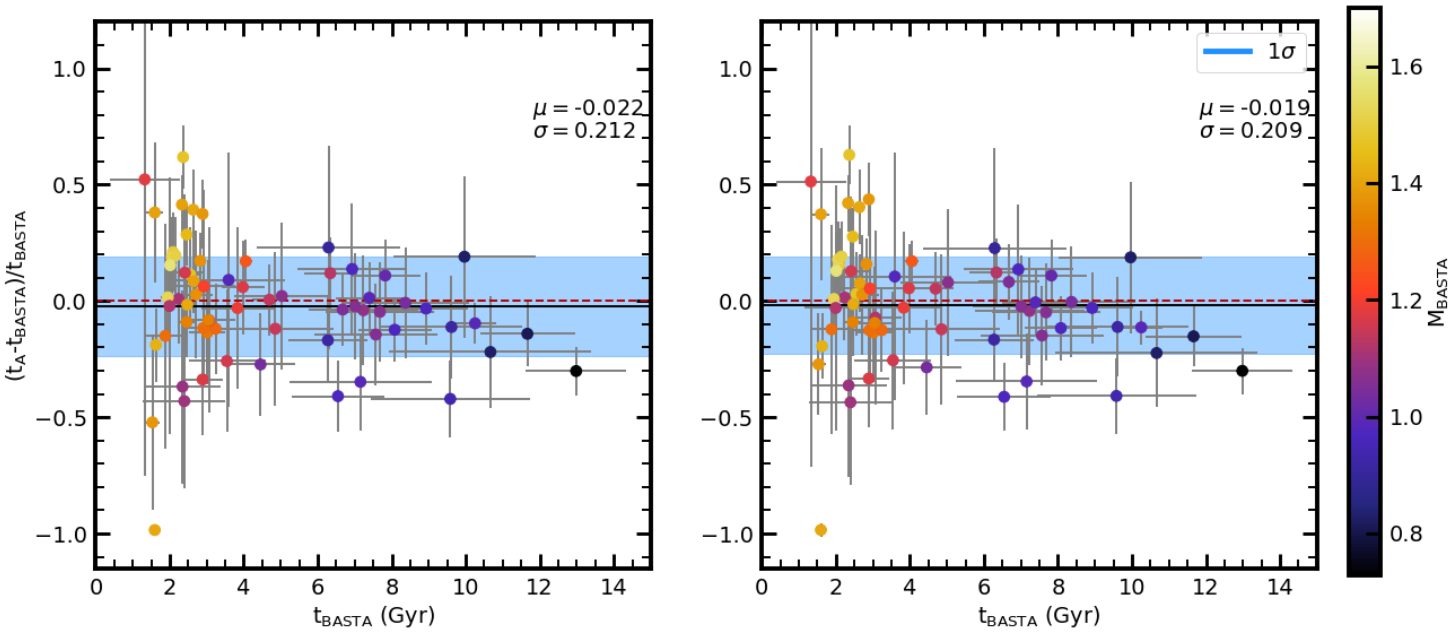

Figure 7.21: Relative age deviation (comparison of BASTA and Grid A results). The left panel presents the results considering $T_{\rm eff}$ and [Fe/H] as classical constraints only. Adding to these, luminosity is also considered as a constraint on the right panel.

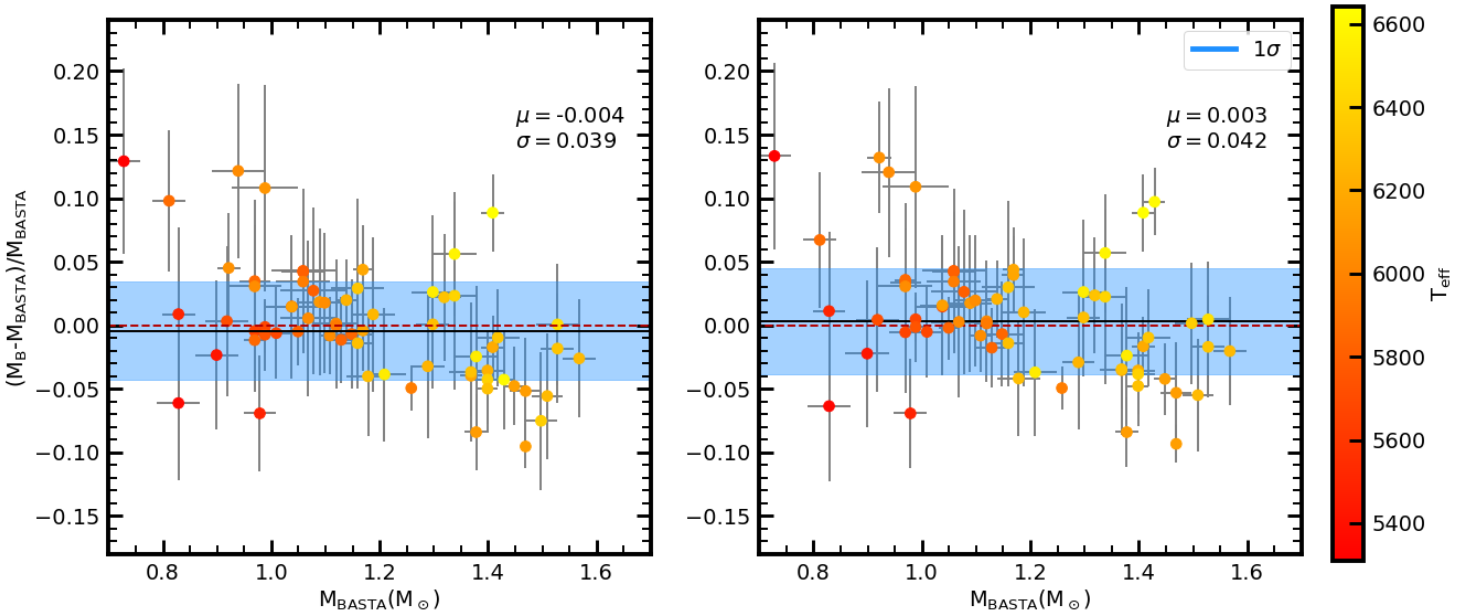

Figure 7.22: Relative mass deviation (comparison of BASTA and Grid B results). The left panel presents the results considering $T_{\rm eff}$ and [Fe/H] as classical constraints only. Adding to these, luminosity is also considered as a constraint on the right panel.

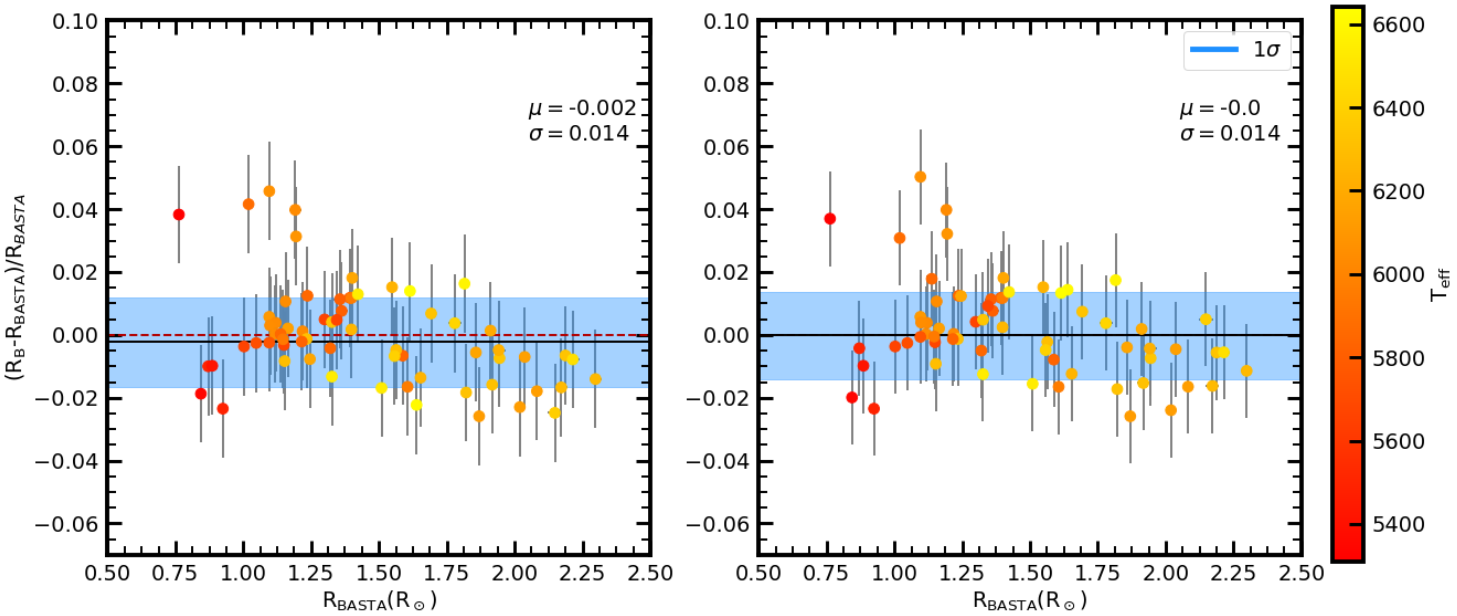

Figure 7.23: Relative radius deviation (comparison of BASTA and Grid B results). The left panel presents the results considering $T_{\rm eff}$ and [Fe/H] as classical constraints only. Adding to these, luminosity is also considered as a constraint on the right panel.

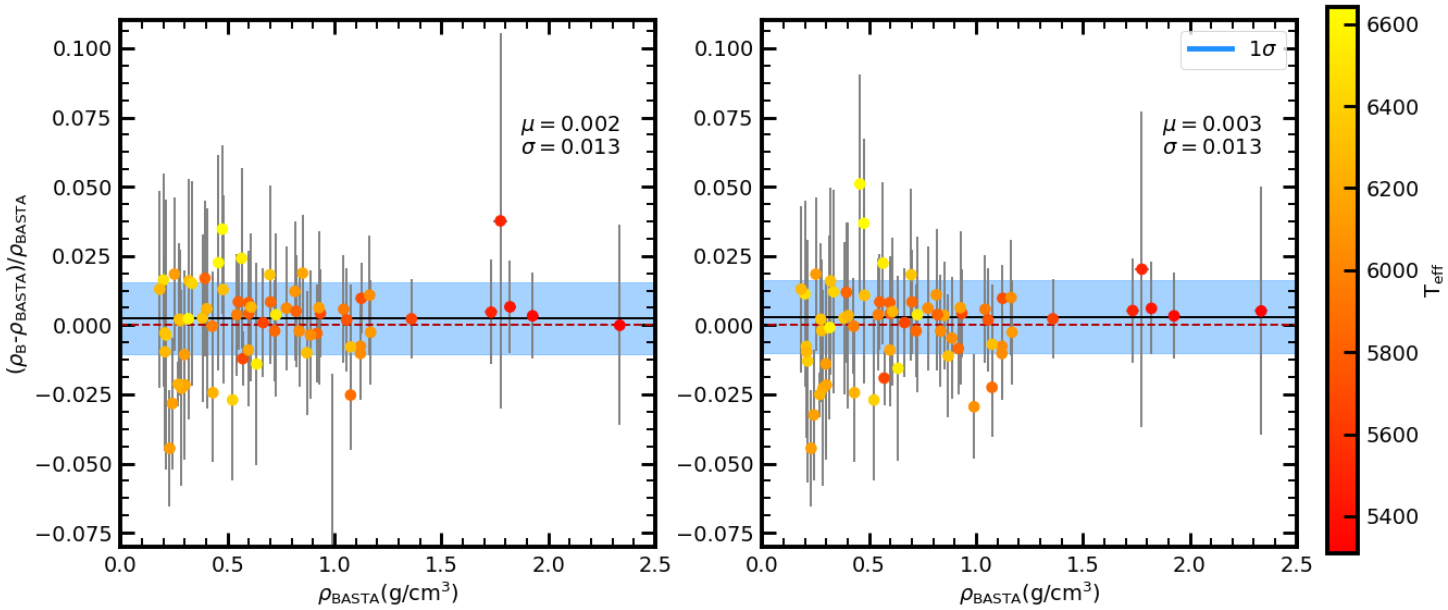

Figure 7.24: Relative density deviation (comparison of BASTA and Grid B results). The left panel presents the results considering $T_{\rm eff}$ and [Fe/H] as classical constraints only. Adding to these, luminosity is also considered as a constraint on the right panel.

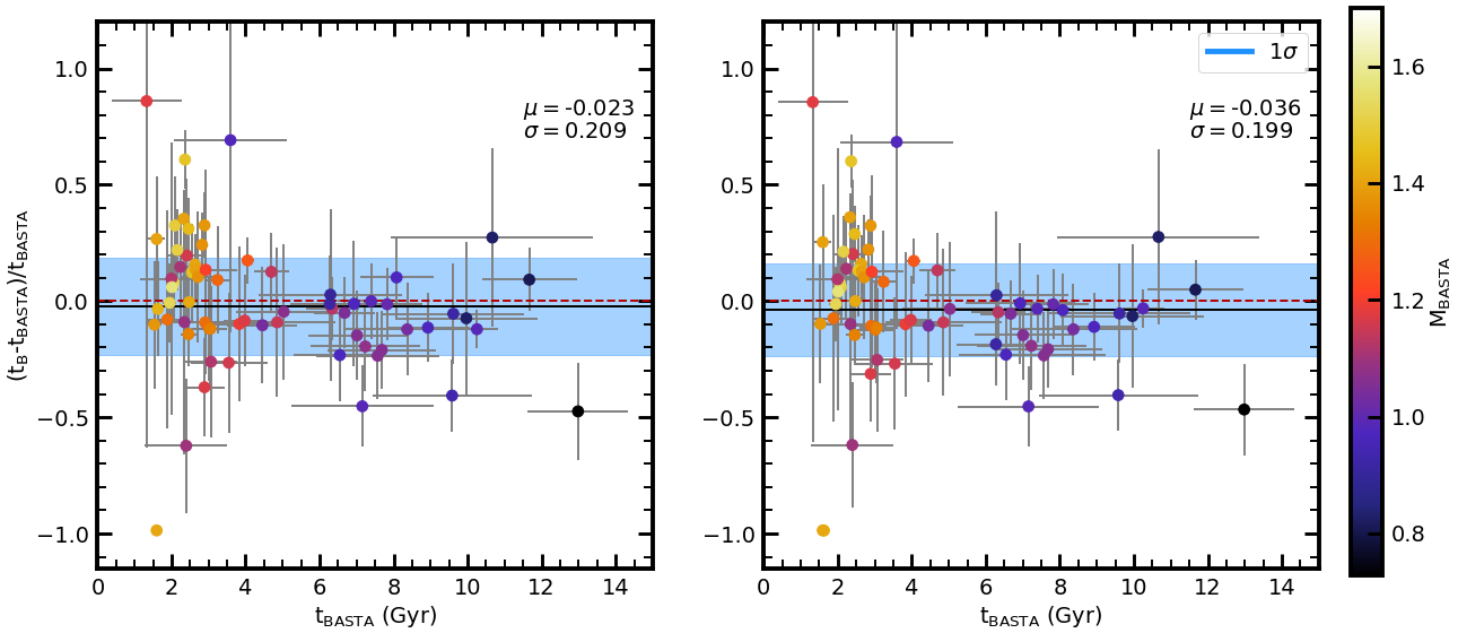

Figure 7.25: Relative age deviation (comparison of BASTA and Grid B results). The left panel presents the results considering $T_{\rm eff}$ and [Fe/H] as classical constraints only. Adding to these, luminosity is also considered as a constraint on the right panel.

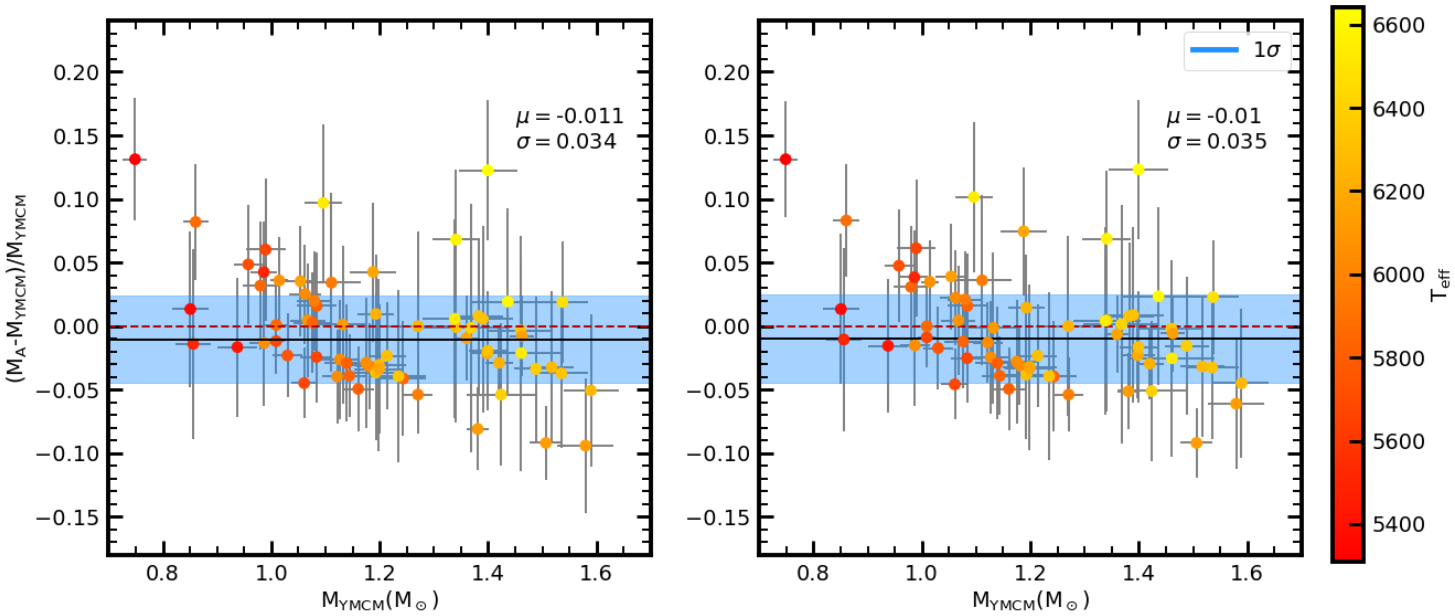

Figure 7.26: Relative mass deviation (comparison of YMCM and Grid A results). The left panel presents the results considering $T_{\rm eff}$ and [Fe/H] as classical constraints only. Adding to these, luminosity is also considered as a constraint on the right panel.

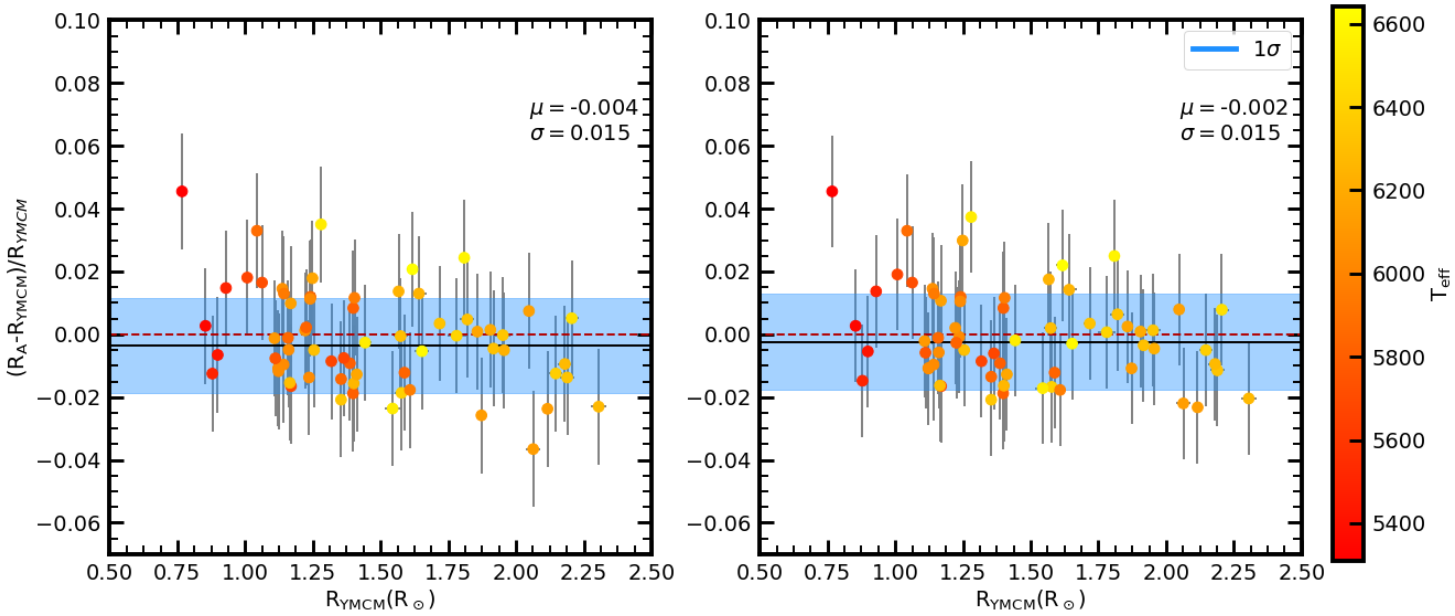

Figure 7.27: Relative radius deviation (comparison of YMCM and Grid A results). The left panel presents the results considering $T_{\rm eff}$ and [Fe/H] as classical constraints only. Adding to these, luminosity is also considered as a constraint on the right panel.

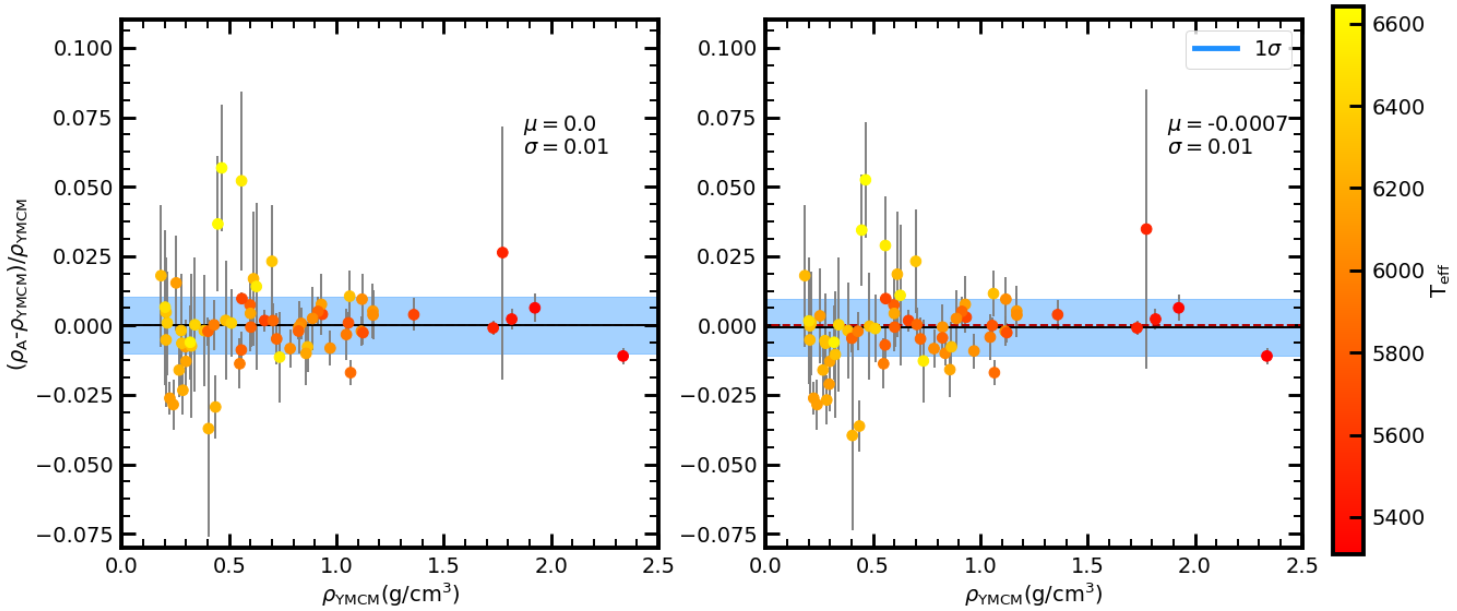

Figure 7.28: Relative density deviation (comparison of YMCM and Grid A results). The left panel presents the results considering $T_{\rm eff}$ and [Fe/H] as classical constraints only. Adding to these, luminosity is also considered as a constraint on the right panel.

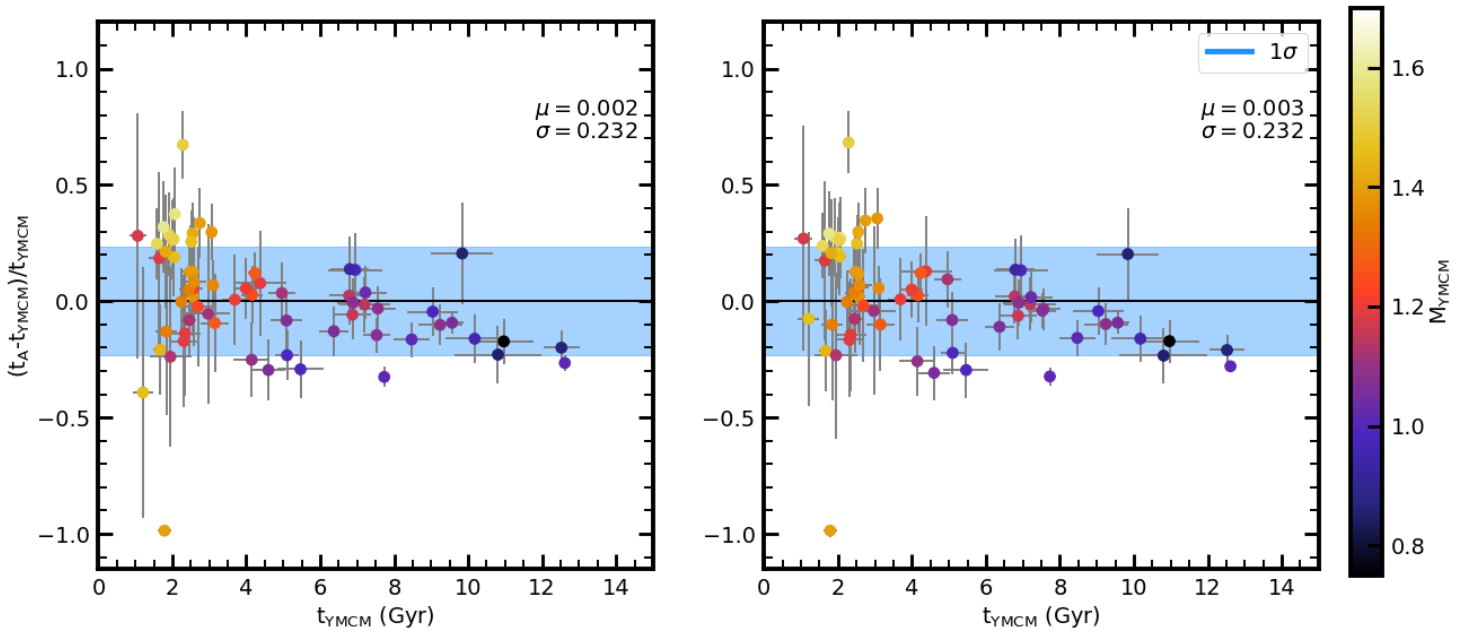

Figure 7.29: Relative age deviation (comparison of YMCM and Grid A results). The left panel presents the results considering $T_{\rm eff}$ and [Fe/H] as classical constraints only. Adding to these, luminosity is also considered as a constraint on the right panel.

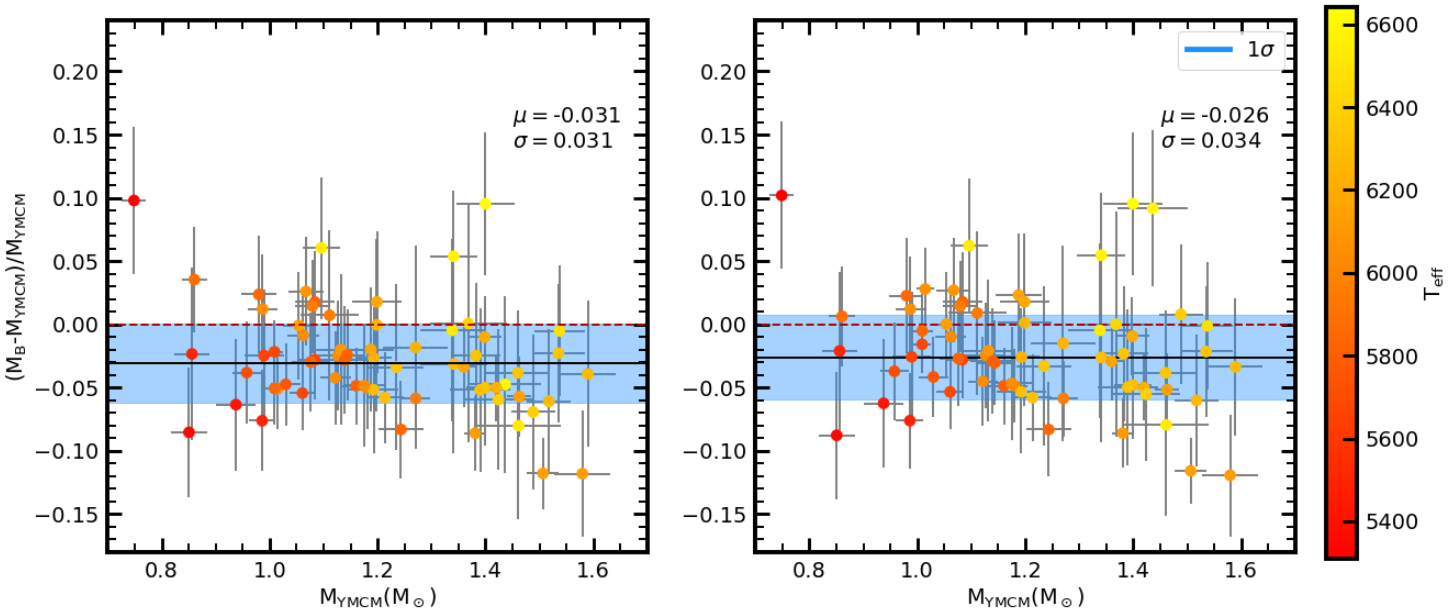

Figure 7.30: Relative mass deviation (comparison of YMCM and Grid B results). The left panel presents the results considering $T_{\rm eff}$ and [Fe/H] as classical constraints only. Adding to these, luminosity is also considered as a constraint on the right panel.

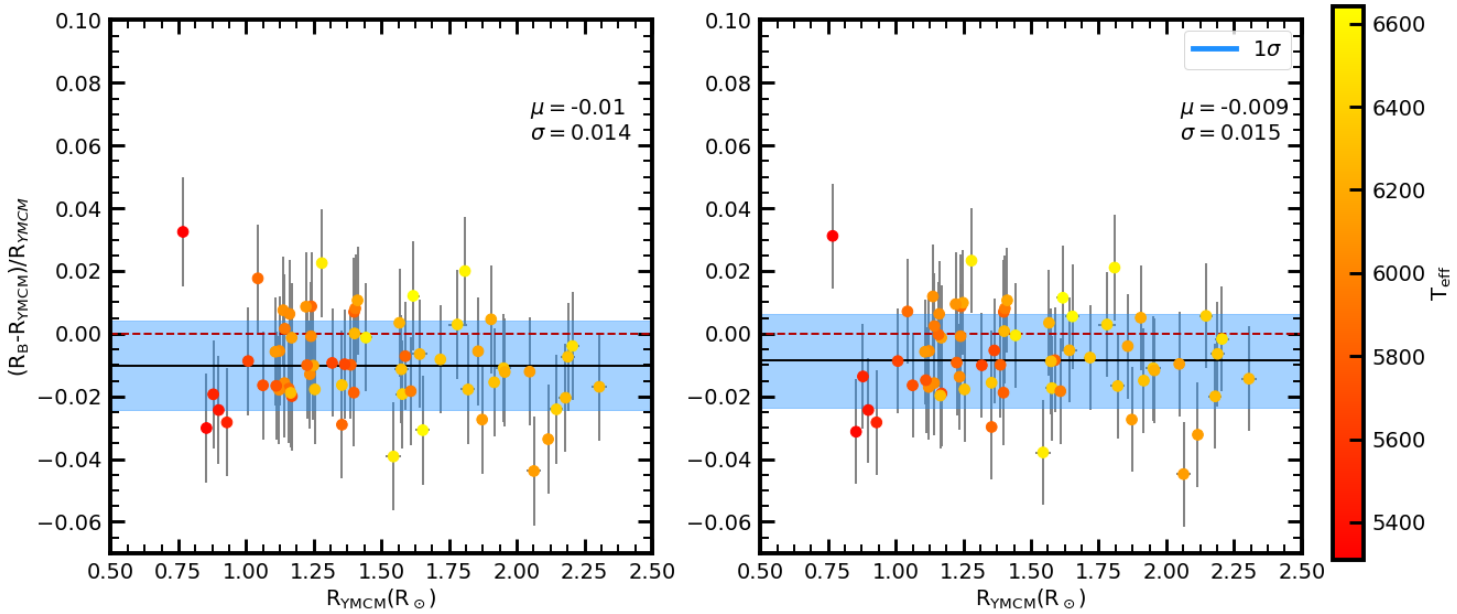

Figure 7.31: Relative radius deviation (comparison of YMCM and Grid B results). The left panel presents the results considering $T_{\rm eff}$ and [Fe/H] as classical constraints only. Adding to these, luminosity is also considered as a constraint on the right panel.

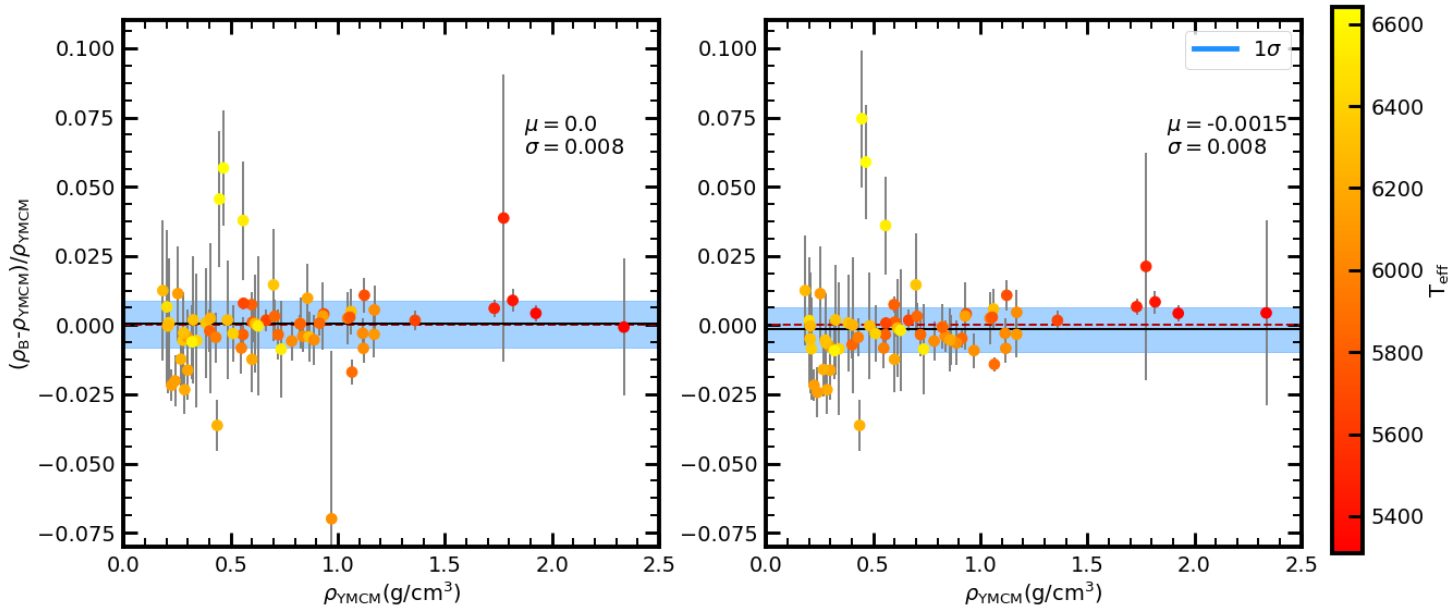

Figure 7.32: Relative density deviation (comparison of YMCM and Grid B results). The left panel presents the results considering $T_{\rm eff}$ and [Fe/H] as classical constraints only. Adding to these, luminosity is also considered as a constraint on the right panel.

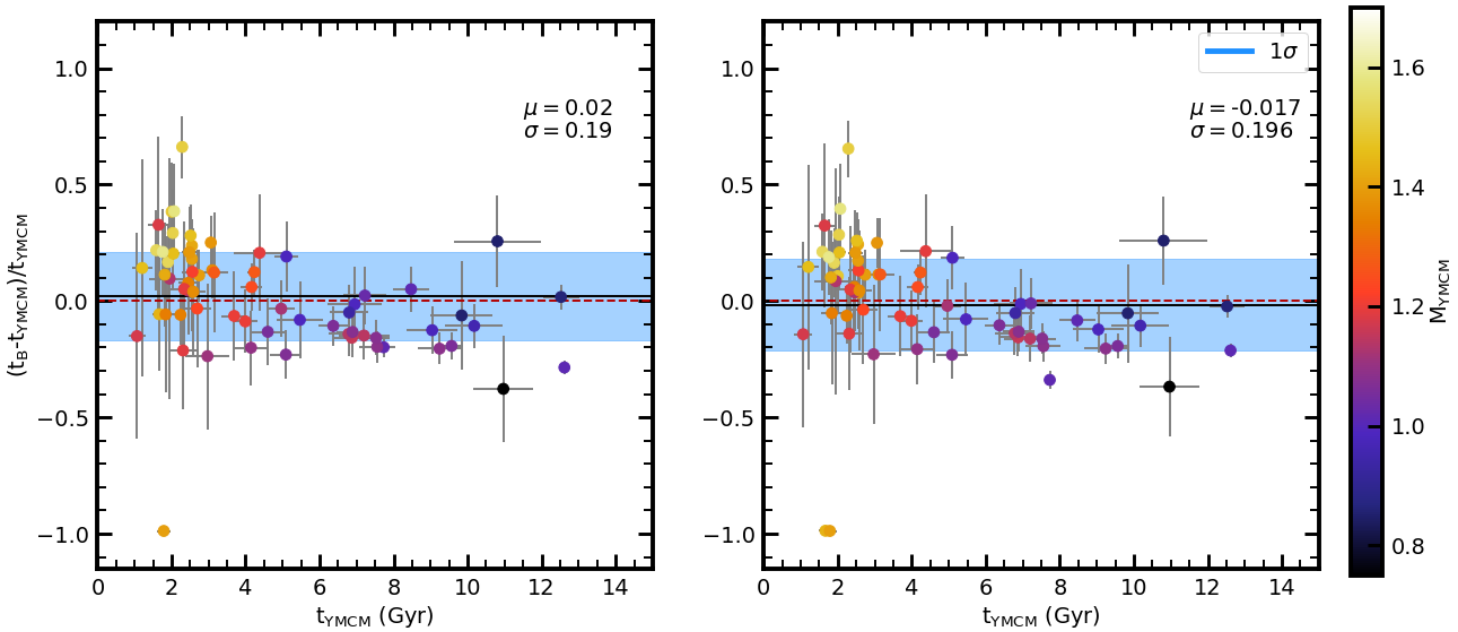

Figure 7.33: Relative age deviation (comparison of YMCM and Grid B results). The left panel presents the results considering $T_{\rm eff}$ and [Fe/H] as classical constraints only. Adding to these, luminosity is also considered as a constraint on the right panel.

7.3.3 Grid Comparison

We now compare the parameters derived from the two grids. Since using L_* as a constraint does not have a significant impact on the results, from now on we will only consider results obtained using L_* as an input.

In Fig. 7.34a we see the relative mass deviation between the two grids. We find a small negative bias, which indicates that Grid B masses are smaller than those from Grid A. This has been already explained in the previous section. For the radius (see Fig. 7.35a), we see a negative bias due to the same reason as for the mass.

Figure 7.36a refers to the density. Since the same individual frequency constraints are used irrespective of the grid, density values are very similar. As for the age (see Fig. 7.37a), we see a larger dispersion due to this parameter having a strong dependence on the stellar mass and chemical composition.

Looking at panel (b) in these figures, we see the histogram of the statistical uncertainties of the parameters of the reference grid that are obtained by statistical inference with AIMS. We see that this uncertainty is less than the dispersion (σ) obtained for the different parameters, which indicates that the variation of $\frac{\Delta Y}{\Delta Z}$ imposes a systematic effect on the stellar parameters. Comparing to the requirements of the PLATO mission [13], which has an accuracy requirement of 10% to 15% for the stellar mass, 2% to 4% for the stellar radius, and 10% for the stellar age, our bias and dispersion are well within these limits (see Table 7.3). However, for some individual stars, the impact of changing $\frac{\Delta Y}{\Delta Z}$ does approach the limits established by PLATO.

Table 7.3: Parameter relative deviations from grid comparison (μ =bias and σ =dispersion).

	μ	σ
Mass	-0.019	0.026
Radius	-0.006	0.011
Density	0.0	0.007
Age	-0.02	0.131

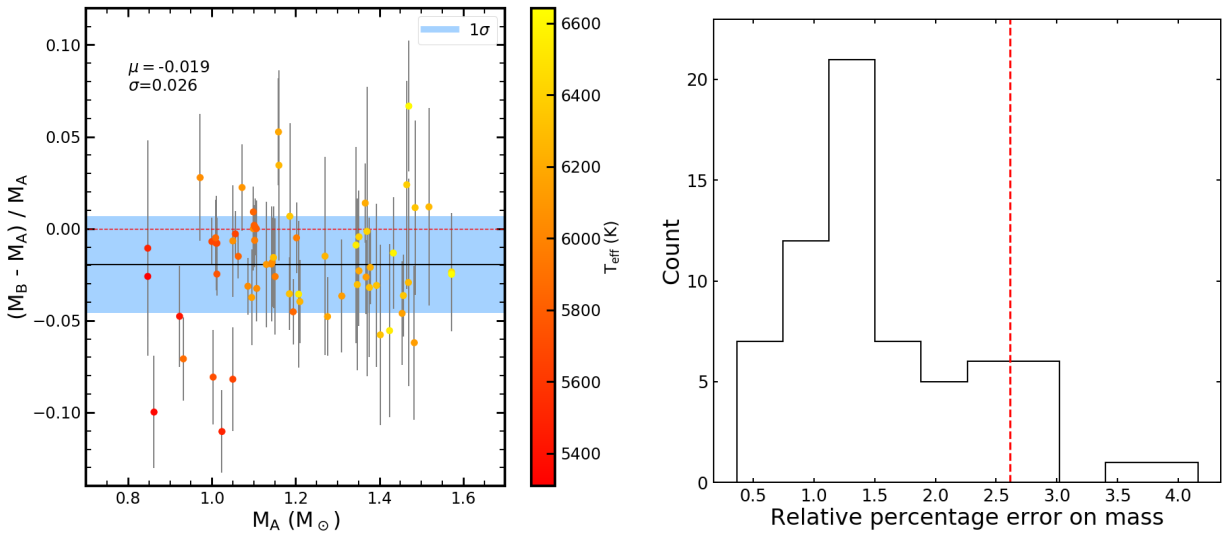

(a) (b)

Figure 7.34: (a) Relative mass deviation between Grids A and B; (b) Histogram of the statistical uncertainties for the mass in the reference grid, where the red line indicates the dispersion obtained between the two grids.

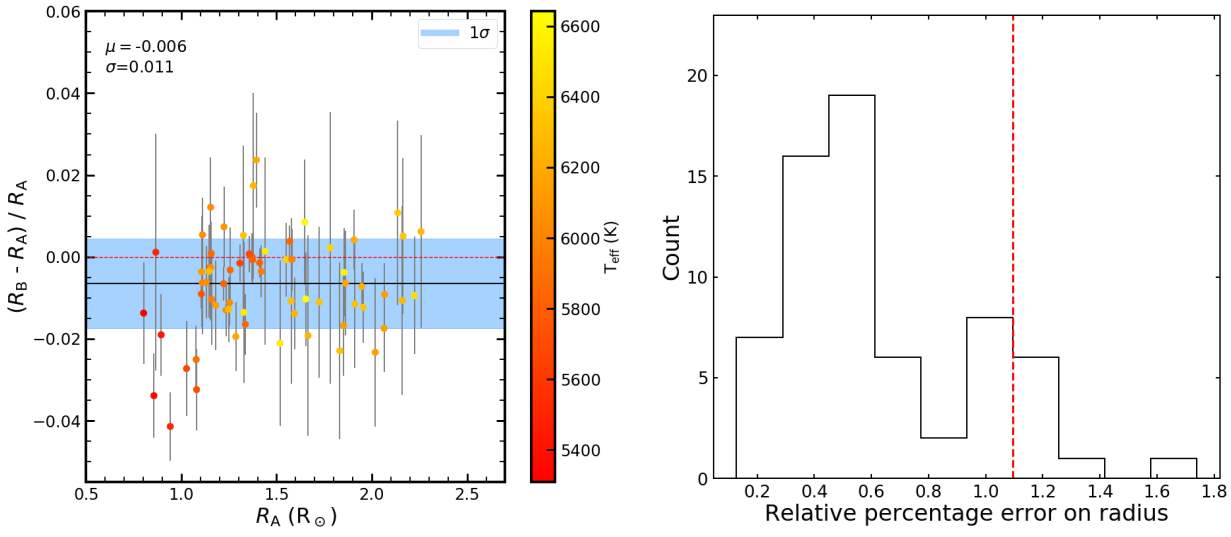

(a) (b)

Figure 7.35: (a) Relative radius deviation between Grids A and B; (b) Histogram of the statistical uncertainties for the radius in the reference grid, where the red line indicates the dispersion obtained between the two grids.

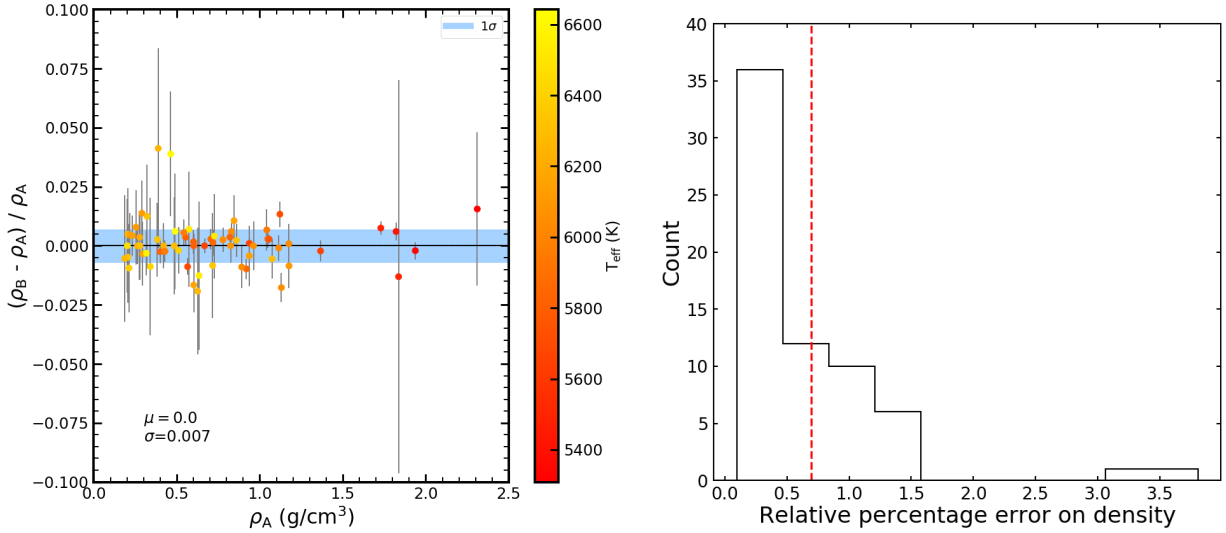

(a) (b)

Figure 7.36: (a) Relative density deviation between Grids A and B. (b) Histogram of the statistical uncertainties for the density in the reference grid, where the red line indicates the dispersion obtained between the two grids.

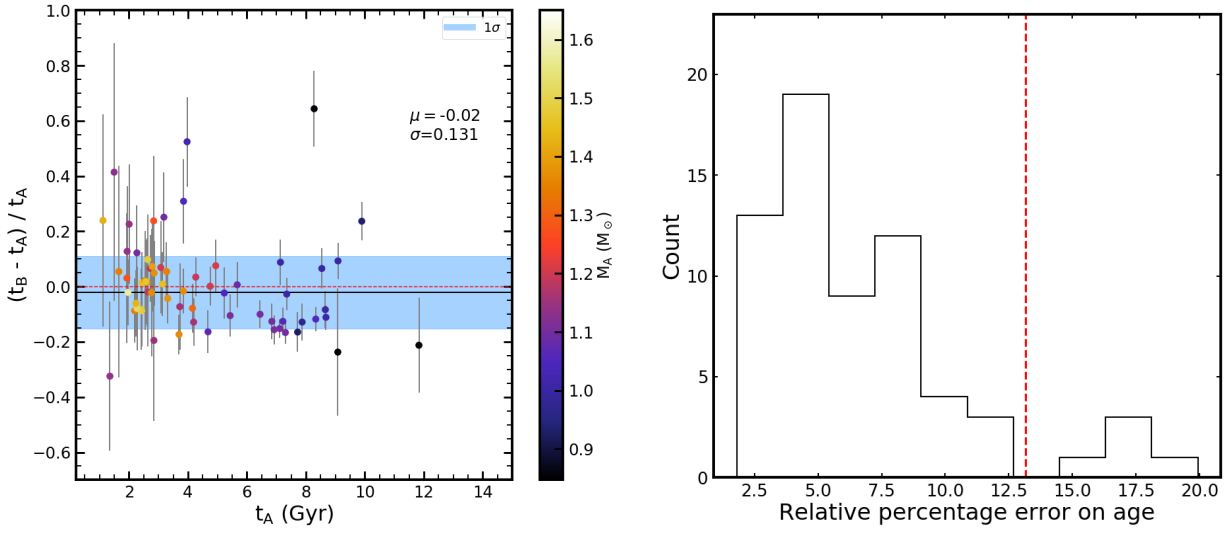

(a) (b)

Figure 7.37: (a) Relative age deviation between Grids A and B. (b) Histogram of the statistical uncertainties for the age in the reference grid, where the red line indicates the dispersion obtained between the two grids.

7.3.4 Models vs. Inference from Structural Glitches

Finally, we compare the values of the helium abundance at the surface with those derived through the observation of the glitch (i.e., short scale structural variation) associated to the helium second ionization zone [14]. The reference values were not obtained directly from the observation of glitches, but from a model calibration, using for that the MESA and GARSTEC stellar evolution codes. In both sets of models, the authors used similar physics, with the exception of diffusion, which was only included in MESA. In either case the helium fit is done in two ways: (i) one in which they directly fit the frequencies and (ii) the other using the second differences of the oscillation frequencies with respect to the radial order, $\delta^2\nu_{n,\ell} = \nu_{n-1,\ell} - 2\nu_{n,\ell} + \nu_{n+1,\ell}$. The authors show that the choice of method does not have a noticeable influence on the results. However, they only give results for 38 out of the 66 stars in the sample, since the other 28 stars have a low signal-to-noise ratio (S/N) in the observation of the glitch signature. Next, we compare the surface helium abundance computed with both our grids to the glitch-based values (both from MESA- and GARSTEC-calibrated models) for these 38 stars. We adopt the results coming from the first method of fitting the glitches as the reference. The glitch-based helium abundances from [14] are presented in Table A.12.

Starting with Grid A, we see that in the case of MESA (Fig. 7.38), where we include only stars with mass $\leq 1.15\mathrm{M}_\odot$ (which are the stars with diffusion in our models), there is a positive bias. This was to be expected, since we use $\frac{\Delta Y}{\Delta Z} = 1.4$, whereas the one obtained in reference [14] was $\frac{\Delta Y}{\Delta Z} = 1.226 \pm 0.849$. We also observe a clear trend, with Grid A values overestimating glitch-based values at low Y and vice versa at high Y. In the case of GARSTEC (Fig. 7.39), we include all 38 stars. We see that there is a larger bias (about ~ 0.02 larger), which is to be expected since diffusion is not included in the GARSTEC models. This leads to a smaller abundance of helium at the surface, making this systematic difference larger. Again, the same trend with Y can be seen.

Now for Grid B (Figs. 7.40 and 7.41), in both cases we observe a larger bias compared to the case of Grid A, which is to be expected due to the larger adopted value of $\frac{\Delta Y}{\Delta Z} = 2.0$. We continue to see a difference in the bias of ~ 0.02 between MESA and GARSTEC for the same reasons stated above. Furthermore, the trend observed for Grid A is again seen here. This trend is explained by the different physics used with respect to [14]. In [14] the authors define the initial abundance of helium (Y_i) as a free parameter, while we use a relationship that imposes the Y_i, keeping $\frac{\Delta Y}{\Delta Z}$ constant.

To study this possibility we used the results on the initial abundance of helium, Y_i, and on the initial metallicity, Z_i, provided by the lead author of [14], and by using eq. 2.19 we obtained an estimate of $\frac{\Delta Y}{\Delta Z}$ for each star. Showing these values in Fig. 7.42 as a function of Y_i, we see that these display a relationship indicating that stars with lower Y_i have a lower value of $\frac{\Delta Y}{\Delta Z}$. This same relationship

continues to appear when we plot results as function of $Y_{\rm s}$ instead. Such trend is reminiscent of the one obtained in Figs. 7.38 to 7.41, but with a positive slope. What we expect is that, when the value of $Y_{\rm s}$ from the glitches is lower than ours, $\frac{\Delta Y}{\Delta Z}$ will also be lower and vice versa. We find the reason as to why the trend appears when we compare the results, but now we want to know why it exists. It may be due to $\frac{\Delta Y}{\Delta Z}$ evolving over time or due to fluctuations in helium as a consequence of $Y_{\rm i}$ being a free parameter. We note that some of the estimated $\frac{\Delta Y}{\Delta Z}$ unexpectedly show negative values. These are due to the use of a constant helium primordial value, $Y_0 = 0.2484$, which may not be the corresponding value for the data set used. The values may thus present some inconsistencies, although this will not affect the observed trend.

We can expect $\frac{\Delta Y}{\Delta Z}$ to vary with time due to the chemical enrichment caused by supernova explosions. As we can see from Fig. 7.44, we do not find evidence that the above correlation is linked to this possibility. So it could come from the fluctuations that exist in the abundance of initial helium ($\delta Y_{\rm i}$). To calculate $\delta Y_{\rm i}$, we use eq. 2.19, so that:

$$\delta Y_{\rm i} = Y_{\rm i} - \left(\frac{\Delta Y}{\Delta Z}\right) Z_{\rm i} - Y_0, \tag{7.4}$$

where we use $\frac{\Delta Y}{\Delta Z} = 1.4$ and $Y_0 = 0.2484$ (these values introduce a bias, but will not change the result we are looking for). We find a strong positive correlation between $\delta Y_{\rm i}$ and $Y_{\rm i}$ (see Fig. 7.45) similar to that in Fig. 7.42. This could explain the trend. For the fluctuations to dominate, they have to be larger or of the same order of magnitude as the term $\left(\frac{\Delta Y}{\Delta Z}\right) Z_{\rm i}$. As $Z_{\rm i}$ has a range of values $\sim [0.01, 0.04]$ and $\frac{\Delta Y}{\Delta Z} = 1.4$, then $\left(\frac{\Delta Y}{\Delta Z}\right) Z_{\rm i}$ varies within the interval $[0.014, 0.056]$. Since $\delta Y_{\rm i}$ has values that are of the same order of magnitude as $\left(\frac{\Delta Y}{\Delta Z}\right) Z_{\rm i}$, the trend is dominated by fluctuations that exist in the initial helium.

Looking at $\delta Y_{\rm i}$ as a function of $Y_{\rm s}$ (Fig. 7.45), a comparison with Fig. 7.38 reveals that where the minimum fluctuation is we have the maximum difference and vice versa. We also see that the order of magnitude of the difference between the minimum and maximum values in Fig. 7.38 is similar to what we find for the difference that exists in the fluctuations.

Therefore, we conclude that there are fluctuations in the helium abundance that are significant when leaving $Y_{\rm i}$ as a free parameter. This way we can say that this trend appears because we impose a fixed value for $\frac{\Delta Y}{\Delta Z}$.

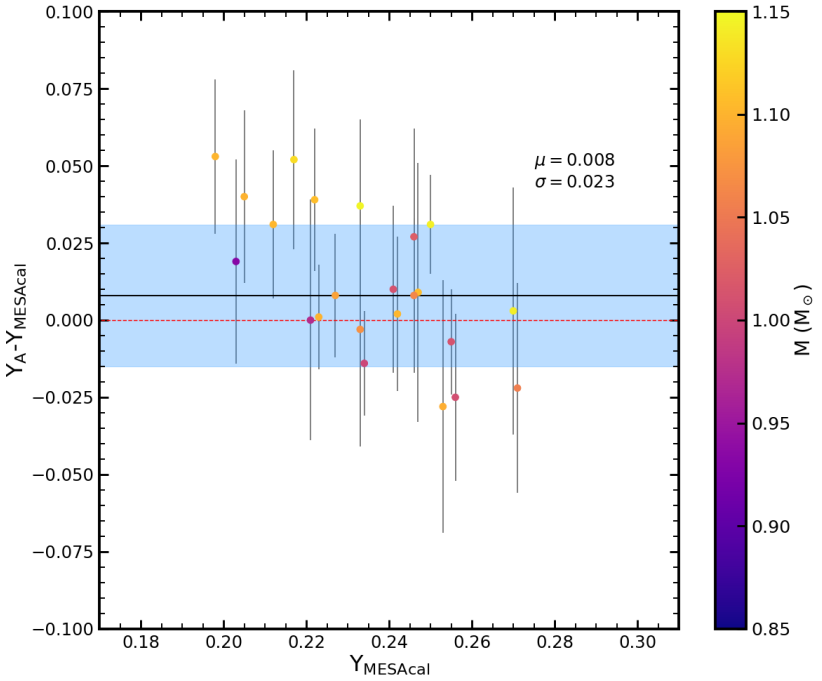

Figure 7.38: Comparison of the values obtained for the helium abundance at the surface from Grid A models with those obtained from a measurement of the glitches (calibrated with MESA models)

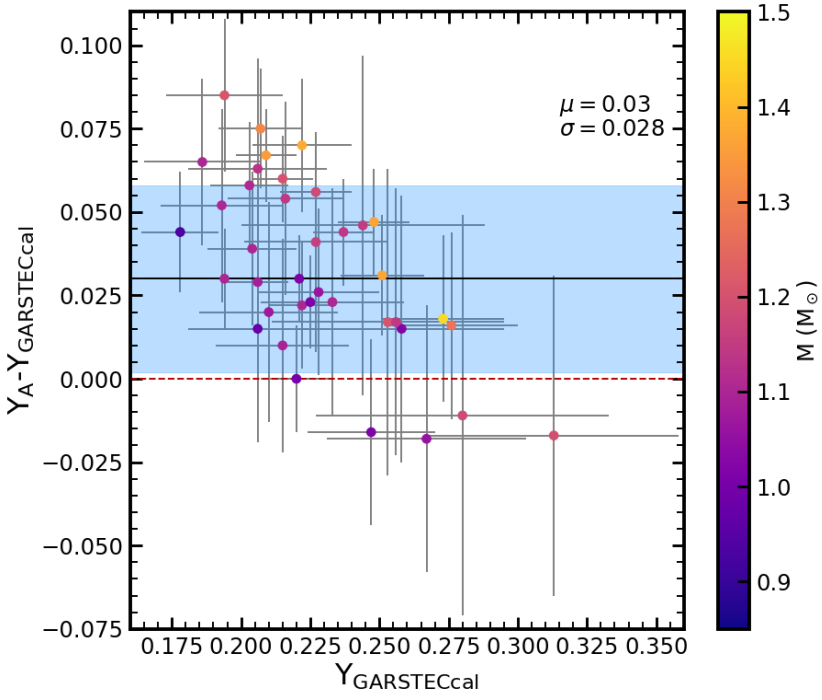

Figure 7.39: Comparison of the values obtained for the helium abundance at the surface from Grid A models with those obtained from a measurement of the glitches (calibrated with GARSTEC models)

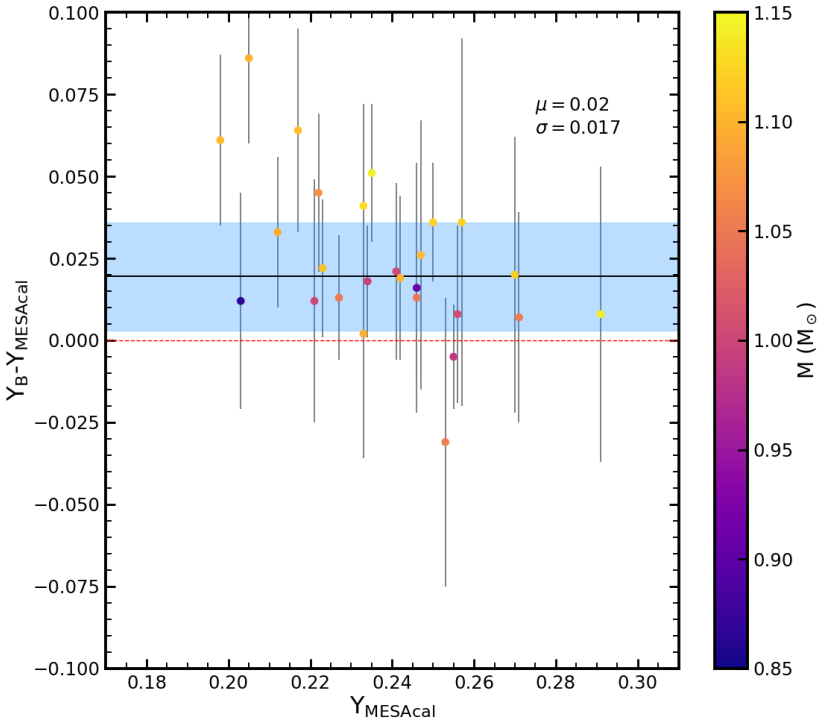

Figure 7.40: Comparison of the values obtained for the helium abundance at the surface from Grid B models with those obtained from a measurement of the glitches (calibrated with MESA models)

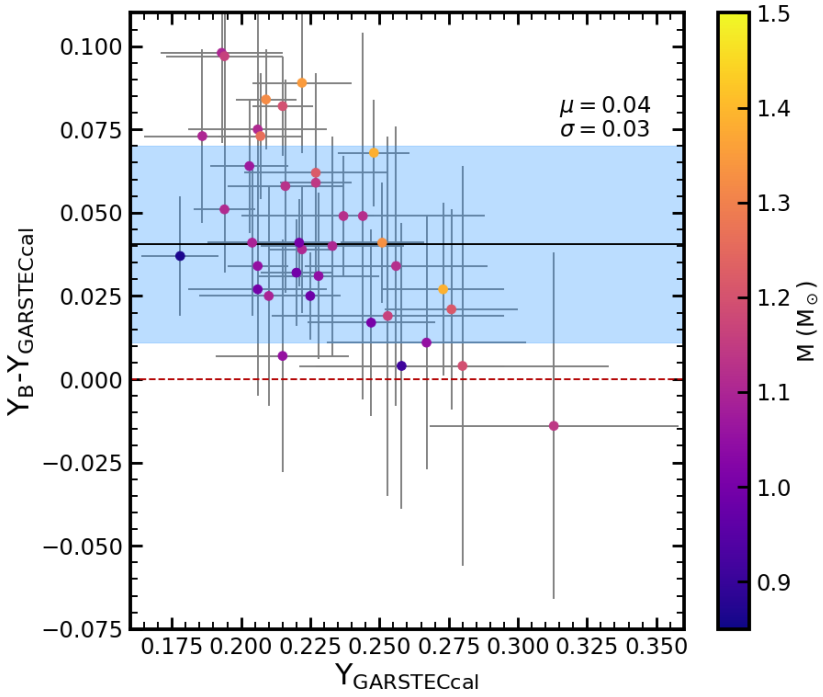

Figure 7.41: Comparison of the values obtained for the helium abundance at the surface from Grid B models with those obtained from a measurement of the glitches (calibrated with GARSTEC models)

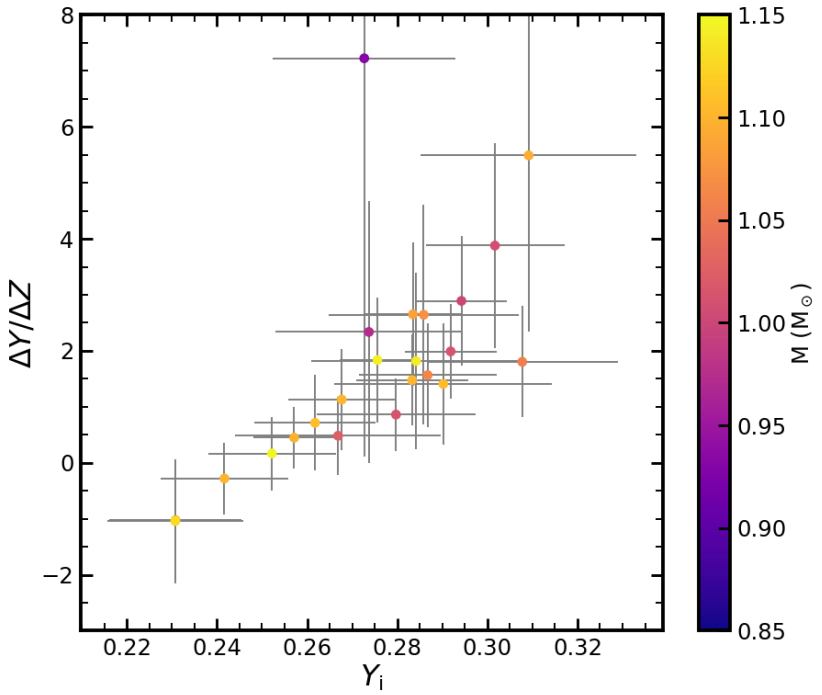

Figure 7.42: Estimated value of $\frac{\Delta Y}{\Delta Z}$ for each star as a function of Y_i.

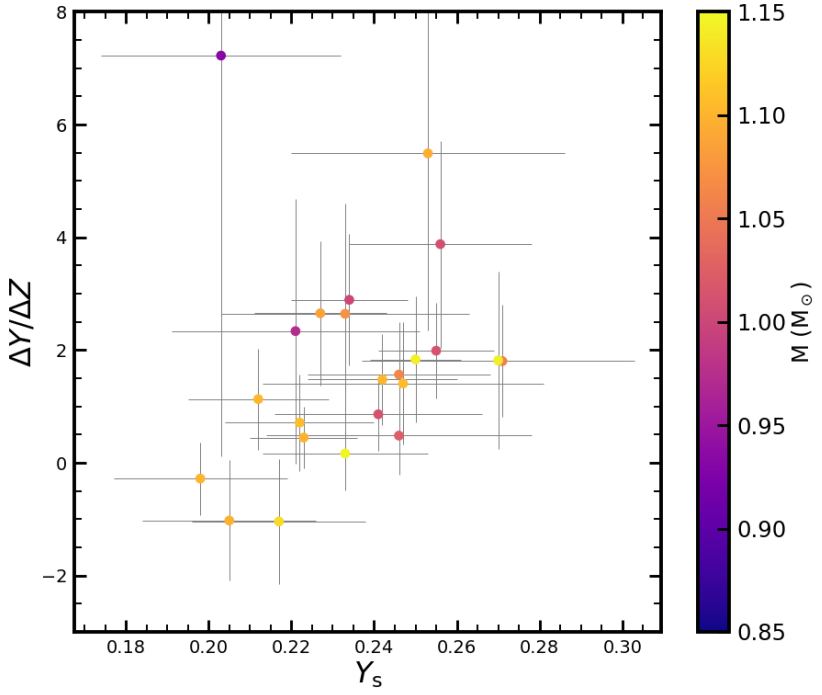

Figure 7.43: Estimated value of $\frac{\Delta Y}{\Delta Z}$ for each star as a function of Y_s.

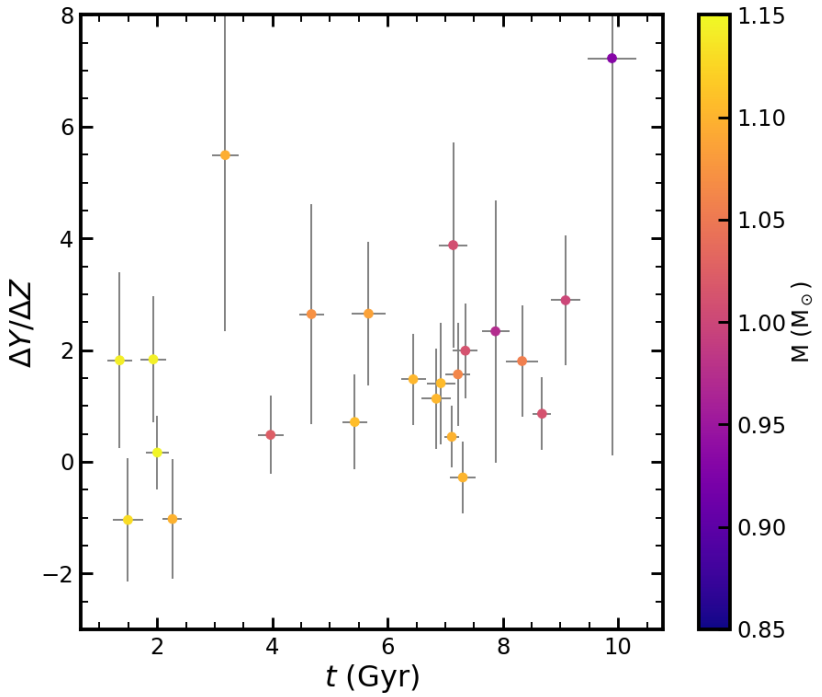

Figure 7.44: Estimated $\frac{\Delta Y}{\Delta Z}$ as a function of stellar age.

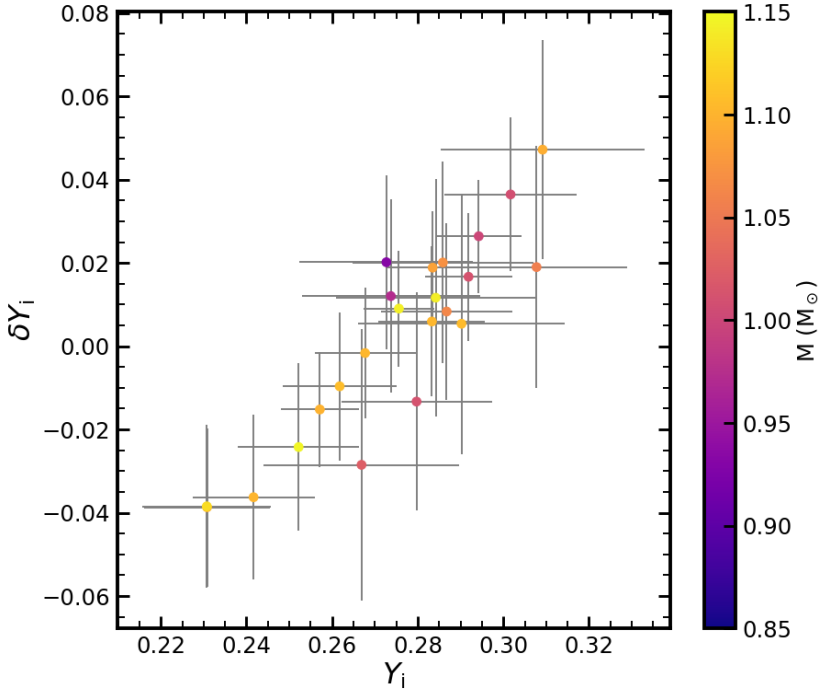

Figure 7.45: $\delta Y_{\rm i}$ as a function of $Y_{\rm i}$.

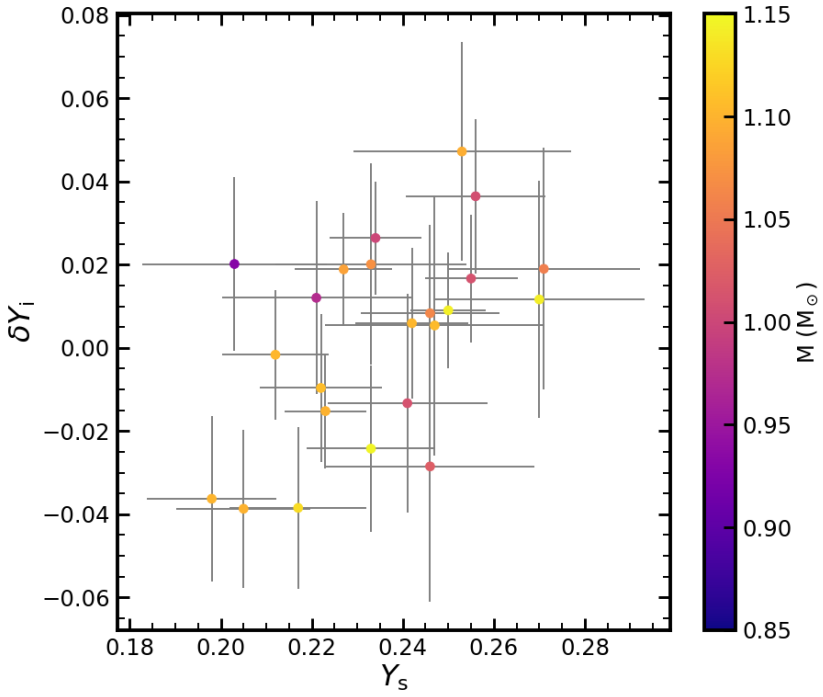

Figure 7.46: δY_i a function of Y_s.

8 Summary

With the three codes presented in our work we were able to model stars. With MESA and GYRE, we were able to build model grids and obtain theoretical frequency values, which were optimized by AIMS to obtain stellar parameters. With these codes, we modeled the Sun obtaining reasonable results for its parameters, and verifying that the use of different physics affects the obtained parameters.

Afterwards, we used two grids to get the stellar parameters of 66 stars from the *Kepler* LEGACY sample. We performed two tests, one considering the luminosity as a constraint, and another without including it, and we observed that it does not have a significant impact on the results. Comparing the results with the literature, we obtained consistent values.

Between the two grids used (Grid A and B), we obtained that the higher the value of $\frac{\Delta Y}{\Delta Z}$, the lower the estimates for mass and radius will be, having respectively a relative bias (with Grid A as reference) of $\mu = -0.019$ and $\mu = -0.011$. However, density is not expected to change due to the use of the same individual frequency constraint. The statistical uncertainties of the stellar parameters obtained with Grid A (used as reference) are smaller than the systematics, which take values for the mass of 2.6%, for radius of 1.1%, for density of 0.7%, and for the stellar age of 13.1%, showing a systematic contribution caused by the variation of $\frac{\Delta Y}{\Delta Z}$. Also, notice that the bias and dispersion estimated for the mass and the radius are within the requirements of 10-15% and 2-4%, respectively, of the future PLATO mission. Nevertheless, for some particular stars, the effect of changing $\frac{\Delta Y}{\Delta Z}$ may be a matter of concern.

When comparing the helium values obtained from our models with those obtained using the glitch analysis in [14], we found an abundance of helium greater than the one from the reference [14]. This was expected since we used in both our grids a larger $\frac{\Delta Y}{\Delta Z}$ than the one those authors obtained. From our results, it became clear that the lower the value obtained for helium from glitches, the larger the abundance of helium at the surface determined in the stars by our models.This might be due to the constraint on the abundance of helium in our models caused by the helium enrichment law, which, in the case of the glitches, is not used.

In the end, we can say that the value of $\frac{\Delta Y}{\Delta Z}$ does impact the stellar parameters obtained. Depending on the variation of the chemical transport processes in stellar models, it may alter the values of the uncertainties obtained and thus exceed the limits required by the PLATO mission. This way, it would be interesting in a future work to build a grid where $\frac{\Delta Y}{\Delta Z}$ is a free parameter, and at the same time varying the chemical transport process in the stellar models, in order to study the systematic effects, of the two effects combined would cause on the derived stellar parameters.

References

[1] Aguirre V.S. (2018) *Stellar Evolution and Modelling Stars.* In: Campante T., Santos N., Monteiro M. (eds) Asteroseismology and Exoplanets: Listening to the Stars and Searching for New Worlds. Astrophysics and Space Science Proceedings, vol 49. Springer, Cham

[2] William J. Chaplin and Andrea Miglio, (2013), *Asteroseismology of Solar-Type and Red-Giant Stars*, Annual Review of Astronomy and Astrophysics vol 51, 353-392

[3] Cunha M.S. (2018) *Theory of Stellar Oscillations.* In: Campante T., Santos N., Monteiro M. (eds) Asteroseismology and Exoplanets: Listening to the Stars and Searching for New Worlds. Astrophysics and Space Science Proceedings, vol 49. Springer, Cham

[4] Bill Paxton, Lars Bildsten, Aaron Dotter, Falk Herwig, Pierre Lesaffre, and Frank Timmes, (2011), *Modules For Experiments In Stellar Astrophysics (MESA)*, The Astrophysical Journal Supplement Series, vol 192, 1

[5] R. H. D. Townsend, (2013), *GYRE: an open-source stellar oscillation code based on a new Magnus Multiple Shooting scheme*, Monthly Notices of the Royal Astronomical Society , vol 435, 4, 3406-3418

[6] Ben M. Rendle, Gaël Buldgen, Andrea Miglio, Daniel Reese,Arlette Noels, Guy R. Davies, Tiago L. Campante, William J. Chaplin,Mikkel N. Lund, James S. Kuszlewicz, Laura J. A. Scott, Richard Scuflaire,Warrick H. Ball, Jiri Smetana, Benard Nsamba, (2019), *AIMS - A new tool for stellar parameter determinations using asteroseismic constraints*, Monthly Notices of the Royal Astronomical Society, vol 484, 771-786

[7] M. Gennaro, P. G. Prada Moroni, and S. Degl'Innocenti, (2010), $\Delta Y/\Delta Z$ *from the analysis of local K dwarfs*, Astronomy & Astrophysics, vol 518

[8] Raul Jimenez, Chris Flynn, James MacDonald, Brad K. Gibso (2003) *Cosmic Production of Helium* Science, vol 299, 1552-1555

[9] Luca Casagrande, Chris Flynn, Laura Portinari, Leo Girardi, Raul Jimene, (2007), *The helium abundance and* $\Delta Y/\Delta Z$ *in lower main-sequence stars* , MNRAS, vol 382, 1516-1540

[10] Dana S. Balser (2006), *The Chemical Evolution of Helium*, The Astronomical Journal, vol 132, 2326-2332

[11] Aldo M. Serenelli, Sarbani Basu, *Determining the initial helium abundance of the Sun*, ApJ, vol 719, 865-872

[12] William J. Borucki, (2016), *KEPLER* Mission: development and overview, Reports on Progress in Physics, vol 79

[13] H. Rauer, C. Aerts, J. Cabrera, and PLATO Team, (2016), The PLATO 2.0 mission, Astronomische Nachrichten, vol 337, 961

[14] Kuldeep Verma, Keyuri Raodeo, Sarbani Basu, Víctor Silva Aguirre, Anwesh Mazumdar, Jakob Rørsted Mosumgaard, Mikkel N Lund, Pritesh Ranadive , (2019), *Helium abundance in a sample of cool stars: measurements from asteroseismology*, Monthly Notices of the Royal Astronomical Society, vol 483, 4, 4678-4694

[15] Cyburt, Richard H.; Fields, Brian D.; Olive, Keith A., (2003), *Primordial nucleosynthesis in light of WMAP* Physics Letters B, vol 567, 3-4, 227-234

[16] Mikkel N. Lund, Víctor Silva Aguirre, Guy R. Davies, William J. Chaplin, Jørgen Christensen-Dalsgaard, Günter Houdek, Timothy R. White, Timothy R. Bedding, Warrick H. Ball, Daniel Huber, (2017), *Standing on the Shoulders of Dwarfs: the Kepler Asteroseismic LEGACY Sample. I. Oscillation Mode Parameters*, The Astrophysical Journal, vol 835, 2

[17] F. P. Pijpers, (2003), *Selection Criteria For Targets Of Asteroseismic Campaigns*, Astronomy & Astrophysics, vol 400, 1, 241-248

[18] Hekker S. (2018) *Asteroseismology of Red Giants and Galactic Archaeology.* In: Campante T., Santos N., Monteiro M. (eds) Asteroseismology and Exoplanets: Listening to the Stars and Searching for New Worlds. Astrophysics and Space Science Proceedings, vol 49. Springer, Cham

[19] Aaron Dotter, Charlie Conroy, Phillip Cargile, and Martin Asplund (2017), *The Influence Of Atomic Diffusion On Stellar Ages And Chemical Tagging*, The Astrophysical Journal, Volume 840, Number 2

[20] S. Turcotte, J. Richer, G. Michaud, C. A. Iglesias, and F. J. Rogers, (1998), *Consistent Solar Evolution Model Including Diffusion And Radiative Acceleration Effects*, The Astrophysical Journal, vol 504, 1

[21] Christensen-Dalsgaard, (2008), in IAU Symposium, vol. 252, The Art of Modeling Stars in the 21st Century, ed. L. Deng & K. L. Chan, 135-147

[22] Naoki Itoh, Hiroshi Hayashi, Akinori Nishikawa, Yasuharu Kohyama ,(1996), *Neutrino Energy Loss in Stellar Interiors. VII. Pair, Photo-, Plasma, Bremsstrahlung, and Recombination Neutrino Processes*, Astrophysical Journal Supplement vol 102, 411

[23] Anne A. Thoul, John N. Bahcall and Abraham Loeb, (1994), *Element Diffusion in the Solar Interior*, Astrophysical Journal, vol421, 828

[24] Icko Iben, and Jim MacDonald,(1985), *The effects of diffusion due to gravity and due to composition gradients on the rate of hydrogen burning in a cooling degenerate dwarf. I - The case of a thick helium buffer layer*, Astrophysical Journal, vol 296, 540-553.

[25] Mikkel N. Lund, Daniel R. Reese, *Tutorial: Asteroseismic Stellar Modelling with AIMS.* In: Campante T., Santos N., Monteiro M. (eds) Asteroseismology and Exoplanets: Listening to the Stars and Searching for New Worlds. Astrophysics and Space Science Proceedings, vol 49. Springer, Cham

[26] Aguirre V.S., Mikkel N. Lund, H. M. Antia, Warrick H. Ball, Sarbani Basu, Jørgen Christensen-Dalsgaard, Yveline Lebreton, Daniel R. Reese, Kuldeep Verma, Luca Casagrande, (2017), *Standing on the Shoulders of Dwarfs: the Kepler Asteroseismic LEGACY Sample.II. Radii, Masses, and Ages*, The Astrophysical Journal, vol 835, 2

[27] Warrick H. Ball, L. Gizon, (2014), *A new correction of stellar oscillation frequencies for near-surface effects*, Astronomy & Astrophysics vol 568, A123

[28] B Nsamba, T L Campante, M J P F G Monteiro, M S Cunha, B M Rendle, D R Reese, K Verma,(2018), *Asteroseismic modelling of solar-type stars: internal systematics from input physics and surface correction methods*, Monthly Notices of the Royal Astronomical Society, vol 477, 4, 5052-5063

[29] Z. Magic, A. Weiss and M. Asplund, (2014), The Stagger-grid: A grid of 3D stellar atmosphere models III. The relation to mixing-length convection theory Astronomy & Astrophysics, vol 573, A89

[30] B. Nsamba, N. Moedas, (2009 preprint), *In-depth exploration of the treatment of initial helium abundance in asteroseismic stellar modelling*

[31] Kunz R., Fey M., (2002), *Astrophysical Reaction Rate of* $^{1}2C(\alpha,\gamma)^{1}6O$, The Astrophysical Journal , vol 567, 643-650

[32] G. Imbriani, H. Costantini, (2005), *S-factor of* $^{1}4N(p,\gamma)^{1}5O$ *at astrophysical energies*, The European Physical Journal A, vol 25, 455-466

[33] Iglesias C. A.; Rogers F. J., (1996) *Updated Opal Opacities* , The Astrophysical Journal, vol 567, 943

[34] Ferguson J. W., Alexander D. R., (2005), *Low-Temperature Opacities* , The Astrophysical Journal, vol 623, 585-596

[35] Rogers F. J., Nayfonov A.(2002), *Updated and Expanded OPAL Equation-of-State Tables: Implications for Helioseismology* , The Astrophysical Journal, vol 576, 1064-1074

[36] Grevesse N., Sauval A. J. (1998), *Standard Solar Composition* , Space Science Reviews, vol 85, 161-174

[37] Herwig F., (2000), *The evolution of AGB stars with convective overshoot* , Astronomy and Astrophysics, vo 360, 952-968

[38] Travis A. Berger, Daniel Huber, Eric Gaidos, and Jennifer L. van Saders, (2018), *Revised Radii of Kepler Stars and Planets Using Gaia Data Release 2*, The Astrophysical Journal, vol 866, 2

[39] T. S. Metcalfe, W. J. Chaplin, T. Appourchaux, R. A. García, S. Basu, I. Brandão, O. L. Creevey, S. Deheuvels, G. Doğan, P. Eggenberger (2012), *Asteroseismology Of The Solar Analogs 16 Cyg A And B From Kepler Observations*, The Astrophysical Journal Letters, vol 748, 1

[40] Savita Mathur, Daniel Huber, Natalie M. Batalha, David R. Ciardi, Fabienne A. Bastien, Allyson Bieryla, (2017), *Revised Stellar Properties Of Kepler Targets For The Q1-17 (DR25) Transit Detection Run*, The Astrophysical Journal Supplement Series, vol 229, 2

[41] Guillermo Torres, (2010), On The Use Of Empirical Bolometric Corrections For Stars, The Astronomical Journal, vol 140, 5

[42] Sara Crandall, Bharat Ratra, (2014), *Median statistics cosmological parameter values*, Physics Letters B, vol 732, 330-334

A Appendix

Stellar Inputs

Table A.1: Classical parameters of stars in the LEGACY sample, plus the Sun, used as constraints.

KIC	$T_{\rm eff}$(K)	$\Delta T_{\rm eff}$(K)	[Fe/H]	Δ[Fe/H]	$L(\mathrm{L}_\odot)$	$\Delta L(\mathrm{L}_\odot)$
1435467	6326.0	127.0	0.01	0.15	4.143	0.68
2837475	6614.0	132.0	0.01	0.15	4.669	0.775
3427720	6045.0	121.0	-0.06	0.15	1.544	0.252
3456181	6384.0	128.0	-0.15	0.15	6.991	1.162
3632418	6202.0	124.0	-0.12	0.15	5.04	0.823
3656476	5668.0	113.0	0.25	0.15	1.624	0.265
3735871	6107.0	122.0	-0.04	0.15	1.485	0.244
4914923	5805.0	116.0	0.08	0.15	2.1	0.352
5184732	5846.0	117.0	0.36	0.15	1.897	0.31
5773345	6130.0	123.0	0.21	0.09	5.354	0.878
5950854	5853.0	117.0	-0.23	0.15	1.767	0.292
6106415	6037.0	121.0	-0.04	0.15	1.89	0.311
6116048	6033.0	121.0	-0.23	0.15	1.876	0.306
6225718	6313.0	126.0	-0.07	0.15	2.281	0.374
6508366	6331.0	127.0	-0.05	0.15	6.793	1.122
6603624	5674.0	113.0	0.28	0.15	1.243	0.205
6679371	6479.0	130.0	0.01	0.15	8.212	1.367
6933899	5832.0	117.0	-0.01	0.15	2.993	0.494
7103006	6344.0	127.0	0.02	0.15	5.575	0.914
7106245	6068.0	212.0	-0.99	0.30	1.668	0.479
7206837	6305.0	126.0	0.10	0.15	3.785	0.618
7296438	5808.0	116.0	0.19	0.15	2.026	0.329
7510397	6171.0	123.0	-0.21	0.15	6.986	1.143
7680114	5811.0	116.0	0.05	0.15	2.111	0.342
7771282	6248.0	125.0	-0.02	0.15	3.919	0.643
7871531	5501.0	80.0	-0.26	0.15	0.661	0.066
7940546	6235.0	125.0	-0.20	0.15	5.303	0.871
7970740	5309.0	106.0	-0.54	0.15	0.454	0.074
8006161	5488.0	110.0	0.34	0.15	0.699	0.115

Table A.1 continued						
8150065	6265.0	219.0	-0.20	0.30	2.949	0.849
8179536	6343.0	127.0	-0.03	0.15	2.772	0.455
8228742	6122.0	122.0	-0.08	0.15	4.352	0.718
8379927	6034.0	211.0	-0.20	0.30	2.333	0.67
8394589	6143.0	123.0	-0.29	0.15	1.978	0.324
8424992	5719.0	114.0	-0.12	0.15	1.109	0.181
8694723	6246.0	125.0	-0.42	0.15	3.361	0.548
8760414	5873.0	117.0	-0.92	0.15	1.204	0.196
8938364	5677.0	114.0	-0.13	0.15	1.725	0.283
9025370	5659.0	198.0	-0.20	0.30	1.485	0.43
9098294	5852.0	117.0	-0.18	0.15	1.458	0.238
9139151	6302.0	126.0	0.10	0.15	1.852	0.304
9139163	6400.0	128.0	0.15	0.09	3.719	0.606
9206432	6538.0	131.0	0.16	0.15	3.831	0.628
9353712	6278.0	126.0	-0.05	0.15	6.697	1.113
9410862	6047.0	121.0	-0.31	0.15	1.731	0.283
9414417	6318.0	126.0	-0.13	0.101	5.322	0.867
9812850	6321.0	126.0	-0.07	0.15	4.591	0.751
9955598	5416.0	108.0	0.05	0.15	0.625	0.103
9965715	6542.0	131.0	-0.22	0.15	3.284	0.538
10068307	6132.0	123.0	-0.23	0.15	5.272	0.874
10079226	5949.0	119.0	0.11	0.15	1.611	0.264
10162436	6146.0	123.0	-0.16	0.15	5.415	0.887
10454113	6177.0	80.0	-0.07	0.15	2.612	0.105
10516096	5964.0	119.0	-0.11	0.15	2.375	0.39
10644253	6045.0	121.0	0.06	0.15	1.571	0.26
10730618	6423.0	225.0	-0.172	0.30	4.774	1.372
10963065	6089.0	122.0	-0.19	0.15	1.943	0.317
11081729	6548.0	131.0	0.11	0.15	3.291	0.539
11253226	6642.0	133.0	-0.08	0.15	4.571	0.751
11772920	5341.0	107.0	-0.10	0.15	0.538	0.088
12009504	6179.0	124.0	-0.08	0.15	2.775	0.459

Table A.1 continued						
12069127	6276.0	126.0	0.08	0.15	7.953	1.312
12069424	5825.0	50.0	0.096	0.026	1.56	0.05
12069449	5750.0	50.0	0.052	0.021	1.27	0.04
12258514	5964.0	119.0	-0.00	0.15	3.023	0.494
12317678	6580.0	132.0	-0.28	0.15	6.042	1.015
Sun	5772.0	65.0	0.0	0.05	1.0	0.03

Table A.2: Bolometric correction coefficients.

Coefficient	$\log(T_{\rm eff}(\rm K)) < 3.70$	$3.70 < \log(T_{\rm eff}(\rm K)) < 3.90$	$\log(T_{\rm eff}(\rm K)) > 3.90$
a	-0.190537291496456E+05	-0.370510203809015E+05	-0.118115450538963E+06
b	0.155144866764412E+05	0.385672629965804E+05	0.137145973583929E+06
c	-0.421278819301717E+04	-0.150651486316025E+05	-0.636233812100225E+05
d	0.381476328422343E+03	0.261724637119416E+04	0.147412923562646E+05
e	...	-0.170623810323864E+03	-0.170587278406872E+04
f	...	...	0.788731721804990E+02

Stellar Results

Table A.3: Derived mass, radius, age, and density for Grid A without L_*.

KIC	M_* ($\rm M_\odot$)	R_* ($\rm R_\odot$)	Age (Myr)	$\bar{\rho}$ (g cm^{-3})
1435467	1.393±0.038	1.724±0.019	2.6073±0.2384	0.383±0.004
2837475	1.464±0.038	1.644±0.018	1.3202±0.1669	0.464±0.007
3427720	1.097±0.017	1.11±0.007	2.2532±0.1823	1.13±0.006
3456181	1.438±0.045	2.12±0.027	2.5298±0.2031	0.212±0.002
3632418	1.368±0.021	1.908±0.011	3.6667±0.2056	0.278±0.001
3656476	1.057±0.01	1.307±0.005	8.3004±0.2799	0.667±0.001
3735871	1.133±0.024	1.107±0.009	1.4819±0.3187	1.176±0.007
4914923	1.103±0.011	1.372±0.005	6.4768±0.2472	0.602±0.002
5184732	1.192±0.016	1.335±0.007	4.2743±0.2191	0.706±0.002
5773345	1.431±0.037	1.988±0.021	2.8431±0.2389	0.257±0.002
5950854	1.011±0.017	1.256±0.008	8.6363±0.2954	0.718±0.003
6106415	1.077±0.014	1.219±0.006	5.1368±0.2884	0.837±0.002
6116048	1.089±0.012	1.254±0.004	5.5482±0.3344	0.778±0.002
6225718	1.185±0.017	1.248±0.007	2.7032±0.2196	0.859±0.003
6508366	1.478±0.043	2.159±0.025	2.4474±0.1976	0.207±0.002
6603624	1.013±0.006	1.15±0.002	8.6803±0.1699	0.938±0.001

Table A.3 continued				
6679371	1.566±0.025	2.217±0.017	1.9771±0.1187	0.203±0.003
6933899	1.099±0.006	1.569±0.003	7.0958±0.1681	0.401±0.001
7103006	1.455±0.019	1.951±0.01	2.4337±0.156	0.276±0.003
7106245	1.051±0.018	1.154±0.008	5.2141±0.2885	0.963±0.005
7206837	1.34±0.039	1.573±0.02	2.5664±0.2689	0.485±0.006
7296438	1.106±0.012	1.374±0.006	6.9453±0.2762	0.601±0.002
7510397	1.347±0.024	1.859±0.014	3.3119±0.1769	0.295±0.002
7680114	1.101±0.008	1.411±0.004	7.3223±0.2466	0.552±0.001
7771282	1.27±0.035	1.663±0.023	2.8539±0.3174	0.389±0.012
7871531	0.844±0.031	0.868±0.013	11.8604±1.162	1.821±0.077
7940546	1.379±0.017	1.946±0.007	3.295±0.1867	0.263±0.001
7970740	0.847±0.011	0.802±0.003	9.0716±0.3994	2.31±0.002
8006161	1.028±0.013	0.943±0.004	3.9169±0.2912	1.729±0.002
8150065	1.162±0.033	1.379±0.019	3.7153±0.3645	0.624±0.011
8179536	1.186±0.034	1.326±0.016	2.6284±0.3145	0.716±0.009
8228742	1.269±0.026	1.824±0.016	3.9702±0.2048	0.294±0.002
8379927	1.143±0.018	1.131±0.006	1.9518±0.2728	1.114±0.003
8394589	1.091±0.016	1.18±0.007	3.2385±0.2907	0.937±0.006
8424992	1.004±0.018	1.08±0.007	8.5374±0.4212	1.121±0.003
8694723	1.204±0.021	1.588±0.011	4.7186±0.2395	0.424±0.003
8760414	0.931±0.013	1.078±0.005	10.0202±0.5205	1.048±0.003
8938364	0.997±0.01	1.354±0.004	9.2676±0.3949	0.565±0.001
9025370	1.049±0.017	1.026±0.007	3.8677±0.2507	1.366±0.005
9098294	1.01±0.015	1.157±0.006	7.0811±0.2328	0.919±0.003
9139151	1.149±0.02	1.147±0.008	2.0156±0.254	1.073±0.006
9139163	1.347±0.02	1.548±0.009	2.2022±0.1686	0.511±0.003
9206432	1.43±0.058	1.508±0.024	0.7326±0.476	0.587±0.015
9353712	1.468±0.051	2.16±0.031	2.5757±0.2254	0.205±0.003
9410862	0.974±0.022	1.155±0.01	7.8825±0.2781	0.891±0.006
9414417	1.372±0.031	1.908±0.017	2.8741±0.1875	0.278±0.002
9812850	1.398±0.045	1.829±0.025	2.7891±0.2661	0.322±0.005
9955598	0.922±0.015	0.893±0.005	7.7369±0.3687	1.821±0.003

Table A.3 continued				
9965715	1.202±0.03	1.325±0.014	3.103±0.3033	0.727±0.007
10068307	1.368±0.018	2.066±0.01	3.8228±0.1967	0.218±0.001
10079226	1.149±0.023	1.158±0.008	2.8091±0.5768	1.043±0.005
10162436	1.451±0.024	2.063±0.012	3.1595±0.2045	0.233±0.001
10454113	1.238±0.02	1.271±0.008	1.9138±0.3144	0.85±0.005
10516096	1.101±0.01	1.42±0.005	6.8501±0.2897	0.542±0.002
10644253	1.141±0.023	1.11±0.009	1.3638±0.2576	1.175±0.006
10730618	1.366±0.063	1.78±0.034	2.7972±0.3662	0.341±0.005
10963065	1.072±0.016	1.223±0.007	4.6663±0.2427	0.824±0.004
11081729	1.346±0.045	1.439±0.021	1.5996±0.4061	0.636±0.014
11253226	1.571±0.016	1.651±0.009	0.0245±0.0036	0.492±0.007
11772920	0.862±0.018	0.856±0.006	8.3261±0.4245	1.937±0.006
12009504	1.158±0.017	1.394±0.009	4.2119±0.1933	0.602±0.004
12069127	1.509±0.047	2.252±0.031	2.3201±0.2127	0.186±0.003
12069424	1.079±0.008	1.228±0.003	6.4287±0.2493	0.822±0.001
12069449	1.006±0.007	1.103±0.003	7.4936±0.2306	1.057±0.002
12258514	1.202±0.013	1.58±0.007	4.7476±0.1728	0.43±0.002
12317678	1.432±0.026	1.853±0.012	2.2358±0.1668	0.317±0.002

Table A.4: Derived mass, radius, age, and density for Grid A with L_*.

KIC	M_* ($M_\odot$)	R_* ($R_\odot$)	Age (Myr)	$\bar{\rho}$ (g cm^{-3})
1435467	1.393±0.034	1.724±0.017	2.6084±0.2074	0.383±0.003
2837475	1.47±0.033	1.648±0.016	1.3108±0.1391	0.463±0.005
3427720	1.099±0.014	1.111±0.006	2.2675±0.1664	1.13±0.005
3456181	1.465±0.041	2.136±0.023	2.4149±0.1769	0.212±0.002
3632418	1.366±0.017	1.907±0.009	3.6958±0.1769	0.277±0.001
3656476	1.056±0.009	1.307±0.004	8.3339±0.2756	0.667±0.001
3735871	1.13±0.021	1.106±0.008	1.4943±0.26	1.176±0.006
4914923	1.103±0.01	1.372±0.005	6.4449±0.2151	0.602±0.002
5184732	1.194±0.014	1.336±0.006	4.2632±0.1873	0.705±0.002
5773345	1.483±0.033	2.018±0.019	2.6317±0.1935	0.254±0.002
5950854	1.01±0.014	1.256±0.007	8.6589±0.2868	0.718±0.002

Table A.4 continued				
6106415	1.107±0.008	1.235±0.003	5.4301±0.2106	0.828±0.001
6116048	1.086±0.01	1.253±0.004	5.6696±0.2924	0.778±0.002
6225718	1.185±0.015	1.248±0.006	2.7182±0.1789	0.859±0.003
6508366	1.485±0.039	2.164±0.022	2.4274±0.1797	0.206±0.002
6603624	1.012±0.006	1.15±0.002	8.6803±0.1607	0.937±0.001
6679371	1.572±0.021	2.223±0.014	1.9633±0.0995	0.202±0.002
6933899	1.099±0.004	1.569±0.002	7.1136±0.1279	0.4±0.001
7103006	1.457±0.018	1.954±0.009	2.4392±0.1469	0.275±0.002
7106245	1.05±0.016	1.154±0.007	5.231±0.2577	0.962±0.005
7206837	1.347±0.034	1.577±0.017	2.5404±0.226	0.484±0.005
7296438	1.106±0.01	1.374±0.005	6.9235±0.2456	0.601±0.002
7510397	1.351±0.02	1.862±0.012	3.2739±0.1487	0.295±0.002
7680114	1.101±0.007	1.411±0.003	7.3052±0.2221	0.553±0.001
7771282	1.27±0.03	1.665±0.018	2.8348±0.2763	0.388±0.01
7871531	0.847±0.029	0.866±0.012	11.8338±0.9531	1.836±0.085
7940546	1.378±0.015	1.947±0.006	3.3106±0.1719	0.263±0.001
7970740	0.847±0.009	0.802±0.003	9.0826±0.346	2.31±0.002
8006161	1.024±0.01	0.942±0.003	3.969±0.2208	1.729±0.002
8150065	1.16±0.03	1.378±0.017	3.721±0.2957	0.625±0.01
8179536	1.186±0.032	1.326±0.015	2.641±0.2749	0.716±0.008
8228742	1.31±0.022	1.852±0.012	4.1509±0.2234	0.29±0.002
8379927	1.144±0.015	1.131±0.005	1.9346±0.2293	1.114±0.003
8394589	1.095±0.014	1.181±0.006	3.1829±0.2272	0.937±0.005
8424992	1.003±0.015	1.08±0.006	8.5392±0.3565	1.121±0.002
8694723	1.21±0.015	1.594±0.007	4.9415±0.2366	0.421±0.002
8760414	0.932±0.012	1.078±0.005	9.8943±0.423	1.048±0.003
8938364	1.0±0.006	1.356±0.003	9.0883±0.2576	0.565±0.001
9025370	1.05±0.015	1.027±0.006	3.849±0.2191	1.366±0.004
9098294	1.009±0.012	1.157±0.005	7.1377±0.2535	0.919±0.003
9139151	1.147±0.017	1.146±0.007	2.0036±0.1986	1.074±0.005
9139163	1.351±0.019	1.551±0.008	2.1901±0.1463	0.51±0.003
9206432	1.424±0.036	1.518±0.016	1.1144±0.1846	0.574±0.007

Table A.4 continued				
9353712	1.469±0.044	2.16±0.026	2.5652±0.1932	0.205±0.002
9410862	0.972±0.02	1.154±0.008	7.8715±0.2387	0.891±0.005
9414417	1.376±0.027	1.91±0.015	2.8508±0.1569	0.278±0.002
9812850	1.402±0.039	1.832±0.022	2.7873±0.2237	0.321±0.004
9955598	0.923±0.013	0.894±0.004	7.7197±0.3282	1.821±0.003
9965715	1.207±0.027	1.328±0.012	3.0768±0.2602	0.726±0.006
10068307	1.368±0.015	2.067±0.009	3.8455±0.1696	0.218±0.001
10079226	1.151±0.019	1.158±0.007	2.8449±0.4989	1.042±0.004
10162436	1.454±0.021	2.064±0.011	3.1379±0.1847	0.233±0.001
10454113	1.276±0.014	1.286±0.005	1.9259±0.2336	0.845±0.004
10516096	1.102±0.009	1.42±0.005	6.8448±0.2552	0.542±0.002
10644253	1.142±0.02	1.11±0.008	1.3514±0.2136	1.175±0.005
10730618	1.37±0.057	1.782±0.031	2.7612±0.3192	0.341±0.005
10963065	1.072±0.014	1.224±0.007	4.6785±0.2131	0.824±0.003
11081729	1.344±0.039	1.44±0.018	1.6536±0.3296	0.634±0.011
11253226	1.572±0.016	1.653±0.009	0.0251±0.0456	0.49±0.006
11772920	0.862±0.016	0.856±0.005	8.2798±0.3687	1.937±0.005
12009504	1.159±0.014	1.394±0.008	4.1911±0.1577	0.602±0.004
12069127	1.518±0.044	2.258±0.028	2.2708±0.1918	0.186±0.003
12069424	1.063±0.006	1.222±0.002	7.2195±0.2147	0.82±0.001
12069449	1.012±0.006	1.105±0.002	7.3491±0.2134	1.056±0.001
12258514	1.202±0.011	1.58±0.006	4.7491±0.1469	0.429±0.001
12317678	1.433±0.024	1.854±0.011	2.2341±0.1513	0.317±0.002

Table A.5: Defined mass, radius, age, and density for Grid B without L_*.

KIC	M_* ($M_\odot$)	R_* ($R_\odot$)	Age (Myr)	$\bar{\rho}$ (g cm^{-3})
1435467	1.348±0.035	1.704±0.018	2.6588±0.2441	0.384±0.004
2837475	1.368±0.038	1.602±0.019	1.5721±0.2227	0.468±0.007
3427720	1.099±0.013	1.117±0.005	2.5614±0.2228	1.11±0.002
3456181	1.385±0.053	2.095±0.032	2.7696±0.2768	0.212±0.003
3632418	1.384±0.014	1.914±0.007	3.0468±0.136	0.278±0.001
3656476	1.053±0.005	1.306±0.002	7.3496±0.1569	0.667±0.001
3735871	1.109±0.022	1.102±0.008	2.1339±0.3885	1.166±0.005
4914923	1.104±0.007	1.372±0.004	5.7874±0.1507	0.602±0.002
5184732	1.14±0.01	1.315±0.005	4.4097±0.1295	0.707±0.002
5773345	1.393±0.034	1.973±0.02	2.8666±0.2429	0.256±0.002
5950854	1.003±0.013	1.252±0.006	7.9061±0.3297	0.719±0.003
6106415	1.074±0.014	1.22±0.006	4.7977±0.2528	0.833±0.002
6116048	1.053±0.009	1.239±0.004	5.6875±0.1907	0.78±0.002
6225718	1.143±0.011	1.232±0.005	2.8817±0.1619	0.862±0.003
6508366	1.5±0.036	2.173±0.022	2.2195±0.1789	0.206±0.002
6603624	1.003±0.008	1.146±0.003	7.717±0.289	0.938±0.001
6679371	1.529±0.033	2.197±0.021	1.9317±0.1534	0.203±0.003
6933899	1.116±0.01	1.577±0.007	6.13±0.1631	0.401±0.002
7103006	1.404±0.015	1.93±0.008	2.4627±0.1337	0.275±0.002
7106245	0.963±0.017	1.146±0.027	6.1945±0.2642	0.903±0.058
7206837	1.299±0.035	1.556±0.018	2.6378±0.2703	0.485±0.006
7296438	1.107±0.008	1.373±0.004	5.8209±0.1868	0.602±0.002
7510397	1.314±0.023	1.847±0.013	3.5087±0.2162	0.294±0.002
7680114	1.103±0.006	1.409±0.003	6.0681±0.1252	0.555±0.001
7771282	1.247±0.043	1.631±0.025	3.5345±0.3697	0.405±0.007
7871531	0.836±0.026	0.862±0.017	9.2266±1.492	1.843±0.088
7940546	1.349±0.014	1.932±0.006	3.1548±0.1445	0.264±0.001
7970740	0.822±0.019	0.792±0.006	6.8253±2.0098	2.334±0.053
8006161	0.911±0.016	0.903±0.006	6.0764±0.3699	1.741±0.003
8150065	1.198±0.032	1.401±0.016	3.4535±0.383	0.614±0.007
8179536	1.193±0.031	1.332±0.015	2.6039±0.3053	0.71±0.009
8228742	1.262±0.022	1.821±0.013	3.8294±0.1936	0.295±0.002

Table A.5 continued				
8379927	1.121±0.017	1.124±0.006	2.1864±0.2445	1.113±0.003
8394589	1.053±0.016	1.167±0.008	3.9901±0.2705	0.933±0.007
8424992	0.921±0.014	1.045±0.006	9.0888±0.2611	1.136±0.005
8694723	1.161±0.015	1.572±0.008	5.2829±0.2462	0.421±0.002
8760414	0.891±0.011	1.062±0.005	12.7379±0.1884	1.048±0.003
8938364	0.987±0.01	1.351±0.005	9.012±0.3438	0.564±0.001
9025370	0.965±0.016	0.999±0.006	5.0228±0.3292	1.363±0.002
9098294	0.958±0.01	1.138±0.005	8.8995±0.3146	0.915±0.002
9139151	1.131±0.017	1.143±0.007	2.4618±0.2219	1.067±0.005
9139163	1.339±0.02	1.547±0.008	2.0205±0.1505	0.509±0.002
9206432	1.344±0.036	1.484±0.017	1.376±0.2339	0.579±0.009
9353712	1.425±0.048	2.136±0.029	2.6269±0.2432	0.206±0.003
9410862	0.999±0.015	1.168±0.007	6.8485±0.3961	0.884±0.004
9414417	1.329±0.03	1.887±0.017	3.0084±0.1953	0.279±0.002
9812850	1.318±0.036	1.788±0.02	2.9943±0.2482	0.325±0.004
9955598	0.878±0.014	0.877±0.005	6.4626±0.3208	1.833±0.004
9965715	1.162±0.025	1.309±0.012	3.3141±0.2737	0.729±0.008
10068307	1.329±0.017	2.045±0.009	3.7985±0.1719	0.219±0.001
10079226	1.119±0.021	1.145±0.008	2.2652±0.4724	1.049±0.005
10162436	1.379±0.025	2.023±0.014	3.2213±0.2059	0.235±0.001
10454113	1.164±0.016	1.236±0.007	1.8184±0.2627	0.867±0.006
10516096	1.095±0.008	1.415±0.004	5.9745±0.221	0.545±0.002
10644253	1.118±0.02	1.102±0.008	0.904±0.2697	1.177±0.006
10730618	1.369±0.058	1.786±0.032	2.6865±0.3668	0.339±0.005
10963065	1.095±0.013	1.232±0.006	3.9171±0.202	0.825±0.004
11081729	1.332±0.037	1.441±0.017	1.7331±0.3389	0.627±0.011
11253226	1.533±0.02	1.637±0.01	0.0218±0.004	0.492±0.006
11772920	0.778±0.013	0.828±0.005	13.5794±0.6213	1.933±0.002
12009504	1.22±0.021	1.427±0.01	3.641±0.2543	0.592±0.003
12069127	1.527±0.043	2.266±0.03	2.1306±0.1994	0.185±0.003
12069424	1.044±0.009	1.213±0.004	6.3344±0.2445	0.824±0.001
12069449	0.981±0.007	1.093±0.002	7.3911±0.3	1.059±0.001

Table A.5 continued				
12258514	1.196±0.013	1.579±0.007	4.7629±0.2024	0.428±0.002
12317678	1.413±0.023	1.845±0.01	2.1078±0.1479	0.317±0.002

Table A.6: Derived mass, radius, age, and density for Grid B with L_*.

KIC	M_* ($M_\odot$)	R_* ($R_\odot$)	Age (Myr)	$\bar{\rho}$ (g cm^{-3})
1435467	1.35±0.029	1.705±0.015	2.6468±0.2043	0.384±0.003
2837475	1.568±0.017	1.662±0.009	0.0216±0.0034	0.481±0.007
3427720	1.099±0.011	1.117±0.004	2.5441±0.2029	1.11±0.002
3456181	1.5±0.041	2.159±0.025	2.2158±0.1916	0.21±0.002
3632418	1.385±0.012	1.915±0.005	3.0545±0.119	0.278±0.001
3656476	1.053±0.004	1.305±0.002	7.3518±0.1211	0.667±0.001
3735871	1.108±0.018	1.102±0.007	2.113±0.3297	1.166±0.005
4914923	1.104±0.007	1.372±0.003	5.7977±0.1307	0.602±0.001
5184732	1.14±0.008	1.314±0.004	4.4086±0.1083	0.707±0.001
5773345	1.391±0.031	1.971±0.018	2.8888±0.2166	0.256±0.002
5950854	1.002±0.012	1.252±0.006	7.9346±0.3162	0.719±0.002
6106415	1.071±0.012	1.219±0.005	4.8594±0.224	0.833±0.002
6116048	1.052±0.007	1.239±0.003	5.7056±0.1697	0.78±0.002
6225718	1.143±0.009	1.232±0.004	2.8969±0.1377	0.861±0.003
6508366	1.502±0.031	2.175±0.019	2.2137±0.1496	0.205±0.002
6603624	1.004±0.008	1.147±0.003	7.7139±0.2501	0.938±0.001
6679371	1.535±0.03	2.202±0.018	1.9213±0.1381	0.202±0.002
6933899	1.109±0.007	1.575±0.004	6.0329±0.1259	0.399±0.001
7103006	1.404±0.015	1.93±0.008	2.4729±0.1208	0.275±0.002
7106245	1.043±0.016	1.151±0.008	5.1092±0.2403	0.962±0.005
7206837	1.306±0.03	1.56±0.015	2.5952±0.225	0.484±0.005
7296438	1.106±0.007	1.373±0.003	5.8416±0.1578	0.602±0.001
7510397	1.32±0.021	1.85±0.012	3.4511±0.1909	0.294±0.002
7680114	1.103±0.005	1.409±0.002	6.0896±0.1141	0.555±0.001
7771282	1.251±0.039	1.633±0.023	3.5085±0.3268	0.404±0.006
7871531	0.838±0.021	0.867±0.013	9.3207±1.2807	1.812±0.069
7940546	1.349±0.013	1.933±0.005	3.1693±0.134	0.263±0.001

Table A.6 continued				
7970740	0.825±0.019	0.791±0.007	6.9278±1.8306	2.346±0.073
8006161	0.911±0.014	0.903±0.005	6.0491±0.3072	1.742±0.003
8150065	1.2±0.029	1.402±0.014	3.4501±0.3052	0.613±0.007
8179536	1.194±0.028	1.333±0.014	2.5901±0.2508	0.71±0.008
8228742	1.262±0.019	1.821±0.011	3.8254±0.1635	0.294±0.002
8379927	1.123±0.013	1.124±0.005	2.1811±0.1997	1.113±0.003
8394589	1.054±0.015	1.167±0.007	3.9818±0.2312	0.933±0.007
8424992	0.922±0.012	1.045±0.005	9.0982±0.2444	1.136±0.004
8694723	1.162±0.013	1.572±0.007	5.3143±0.2115	0.421±0.002
8760414	0.866±0.01	1.051±0.004	12.2341±0.1565	1.051±0.001
8938364	0.993±0.007	1.357±0.003	9.9319±0.3105	0.56±0.001
9025370	0.964±0.016	0.999±0.006	5.0367±0.3042	1.363±0.002
9098294	1.004±0.009	1.158±0.004	7.7647±0.3056	0.91±0.001
9139151	1.129±0.015	1.142±0.006	2.4558±0.1891	1.068±0.004
9139163	1.345±0.015	1.55±0.006	1.9992±0.1193	0.509±0.002
9206432	1.345±0.033	1.486±0.015	1.3813±0.2	0.578±0.007
9353712	1.426±0.04	2.137±0.024	2.6117±0.1952	0.206±0.002
9410862	0.999±0.013	1.168±0.006	6.8603±0.3245	0.883±0.003
9414417	1.332±0.026	1.888±0.015	2.9898±0.1701	0.278±0.002
9812850	1.321±0.032	1.79±0.018	2.9899±0.217	0.325±0.003
9955598	0.879±0.013	0.877±0.005	6.4476±0.2749	1.832±0.004
9965715	1.164±0.022	1.31±0.011	3.2887±0.2346	0.729±0.007
10068307	1.332±0.013	2.048±0.007	3.7818±0.1432	0.219±0.001
10079226	1.121±0.018	1.146±0.006	2.2897±0.4255	1.049±0.005
10162436	1.387±0.021	2.028±0.011	3.1661±0.1766	0.234±0.001
10454113	1.215±0.014	1.261±0.006	1.985±0.2117	0.854±0.005
10516096	1.095±0.007	1.415±0.004	5.9821±0.2139	0.545±0.001
10644253	1.12±0.016	1.103±0.006	0.9125±0.2206	1.176±0.005
10730618	1.368±0.051	1.786±0.028	2.7002±0.3237	0.338±0.005
10963065	1.096±0.011	1.233±0.005	3.9123±0.1829	0.824±0.003
11081729	1.332±0.033	1.442±0.015	1.7429±0.2867	0.626±0.009
11253226	1.533±0.02	1.636±0.01	0.022±0.004	0.493±0.006

Table A.6 continued				
11772920	0.776±0.012	0.827±0.004	13.6081±0.5372	1.933±0.002
12009504	1.22±0.019	1.427±0.008	3.6516±0.2224	0.592±0.003
12069127	1.536±0.037	2.272±0.025	2.0913±0.1662	0.185±0.002
12069424	1.047±0.007	1.214±0.003	6.3103±0.1805	0.823±0.001
12069449	0.987±0.006	1.095±0.002	7.1478±0.2227	1.059±0.001
12258514	1.196±0.012	1.579±0.006	4.7547±0.1903	0.428±0.001
12317678	1.414±0.02	1.847±0.009	2.0988±0.1272	0.316±0.001

Table A.7: Results for the helium surface abundance obtained using the grids with L_* as a constraint.

	Y_s	
KIC	Grid A	Grid B
1435467	0.285±0.005	0.299±0.007
2837475	0.293±0.004	0.313±0.006
3427720	0.245±0.007	0.291±0.005
3456181	0.273±0.004	0.295±0.007
3632418	0.295±0.003	0.316±0.003
3656476	0.249±0.004	0.278±0.002
3735871	0.269±0.008	0.281±0.01
4914923	0.244±0.007	0.261±0.007
5184732	0.296±0.003	0.299±0.007
5773345	0.297±0.003	0.315±0.005
5950854	0.232±0.007	0.234±0.006
6106415	0.261±0.005	0.267±0.006
6116048	0.235±0.004	0.24±0.003
6225718	0.283±0.003	0.286±0.008
6508366	0.277±0.005	0.296±0.007
6603624	0.251±0.002	0.262±0.002
6679371	0.289±0.004	0.306±0.006
6933899	0.224±0.004	0.245±0.008
7103006	0.298±0.003	0.32±0.003
7106245	0.231±0.008	0.235±0.009
7206837	0.287±0.005	0.301±0.007

Table A.7 continued		
7296438	0.256±0.008	0.273±0.007
7510397	0.276±0.003	0.293±0.004
7680114	0.251±0.004	0.259±0.005
7771282	0.27±0.004	0.284±0.007
7871531	0.236±0.011	0.232±0.013
7940546	0.292±0.002	0.311±0.003
7970740	0.246±0.003	0.249±0.018
8006161	0.273±0.003	0.262±0.006
8150065	0.262±0.02	0.289±0.011
8179536	0.269±0.007	0.284±0.007
8228742	0.282±0.003	0.28±0.004
8379927	0.281±0.005	0.286±0.007
8394589	0.225±0.008	0.222±0.011
8424992	0.252±0.007	0.226±0.006
8694723	0.279±0.002	0.291±0.006
8760414	0.222±0.004	0.215±0.004
8938364	0.22±0.003	0.252±0.003
9025370	0.252±0.005	0.282±0.004
9098294	0.231±0.005	0.264±0.005
9139151	0.27±0.008	0.274±0.011
9139163	0.297±0.003	0.321±0.003
9206432	0.292±0.006	0.298±0.008
9353712	0.275±0.005	0.284±0.007
9410862	0.221±0.009	0.233±0.007
9414417	0.272±0.003	0.281±0.004
9812850	0.284±0.005	0.287±0.007
9955598	0.268±0.005	0.252±0.005
9965715	0.27±0.004	0.272±0.012
10068307	0.282±0.003	0.292±0.003
10079226	0.29±0.007	0.293±0.011
10162436	0.291±0.003	0.3±0.004
10454113	0.292±0.004	0.297±0.006

Table A.7 continued		
10516096	0.243±0.007	0.245±0.006
10644253	0.273±0.007	0.29±0.009
10730618	0.276±0.006	0.298±0.009
10963065	0.23±0.008	0.235±0.008
11081729	0.284±0.006	0.307±0.009
11253226	0.293±0.003	0.31±0.005
11772920	0.238±0.005	0.232±0.004
12009504	0.268±0.007	0.289±0.004
12069127	0.277±0.004	0.299±0.008
12069424	0.254±0.003	0.259±0.003
12069449	0.248±0.003	0.25±0.002
12258514	0.275±0.002	0.297±0.004
12317678	0.288±0.003	0.306±0.004

Literature Data

Table A.8: Summary of codes, physical inputs, and optimization methods applied by each pipeline. For more details see [26].

	AIMS	ASTFIT	BASTA	C2kSMO	GOE	V&A	YMCM
Models	MESA	ASTEC	GARSTEC	Cesam2k	MESA	MESA	YREC
Frequencies	InversionKit	ADIPLS	ADIPLS	LOSC	ADIPLS	ADIPLS	AB94
Solar mixture	GN93	GN93	GN98	GN93	GN98	GN98	GN98
Opacities	OPAL96+JF05	OPAL96+JF05	OPAL96+JF05	OPAL96+JF05	OPAL96	OP05+JF05	OPAL96
EOS	OPAL05	OPAL05	OPAL05	OPAL05	OPAL05	OPAL05	OPAL05
Nuclear Reactions	NACRE	NACRE	NACRE	NACRE	NACRE	NACRE	Solar fusion
Atmosphere	Eddington gray	Eddington gray	Eddington gray	Eddington gray	Eddington gray	Eddington gray	Eddington gray
Diffusion	No	MP93,$\leq 1.1M_\odot$	T94,$\leq 1.2M_\odot$	MP93	T94	T94,,$\leq 1.35M_\odot$	No
Overshoot	Yes	No	Yes	Yes	Yes	Yes	Yes
Convection	CG68	MLT58	MLT12	CGM96	CG68	MLT58	MLT58
$\alpha_{\rm MLT}$	1.8	1.5,1.8,2.1	1.791	Variable	Variable	Variable	Variable
$\Delta Y/\Delta Z$	2.0	1.0-2.0	1.4	Variable	Variable	Variable	Variable
Fitted Data	$\nu_i(n)$	$\nu_i(n)$	$r_{010}, r_{02}(n)$	$r_{010}, r_{02}(n), \nu_0(n_{\rm min})$	$\nu_i(n)$	$\langle\Delta\nu\rangle, \langle r_{02}\rangle, r_{01}(n), r_{10}(n+3)$	$\nu_i(n)$,$r_{010}, r_{02}(n)$
Surface correction	BG14	SC	None	TS15	BG14	HK08	BG14
Optimization	MCMC	χ^2 minimization	Bayesian	Levenberg-Marquardt	Downhill simplex	χ^2 minimization	Monte Carlo

ASTFIT Results

Table A.9: Results from ASTFIT.

KIC	M_* ($M_\odot$)	$R_*(R_\odot)$	age(Myr)	$\bar{\rho}$ (g cm^{-3})
1435467	1.3417±0.0479	1.7029±0.0232	2.6679±0.3173	0.3825±0.0035
2837475	1.3879±0.0485	1.6201±0.0221	1.6573±0.2363	0.4596±0.0056
3427720	1.099±0.0273	1.1145±0.0104	2.3521±0.4197	1.1178±0.0055
3456181	1.5569±0.034	2.1784±0.0225	1.8812±0.0953	0.2121±0.0025
3632418	1.4772±0.0306	1.9481±0.0162	2.4261±0.1315	0.2814±0.0013
3656476	1.0659±0.0183	1.3114±0.0077	8.1431±0.4817	0.6656±0.0009
3735871	1.1112±0.031	1.1014±0.0109	1.8414±0.7313	1.1711±0.0073
4914923	1.0513±0.0179	1.3481±0.0078	7.2282±0.4713	0.6043±0.0018
5184732	1.1619±0.0372	1.3234±0.0156	4.4499±0.3691	0.7059±0.0032
5773345	1.5098±0.0447	2.0364±0.0238	2.2791±0.1906	0.2517±0.0017
5950854	0.9739±0.0298	1.2397±0.0134	8.4574±0.863	0.7198±0.0038
6106415	1.0942±0.0206	1.227±0.0082	4.5596±0.3728	0.8341±0.0028
6116048	1.046±0.022	1.2357±0.0094	5.7476±0.4351	0.7806±0.003
6225718	1.1518±0.0286	1.2345±0.0116	2.9607±0.3214	0.8622±0.0048
6508366	1.5797±0.0295	2.2099±0.0179	1.8511±0.0823	0.2061±0.0016
6603624	1.0291±0.012	1.157±0.0046	8.1671±0.3124	0.9357±0.0007
6679371	1.5945±0.0334	2.2381±0.0201	1.6441±0.0892	0.2003±0.0021

Table A.9 continued				
6933899	1.1419±0.0067	1.5908±0.0039	6.2236±0.1193	0.3995±0.0008
7103006	1.45±0.0428	1.9538±0.0228	2.2238±0.1986	0.2738±0.0025
7106245	0.9179±0.0265	1.094±0.011	6.1905±0.9278	0.9873±0.0104
7206837	1.3256±0.0447	1.5719±0.0205	2.5051±0.3131	0.4806±0.0054
7296438	1.0805±0.0232	1.3619±0.0108	6.7058±0.5263	0.6024±0.003
7510397	1.4549±0.0267	1.9071±0.0139	2.5522±0.1291	0.2954±0.0012
7680114	1.0382±0.0224	1.3792±0.0103	7.8152±0.5586	0.5572±0.0019
7771282	1.2534±0.0613	1.6343±0.0289	3.5042±0.6309	0.4041±0.0044
7871531	0.8346±0.0233	0.8711±0.0087	9.2363±0.9607	1.778±0.0048
7940546	1.4798±0.0256	1.9901±0.0143	2.3247±0.1036	0.2644±0.0014
7970740	0.7512±0.0166	0.7684±0.0062	10.3904±0.8317	2.3313±0.0058
8006161	0.974±0.0288	0.9254±0.0096	4.6878±0.4345	1.7303±0.0029
8150065	1.16±0.0495	1.3837±0.0223	3.7998±0.6202	0.6164±0.0068
8179536	1.1977±0.0428	1.3396±0.0179	2.7851±0.5526	0.7015±0.0084
8228742	1.4762±0.0296	1.9196±0.0151	2.5344±0.1356	0.2939±0.0012
8379927	1.121±0.0294	1.1215±0.0111	1.7407±0.4314	1.1192±0.0059
8394589	1.0553±0.0293	1.1706±0.0114	4.0583±0.696	0.9264±0.007
8424992	0.9269±0.0247	1.0502±0.0098	9.4365±0.8835	1.1267±0.0028
8694723	1.1086±0.0204	1.535±0.0105	5.2685±0.2669	0.4317±0.0019
8760414	0.7849±0.0099	1.0116±0.0044	12.6078±0.5978	1.0677±0.0027
8938364	0.979±0.0251	1.349±0.0127	10.1796±0.657	0.5616±0.002
9025370	0.9718±0.0234	1.0014±0.0084	5.0899±0.6904	1.3626±0.0031
9098294	0.9831±0.0217	1.1482±0.0088	7.7103±0.6476	0.9145±0.0025
9139151	1.1483±0.03	1.1499±0.0108	2.4324±0.5033	1.0634±0.0054
9139163	1.3785±0.0388	1.5647±0.0164	1.9361±0.1994	0.5067±0.0038
9206432	1.3761±0.0482	1.5054±0.02	1.3569±0.2668	0.568±0.0061
9353712	1.5619±0.0413	2.1949±0.0286	1.9241±0.1048	0.2081±0.0032
9410862	0.9882±0.0294	1.161±0.0117	6.3299±0.9744	0.8892±0.0064
9414417	1.4475±0.0282	1.9454±0.0161	2.3843±0.1219	0.2769±0.0018
9812850	1.3717±0.0385	1.8143±0.021	2.5871±0.2119	0.3234±0.003
9955598	0.9015±0.0215	0.8867±0.0074	6.5781±0.6292	1.8213±0.0031
9965715	1.0819±0.0448	1.2789±0.019	4.422±0.8554	0.7281±0.008

Table A.9 continued				
10068307	1.6081±0.0263	2.1646±0.0139	2.0082±0.0944	0.2233±0.0007
10079226	1.1148±0.0378	1.1454±0.0124	2.8675±1.2712	1.0445±0.0077
10162436	1.5439±0.0235	2.0903±0.0128	2.2119±0.0948	0.2381±0.001
10454113	1.154±0.0316	1.2368±0.0124	2.3221±0.4769	0.859±0.0062
10516096	1.0876±0.0232	1.411±0.0112	6.1399±0.4115	0.5452±0.0027
10644253	1.1371±0.0284	1.11±0.0105	1.1767±0.5202	1.1708±0.0068
10730618	1.3626±0.0532	1.7851±0.0273	2.7193±0.3544	0.3372±0.0039
10963065	1.0847±0.023	1.2312±0.0094	4.4385±0.4224	0.8184±0.004
11081729	1.3153±0.0453	1.4359±0.0173	1.9282±0.3996	0.6256±0.0074
11253226	1.3655±0.0469	1.5939±0.0208	1.7264±0.2365	0.4748±0.0044
11772920	0.8349±0.0294	0.8479±0.0106	9.7211±1.1725	1.928±0.0051
12009504	1.1696±0.0456	1.4026±0.0209	4.1196±0.489	0.5967±0.0043
12069127	1.6259±0.0378	2.3193±0.0249	1.7588±0.0917	0.1835±0.002
12069424	1.0593±0.0158	1.2202±0.0061	6.665±0.3907	0.8212±0.0009
12069449	1.0036±0.014	1.1025±0.0052	7.0154±0.3414	1.0548±0.0008
12258514	1.1355±0.0147	1.5491±0.0073	5.7927±0.2244	0.4302±0.0014
12317678	1.3724±0.0302	1.824±0.0154	2.2006±0.1412	0.3185±0.0023

BASTA Results

Table A.10: Results from BASTA.

KIC	M_* ($M_\odot$)	R_*($R_\odot$)	age(Myr)	$\bar{\rho}$ (g cm^{-3})
1435467	1.3189±0.0304	1.6925±0.018	3.0164±0.4951	0.383008±0.007553
2837475	1.4291±0.019	1.6385±0.015	1.627±0.1118	0.457674±0.010627
3427720	1.108±0.0209	1.1167±0.009	2.2339±0.2396	1.121488±0.016747
3456181	1.4975±0.0304	2.1483±0.027	2.0901±0.1278	0.212757±0.007395
3632418	1.4082±0.0209	1.9114±0.021	2.6331±0.1757	0.284476±0.009267
3656476	1.0377±0.0513	1.2996±0.021	8.3663±1.7248	0.666377±0.011998
3735871	1.089±0.0399	1.0957±0.012	2.3457±1.038	1.169009±0.017081
4914923	1.0586±0.0589	1.3566±0.024	7.5678±1.6609	0.597164±0.009075
5184732	1.1479±0.0399	1.3206±0.015	4.8529±1.5651	0.701122±0.012144
5773345	1.469±0.0285	2.0194±0.021	2.5533±0.2555	0.251367±0.004916
5950854	0.9693±0.0285	1.2366±0.018	8.9253±1.1179	0.7205±0.010088
6106415	1.0681±0.0513	1.2186±0.018	5.0286±1.2776	0.834782±0.014998
6116048	0.9389±0.0494	1.1916±0.021	9.5801±2.1559	0.775234±0.015251
6225718	1.1593±0.0304	1.2336±0.012	2.4095±0.527	0.870687±0.016615
6508366	1.5279±0.0304	2.1873±0.018	2.0582±0.1278	0.206586±0.004105
6603624	1.0092±0.0285	1.1497±0.012	7.8234±0.9422	0.934006±0.013962
6679371	1.5279±0.0399	2.2143±0.024	1.9464±0.1757	0.199743±0.004645
6933899	1.1289±0.0285	1.5875±0.018	6.3381±0.7187	0.394328±0.008906
7103006	1.4177±0.0399	1.9444±0.018	2.4734±0.2236	0.274412±0.005522
7106245	0.9214±0.0216	1.0959±0.012	6.2732±1.0591	0.991209±0.014118
7206837	1.298±0.0304	1.5635±0.015	2.9046±0.4152	0.478844±0.010174
7296438	1.0776±0.0608	1.3626±0.024	7.2325±1.4852	0.599478±0.01028
7510397	1.3683±0.0209	1.8574±0.018	2.8247±0.1437	0.30048±0.006225
7680114	1.0586±0.0399	1.3926±0.021	7.6796±1.4533	0.550386±0.008355
7771282	1.2885±0.0304	1.6535±0.015	3.24±0.3513	0.402616±0.007534
7871531	0.8287±0.0304	0.8707±0.009	9.9633±1.9324	1.776123±0.031393
7940546	1.3987±0.0304	1.9414±0.027	2.3297±0.0798	0.269754±0.001207
7970740	0.728±0.0304	0.7628±0.006	12.9817±1.3575	2.334073±0.031426
8006161	0.9788±0.0304	0.9247±0.012	3.5913±1.5331	1.732853±0.029523
8150065	1.1878±0.0399	1.3986±0.018	3.8309±0.9901	0.610025±0.009183

Table A.10 continued				
8179536	1.1593±0.0494	1.3266±0.021	3.5434±1.038	0.697301±0.01331
8228742	1.3778±0.0209	1.8694±0.021	2.8886±0.1597	0.298167±0.007155
8379927	1.1194±0.0399	1.1197±0.015	1.9943±0.8464	1.12156±0.018619
8394589	1.0377±0.0418	1.1646±0.015	4.4537±0.9422	0.927167±0.018554
8424992	0.918±0.0399	1.0477±0.012	9.612±1.9164	1.125086±0.009336
8694723	1.1384±0.0209	1.5485±0.015	4.6932±0.4791	0.431524±0.00897
8760414	0.8115±0.031	1.0196±0.0097	11.6642±1.2847	1.075134±0.018828
8938364	0.9883±0.0095	1.3446±0.018	10.2508±0.559	0.570916±0.004695
9025370	0.9693±0.0304	1.0027±0.009	6.5458±1.2616	1.359891±0.017476
9098294	0.9693±0.019	1.1377±0.015	8.0789±0.9901	0.917731±0.014364
9139151	1.1783±0.0399	1.1526±0.015	1.3236±0.9422	1.075444±0.019344
9139163	1.3987±0.0304	1.5575±0.012	1.5951±0.2236	0.52313±0.013528
9206432	1.3778±0.0418	1.5095±0.015	1.5312±0.2076	0.56535±0.009272
9353712	1.5089±0.0285	2.1723±0.024	2.154±0.1118	0.208002±0.004484
9410862	0.9693±0.0494	1.1557±0.018	6.929±1.4852	0.887121±0.016617
9414417	1.3987±0.019	1.9174±0.021	2.6491±0.1597	0.278549±0.005177
9812850	1.3683±0.0399	1.8214±0.015	2.713±0.4631	0.319898±0.0077
9955598	0.899±0.0399	0.8857±0.012	6.2902±1.9483	1.820967±0.026211
9965715	1.2087±0.0399	1.3266±0.015	2.9206±0.8624	0.72626±0.01341
10068307	1.469±0.0095	2.0823±0.018	2.3616±0.0798	0.229193±0.004039
10079226	1.1194±0.019	1.1466±0.009	3.0643±0.7027	1.043018±0.015266
10162436	1.4481±0.0209	2.0373±0.021	2.4574±0.0958	0.241839±0.004865
10454113	1.1688±0.0209	1.2456±0.009	2.8886±0.559	0.851006±0.011611
10516096	1.0586±0.0494	1.3986±0.024	7.0089±1.3255	0.542953±0.009949
10644253	1.0985±0.0399	1.0987±0.015	2.3936±1.1179	1.164403±0.018921
10730618	1.3379±0.0399	1.7794±0.024	3.0483±0.4631	0.333973±0.007171
10963065	0.9883±0.0608	1.1946±0.021	7.1526±1.9164	0.815059±0.016289
11081729	1.298±0.0399	1.4226±0.015	1.8825±0.5909	0.63592±0.012491
11253226	1.4082±0.0209	1.6145±0.012	1.5951±0.0639	0.475516±0.008206
11772920	0.8287±0.0399	0.8438±0.015	10.666±2.7309	1.926522±0.027736
12009504	1.1688±0.019	1.4016±0.012	3.9746±0.5749	0.597379±0.009307
12069127	1.5678±0.0304	2.2983±0.021	2.0103±0.1118	0.182628±0.00344

Table A.10 continued				
12069424	1.0491±0.019	1.2156±0.012	6.6735±0.8145	0.819863±0.015658
12069449	0.9883±0.0209	1.0957±0.009	7.3922±0.8943	1.056983±0.018548
12258514	1.2581±0.0095	1.6055±0.012	4.0544±0.1757	0.428158±0.006404
12317678	1.3379±0.0399	1.8154±0.018	2.4574±0.2236	0.316265±0.009458

YMCM Results

Table A.11: Results from YMCM.

KIC	M_* ($M_\odot$)	R_*($R_\odot$)	age(Myr)	$\bar{\rho}$ (g cm^{-3})
1435467	1.3821±0.046	1.7181±0.0215	2.5562±0.1864	0.38371±0.003668
2837475	1.4363±0.0656	1.6529±0.0259	1.6669±0.1948	0.44763±0.003775
3427720	1.1266±0.0367	1.1232±0.0133	2.4526±0.2028	1.1194±0.004005
3456181	1.4881±0.0409	2.1468±0.0238	2.0014±0.1082	0.21181±0.001949
3632418	1.398±0.0312	1.9053±0.0163	2.7441±0.1529	0.28464±0.001568
3656476	1.0833±0.0298	1.3183±0.0128	9.2398±0.5953	0.66581±0.0016
3735871	1.1316±0.0464	1.1084±0.0159	1.9465±0.5669	1.1699±0.004565
4914923	1.1603±0.0297	1.3983±0.0122	6.8714±0.5104	0.59757±0.000731
5184732	1.2433±0.0418	1.3543±0.0159	4.1592±0.2865	0.70475±0.002275
5773345	1.5794±0.0513	2.0634±0.0255	2.0687±0.1317	0.25312±0.002307
5950854	0.9798±0.0317	1.2412±0.0147	9.0398±0.6805	0.72148±0.003586
6106415	1.1215±0.0283	1.236±0.011	4.9619±0.3598	0.83637±0.0028
6116048	1.0622±0.0288	1.24±0.0123	6.3683±0.3909	0.78451±0.003491
6225718	1.2133±0.035	1.2543±0.0133	2.5607±0.2785	0.86566±0.004773
6508366	1.535±0.0492	2.1891±0.0273	1.9013±0.1113	0.20602±0.002043
6603624	1.0606±0.0246	1.1693±0.0033	9.5634±0.3177	0.93423±0.000636
6679371	1.5369±0.0471	2.2057±0.027	1.5857±0.1009	0.20167±0.002615
6933899	1.1437±0.0324	1.5884±0.0153	7.1969±0.6931	0.40184±0.001072
7103006	1.4599±0.0599	1.9515±0.0292	2.046±0.1605	0.27651±0.002659
7106245	1.0146±0.0163	1.1375±0.0002	7.7287±0.0782	0.97091±0.001121
7206837	1.341±0.0616	1.5739±0.0251	2.4476±0.2566	0.48412±0.004369
7296438	1.1392±0.0415	1.3868±0.0177	6.7815±0.5429	0.60135±0.002238
7510397	1.3598±0.0214	1.8574±0.0106	3.0989±0.1446	0.29886±0.001254
7680114	1.0838±0.0371	1.3993±0.0173	7.5561±0.4765	0.55691±0.002602
7771282	1.2701±0.0599	1.6417±0.0274	3.1491±0.3903	0.404±0.003965
7871531	0.856±0.0333	0.879±0.0119	9.8371±0.8373	1.7744±0.003776
7940546	1.42±0.0251	1.9559±0.0128	2.5489±0.1138	0.26729±0.001609
7970740	0.7487±0.0223	0.7671±0.0081	10.963±0.8071	2.3357±0.005067
8006161	0.9861±0.0253	0.9293±0.0083	5.1012±0.3253	1.7305±0.002257
8150065	1.1985±0.0498	1.4009±0.0208	3.6902±0.3505	0.61367±0.00386

Table A.11 continued				
8179536	1.2346±0.0514	1.3542±0.0195	2.6906±0.3851	0.69983±0.005041
8228742	1.3807±0.0205	1.8723±0.0105	3.0605±0.1288	0.29626±0.0009
8379927	1.1805±0.0226	1.142±0.0078	1.6471±0.2857	1.1163±0.003086
8394589	1.0538±0.0289	1.1685±0.0113	4.5981±0.4435	0.92992±0.004344
8424992	0.9575±0.0259	1.0625±0.0098	10.176±0.775	1.1239±0.002054
8694723	1.1927±0.0343	1.5666±0.0171	4.3766±0.7	0.43682±0.002077
8760414	0.8605±0.024	1.0436±0.0042	12.521±0.4846	1.0661±0.001818
8938364	1.0089±0.0158	1.3643±0.0004	12.613±0.0596	0.55959±0.000172
9025370	0.9894±0.0363	1.0078±0.0129	5.4655±0.6117	1.3607±0.002986
9098294	1.0091±0.0203	1.1583±0.0081	8.4705±0.4835	0.91437±0.001999
9139151	1.1926±0.0452	1.165±0.0153	2.3401±0.4301	1.0618±0.003831
9139163	1.4237±0.0629	1.5774±0.0245	1.8151±0.2262	0.51056±0.003188
9206432	1.461±0.0789	1.5445±0.0281	1.205±0.287	0.55793±0.002796
9353712	1.5172±0.041	2.1806±0.0243	2.0329±0.1063	0.20607±0.001978
9410862	0.987±0.0272	1.1607±0.0107	6.9462±0.7216	0.88875±0.004146
9414417	1.3991±0.0352	1.9167±0.0173	2.5485±0.1383	0.27979±0.0021
9812850	1.39±0.0567	1.8204±0.0267	2.4758±0.1998	0.32439±0.003406
9955598	0.9375±0.0371	0.8989±0.0124	6.7977±0.5174	1.8168±0.003471
9965715	1.0958±0.0344	1.2802±0.0155	4.1458±0.4869	0.73538±0.004999
10068307	1.5064±0.0291	2.1162±0.0023	2.2856±0.0805	0.22386±0.000297
10079226	1.111±0.0534	1.1432±0.0194	2.9687±0.6017	1.0464±0.00482
10162436	1.4625±0.0225	2.0478±0.0132	2.5142±0.1003	0.23983±0.001209
10454113	1.1875±0.0429	1.2487±0.0159	2.3089±0.4066	0.85864±0.004697
10516096	1.0794±0.0314	1.4037±0.0151	6.8903±0.4294	0.54956±0.003018
10644253	1.1748±0.0385	1.1221±0.0133	1.0644±0.2375	1.1706±0.004292
10730618	1.3679±0.0709	1.7808±0.0342	2.5835±0.323	0.34091±0.003231
10963065	1.0672±0.032	1.2215±0.0129	5.0879±0.4348	0.82447±0.003684
11081729	1.3383±0.0597	1.4428±0.022	1.8389±0.2955	0.62719±0.00487
11253226	1.3995±0.0543	1.6175±0.0224	1.788±0.1918	0.46558±0.003483
11772920	0.8506±0.0338	0.8537±0.0119	10.805±1.1878	1.9248±0.00396
12009504	1.1986±0.0452	1.412±0.0193	3.9903±0.315	0.5994±0.004126
12069127	1.5894±0.0509	2.3051±0.0275	1.7595±0.1018	0.18272±0.001633

Table A.11 continued				
12069424	1.076±0.0344	1.2253±0.0072	7.5242±0.3771	0.82366±0.001579
12069449	1.0298±0.0277	1.1115±0.0105	7.2215±0.5679	1.056±0.002063
12258514	1.2704±0.0278	1.6085±0.0136	4.2362±0.1901	0.4299±0.001906
12317678	1.3408±0.0444	1.8089±0.0208	2.2406±0.1525	0.31893±0.002288

Helium Glitches Data

Table A.12: Helium values obtained by calibration of the stellar glitches [14].

KIC	Y_s from MESA	Y_s from GARSTEC
3427720	$0.205^{+0.015}_{-0.014}$	$0.193^{+0.016}_{-0.015}$
3632418	$0.304^{+0.016}_{-0.018}$	$0.248^{+0.009}_{-0.01}$
3656476	$0.271^{+0.024}_{-0.018}$	$0.267^{+0.029}_{-0.022}$
3735871	$0.217^{+0.016}_{-0.014}$	$0.206^{+0.019}_{-0.016}$
4914923	$0.242^{+0.012}_{-0.013}$	$0.222^{+0.008}_{-0.009}$
5184732	$0.291^{+0.028}_{-0.026}$	$0.313^{+0.033}_{-0.031}$
6106415	$0.222^{+0.014}_{-0.012}$	$0.203^{+0.011}_{-0.009}$
6116048	$0.227^{+0.011}_{-0.011}$	$0.206^{+0.008}_{-0.008}$
6225718	$0.235^{+0.009}_{-0.009}$	$0.227^{+0.009}_{-0.009}$
6603624	$0.241^{+0.018}_{-0.017}$	$0.221^{+0.008}_{-0.007}$
6933899	$0.223^{+0.009}_{-0.01}$	$0.194^{+0.008}_{-0.008}$
7296438	$0.247^{+0.025}_{-0.023}$	$0.233^{+0.019}_{-0.018}$
7510397	$0.261^{+0.018}_{-0.016}$	$0.209^{+0.008}_{-0.007}$
7680114	$0.198^{+0.018}_{-0.011}$	$0.186^{+0.018}_{-0.011}$
7940546	$0.331^{+0.025}_{-0.028}$	$0.222^{+0.012}_{-0.013}$
8006161	$0.246^{+0.025}_{-0.02}$	$0.258^{+0.029}_{-0.023}$
8179536	$0.27^{+0.038}_{-0.033}$	$0.28^{+0.04}_{-0.035}$
8228742	$0.23^{+0.02}_{-0.019}$	$0.207^{+0.011}_{-0.01}$
8379927	$0.25^{+0.008}_{-0.008}$	$0.237^{+0.008}_{-0.008}$
8394589	$0.253^{+0.025}_{-0.022}$	$0.215^{+0.018}_{-0.016}$
8694723	$0.251^{+0.016}_{-0.017}$	$0.194^{+0.014}_{-0.015}$
8760414	$0.203^{+0.022}_{-0.019}$	$0.178^{+0.011}_{-0.009}$
8938364	$0.234^{+0.01}_{-0.01}$	$0.22^{+0.01}_{-0.009}$
9098294	$0.256^{+0.015}_{-0.016}$	$0.247^{+0.016}_{-0.016}$
9139151	$0.233^{+0.014}_{-0.014}$	$0.216^{+0.015}_{-0.015}$
9410862	$0.221^{+0.021}_{-0.021}$	$0.206^{+0.018}_{-0.018}$
9965715	$0.312^{+0.061}_{-0.053}$	$0.253^{+0.032}_{-0.027}$
10068307	$0.257^{+0.013}_{-0.015}$	$0.251^{+0.01}_{-0.011}$
10079226	$0.257^{+0.032}_{-0.031}$	$0.244^{+0.032}_{-0.03}$
10162436	$0.324^{+0.021}_{-0.022}$	$0.273^{+0.015}_{-0.016}$

Table A.12 continued		
10454113	$0.279^{+0.017}_{-0.015}$	$0.276^{+0.018}_{-0.016}$
10516096	$0.212^{+0.012}_{-0.012}$	$0.204^{+0.011}_{-0.011}$
10644253	$0.27^{+0.026}_{-0.02}$	$0.256^{+0.026}_{-0.02}$
10963065	$0.233^{+0.022}_{-0.02}$	$0.21^{+0.019}_{-0.016}$
12009504	$0.256^{+0.029}_{-0.029}$	$0.227^{+0.019}_{-0.018}$
12069424	$0.246^{+0.017}_{-0.014}$	$0.228^{+0.017}_{-0.014}$
12069449	$0.255^{+0.01}_{-0.01}$	$0.225^{+0.008}_{-0.008}$
12258514	$0.25^{+0.007}_{-0.008}$	$0.215^{+0.007}_{-0.008}$

Mean Molecular Weight

Neutral gas:

$$\mu = \frac{4}{4X + Y} \text{ or } \mu = \frac{4}{3X - Z + 1}. \tag{A.1}$$

Total ionized gas:

$$\mu = \frac{4}{6X + Y + 2} \text{ or } \mu = \frac{4}{5X - Z + 3}. \tag{A.2}$$

Luminosity-mass relation

Stars with a radiative interior, a convective exterior, and p-p chain,

$$L_* \propto \mu^{101/13} M_*^{71/13}, \tag{A.3}$$

or CNO cycle instead,

$$L_* \propto \mu^{269/37} M_*^{191/37}. \tag{A.4}$$